Publ. Astron. Soc. Japan (2014) 00(0), 1–34
doi: 10.1093/pasj/xxx000

The dominant origin of diffuse Lyα halos around LAEs explored by SED fitting and clustering analysis

Haruka KUSAKABE[1], Kazuhiro SHIMASAKU[1,2], Rieko MOMOSE[1,3], Masami OUCHI[4,5], Kimihiko NAKAJIMA[6], Takuya HASHIMOTO [7, 8], Yuichi HARIKANE[5,9], John D. SILVERMAN[4] and Peter L. CAPAK[10, 11]

[1]Department of Astronomy, Graduate School of Science, The University of Tokyo, 7-3-1 Hongo, Bunkyo-ku, Tokyo 113-0033, Japan
[2]Research Center for the Early Universe, The University of Tokyo, 7-3-1 Hongo, Bunkyo-ku, Tokyo 113-0033, Japan
[3]Department of Physics, National Tsing Hua University, 101 Section 2 Kuang Fu Road, Hsinchu 30013, Taiwan
[4]Institute for Cosmic Ray Research, The University of Tokyo, 5-1-5 Kashiwanoha, Kashiwa, Chiba 277-8582, Japan
[5]Kavli Institute for the Physics and Mathematics of the Universe (Kavli IPMU, WPI), The University of Tokyo, 5-1-5 Kashiwanoha, Kashiwa, Chiba 277-8583, Japan
[6]European Southern Observatory, Karl-Schwarzschild-Strasse 2, D-85748 Garching, b. München, Germany
[7]College of General Education, Osaka Sangyo University, 3-1-1 Nakagaito, Daito, Osaka 574-8530, Japan
[8]National Astronomical Observatory of Japan, 2-21-1 Osawa, Mitaka, Tokyo 181-8588, Japan
[9]Department of Physics, Graduate School of Science, The University of Tokyo, 7-3-1 Hongo, Bunkyo, Tokyo 113-0033, Japan
[10]California Institute of Technology, MC 105-24, 1200 East California Blvd., Pasadena, CA 91125, USA
[11]Infrared Processing and Analysis Center, California Institute of Technology, MC 100-22, 770 South Wilson Ave., Pasadena, CA 91125, USA

*E-mail: kusakabe@astron.s.u-tokyo.ac.jp

Received ⟨reception date⟩; Accepted ⟨acception date⟩

Abstract

The physical origin of diffuse Lyα halos (LAHs) around star-forming galaxies is still a matter of debate. We present the dependence of LAH luminosity ($L(\mathrm{Ly}\alpha)_H$) on the stellar mass ($M_\star$), SFR, color excess ($E(B-V)_\star$), and dark matter halo mass (M_h) of the parent galaxy for ~ 900 Lyα emitters (LAEs) at $z \sim 2$ divided into ten subsamples. We calculate $L(\mathrm{Ly}\alpha)_H$ using the stacked observational relation between $L(\mathrm{Ly}\alpha)_H$ and central Lyα luminosity by Momose et al. (2016), which we find agree with the average trend of VLT/MUSE-detected individual LAEs. We find that our LAEs have relatively high $L(\mathrm{Ly}\alpha)_H$ despite low $M_\star$ and M_h, and that $L(\mathrm{Ly}\alpha)_H$ remains almost unchanged with $M_\star$ and perhaps with M_h. These results are incompatible with the cold streams (cooling radiation) scenario and the satellite-galaxy star-formation scenario, because the former predicts fainter $L(\mathrm{Ly}\alpha)_H$ and both predict steeper $L(\mathrm{Ly}\alpha)_H$ vs. $M_\star$ slopes. We argue that LAHs are mainly caused by Lyα photons escaping from the main body and then

scattered in the circum-galactic medium. This argument is supported by LAH observations of Hα emitters (HAEs). When LAHs are taken into account, the Lyα escape fractions of our LAEs are about ten times higher than those of HAEs with similar $M_\star$ or $E(B-V)_\star$, which may partly arise from lower HI gas masses implied from lower $M_{\rm h}$ at fixed $M_\star$, or from another Lyα source in the central part.

Key words: galaxies: high-redshift — galaxies: star formation — galaxies: halos —intergalactic medium

1 Introduction

A Lyα halo (LAH) is a diffuse, spatially extended structure of Lyα emission seen around star-forming galaxies. LAHs around local galaxies, as well as around active galactic nuclei (AGNs) and quasi-stellar objects (QSOs), can be detected individually because they are relatively bright (e.g., Keel et al. 1999; Kunth et al. 2003; Hayes et al. 2005; Goto et al. 2009; Östlin et al. 2009; Hayes et al. 2013; Matsuda et al. 2011, and reference therein). LAHs around high-z galaxies are much fainter, but they have been detected in stacked narrow-band images (tuned to redshifted Lyα emission) of 100 – 4000 star-forming galaxies at $z\sim2$–6 (e.g., Hayashino et al. 2004; Steidel et al. 2011; Matsuda et al. 2012; Feldmeier et al. 2013; Momose et al. 2014, 2016; Xue et al. 2017, see also a stacking study of spectra of ~80 LAEs at $z\sim2$–4 by Guaita et al. (2017)). Very recently, LAHs around ~170 star forming galaxies at $z\sim3$–6 have been detected individually by deep integral field spectroscopy with VLT/MUSE (Wisotzki et al. 2016; Leclercq et al. 2017). Since the existence of LAHs has now been established, the next question is what is their physical origin(s).

Theoretical studies have proposed several physical origins of LAHs: resonant scattering in the CGM, cold streams (gravitational cooling radiation), star formation in satellite galaxies (one-halo term), fluorescence (photo-ionization), shock heating by gas outflows, and major mergers (e.g., Haiman et al. 2000; Taniguchi & Shioya 2000; Cantalupo et al. 2005; Mori & Umemura 2006; Laursen & Sommer-Larsen 2007; Zheng et al. 2011; Rosdahl & Blaizot 2012; Yajima et al. 2013; Lake et al. 2015; Mas-Ribas & Dijkstra 2016). The former three are generally considered for high-z star-forming galaxies (e.g., Lake et al. 2015), while the latter three are preferred for giant Lyα nebulae (Lyα blobs; LABs) and/or bright QSOs (e.g., Kollmeier et al. 2010; Mori & Umemura 2006; Yajima et al. 2013).

Understanding the origin of LAHs provides crucial information on the circum-galactic medium (CGM), which is closely linked to galaxy formation and evolution. It also enables us to estimate the escape fraction of Lyα emission from central galaxies correctly. If resonant scattering mainly drives LAHs, the Lyα luminosity of LAHs should be included in the calculation of the Lyα escape fraction. LAHs are also important for studies of cosmic reionization because their spatial extent can be used as a probe of the IGM ionization fraction.

Lyman α emitters (LAEs) are suitable objects for studying the nature of LAHs because a large sample of LAEs at a fixed redshift as needed for a stacking analysis can be constructed relatively easily from a narrow-band imaging survey (Matsuda et al. 2012; Feldmeier et al. 2013; Momose et al. 2014, 2016; Xue et al. 2017). LAEs are typically low-stellar-mass young galaxies with low metallicities and low-dust contents hosted in low-mass dark matter halos (e.g., Pirzkal et al. 2007; Lai et al. 2008; Ono et al. 2010; Nakajima & Ouchi 2014; Kusakabe et al. 2015; Kojima et al. 2017; Ouchi et al. 2018, and reference therein). They are detected owing to efficient Lyα escapes, which are suggested to stem partly from these physical properties such as low-dust attenuation (e.g., Finkelstein et al. 2009).

Matsuda et al. (2012) have found that LAEs in a large-scale overdense region at $z=3.1$ have large ($\sim$ 100–200 Å) EWs if LAH components are included. They suggest that those LAHs may partly originate from shock heating due to gas outflows or cold streams, although they have not ruled out other possibilities. On the other hand, Momose et al. (2016) have stacked ~3600 LAEs in field regions at $z\sim2$ to find that some subsamples have relatively small Lyα EWs fully consistent with pop II star formation, suggesting that the cold stream scenario is not preferred. Finding no correlation between the spatial extent (the scale length, r_s) and the surface number density for LAEs at $z\sim3$–4, Xue et al. (2017) have suggested that star formation in satellite galaxies is not the dominant contributor to LAHs (see however, Matsuda et al. 2012). They have also found that the radial profile of LAHs is very close to that predicted by models of resonant scattering in Dijkstra & Kramer (2012), leaving only little room for the contribution from satellites galaxies and cold streams modeled by Lake et al. (2015). Note, however, that Lake et al. (2015)'s model reproduces the radial profile of LAHs seen in LAEs at $z\sim3$ in Momose et al. (2014). More recently, Leclercq et al. (2017) have measured LAH properties of ~150 individual LAEs at $z\sim3$–6 using VLT/MUSE. They argue that a significant contribution from star formation in satellite galaxies is somewhat unlikely since the UV component of LAEs is compact and not spatially offset from the center of their LAHs, while having not given a firm conclusion on other origins.

To summarize, although there are a number of observational studies on the origin of LAHs, their results are not very conclusive, nor consistent with each other (Matsuda et al. 2012;

Feldmeier et al. 2013; Momose et al. 2016; Wisotzki et al. 2016; Xue et al. 2017; Leclercq et al. 2017, see also Steidel et al. (2011)). This is partly because correlations of LAH properties with properties of central galaxies have not been fully studied. Especially important may be correlations with the dark matter halo mass and stellar mass of central galaxies, because they can be directly compared with theoretical predictions (e.g., Rosdahl & Blaizot 2012). Although Leclercq et al. (2017) have discussed a correlation between the Lyα luminosity of LAHs and the UV luminosity of central galaxies, they have not estimated those masses. $SFRs$ and dust attenuation are also important quantities to discuss the scattering origin of LAHs.

Another problem is that r_s, a quantity of LAHs that is often used to discuss the origin of LAHs in previous studies, is not robust against measurement errors. Indeed, the dependence of r_s on Lyα luminosity found in individually detected MUSE LAEs is not consistent with the average dependence obtained by Momose et al. (2016) from stacked images. In contrast, as we will see later, relations between the Lyα luminosity of central galaxies and that of LAHs found in Momose et al. (2016) is in good agreement with those seen in individual MUSE-LAEs in Leclercq et al. (2017). This suggests that Lyα luminosity is more robust against systematic errors from stacking.

In this paper, we study the dependence of LAH luminosity on stellar properties and dark matter halo mass using ~ 900 star-forming LAEs at $z \sim 2$ to identify the dominant origin of LAHs around LAEs. Section 2 summarizes the data and sample used in this study. In section 3, we construct subdivided samples based on UV, Lyα, and K-band properties. We present methods to derive the Lyα luminosities of LAHs as well as the stellar properties and dark matter halo masses of subdivided LAEs in section 4. After showing results in section 5, we discuss the origin of LAHs and high Lyα escape fractions in section 6. Conclusions are given in Section 7.

Throughout this paper, we adopt a flat cosmological model with the matter density $\Omega_{\rm m} = 0.3$, the cosmological constant $\Omega_\Lambda = 0.7$, the baryon density $\Omega_b = 0.045$, the Hubble constant $H_0 = 70\ {\rm km s^{-1} Mpc^{-1}}$ ($h_{100} = 0.7$), the power-law index of the primordial power spectrum $n_{\rm s} = 1$, and the linear amplitude of mass fluctuations $\sigma_8 = 0.8$, which are consistent with the latest Planck results (Plank Collaboration 2016). We assume a Salpeter initial mass function (IMF: Salpeter 1955)[1]. Magnitudes are given in the AB system (Oke & Gunn 1983) and coordinates are given in J2000. Distances are expressed in comoving units. We use "log" to denote a logarithm with a base 10 ($\log_{10}$).

[1] To rescale stellar masses in previous studies assuming a Chabrier or Kroupa IMF (Kroupa 2001; Chabrier & Chabrier 2003), we divide them by a constant factor of 0.61 or 0.66, respectively. Similarly, to convert SFRs in the literature with a Chabrier or Kroupa IMF, we divide them by a constant factor of 0.63 or 0.67, respectively.

2 Data and Sample

2.1 Sample Selection

Kusakabe et al. (2018) have constructed large samples of $z = 2.2$ LAEs in four deep fields: the Subaru/XMM-Newton Deep Survey (SXDS) field (Furusawa et al. 2008), the Cosmic Evolution Survey (COSMOS) field (Scoville et al. 2007), the Hubble Deep Field North (HDFN: Capak et al. 2004), and the Chandra Deep Field South (CDFS: Giacconi et al. 2001).In this study, we only use their SXDS and COSMOS samples. We do not use the HDFN sample because the R-band image of this field is not deep enough to derive the UV slope for faint LAEs. We also do not use the CDFS sample because the i, z, and H data are too shallow to perform reliable SED fitting as has been pointed out by Kusakabe et al. (2018).

We summarize the sample selection and the estimation of the contamination fraction detailed in Kusakabe et al. (2018). LAEs at $z = 2.14$–2.22 are selected using the narrow band $NB387$ (Nakajima et al. 2012) as described in selection papers (Nakajima et al. 2012, 2013; Konno et al. 2016; Kusakabe et al. 2018). The threshold of the rest-frame equivalent width, EW_0, of Lyα emission is $EW_0({\rm Ly}\alpha) \geq 20$–$30$Å (see figure 1 in Konno et al. 2016). The $NB387$ limiting magnitude is 25.7 mag for the SXDS sample and 26.1 mag for the COSMOS sample ($2''$ diameter aperture, 5σ). We only use LAEs with $NB387$ total (i.e., aperture-corrected; see table 1) magnitude brighter than 25.5 mag. All sources detected in either X-ray, UV, or radio have been removed since they are regarded as AGNs. Our entire sample consists of 897 LAEs from $\simeq 1980$ square arcminutes (The survey area of each field is shown in table 1).

Kusakabe et al. (2018) have conservatively estimated the fraction of possible interlopers in their LAE samples to be $10 \pm 10\%$, where interlopers are categorized into spurious sources, AGNs without an X-ray, UV, or radio counterpart, foreground/background galaxies, and $z = 2.2$ LAEs with low $EW_0({\rm Ly}\alpha)$ which happen to meet the color selection due to photometric errors. See sections 2.2 and 3.2 of Kusakabe et al. (2018) for details. We use this contamination fraction to obtain true clustering amplitudes from observed ones in section 4.3.1.

2.2 Imaging Data for SED Fitting

Most of the data used in this work are the same as those used in Kusakabe et al. (2018), except that the NIR imaging data are replaced to new ones in this work. We overview the data used in SED fitting in the two fields below.

We use ten broadband images for SED fitting: five optical bands – B, V, R (or r), i (or i'), and z (or z'); three NIR bands – J, H, and K (or Ks); and two mid-infrared (MIR) bands – IRAC ch1 and ch2. The PSFs of the images are matched in each field. The aperture corrections to convert $3''$ MIR aperture magnitudes to total magnitudes are taken from Ono et al. (2010,

see table1). For each field, a K-band or NIR detected catalog is used to obtain secure IRAC photometry in section 4.2.1 and to divide the LAEs into subsamples in section 3.2.

SXDS field The images used for SED fitting are as follows: B, V, R, i', and z' images with Subaru/Suprime-Cam from the Subaru/XMM-Newton Deep Survey project (Furusawa et al. 2008, SXDS); J, H, and K images from the data release 11 of the UKIRT/WFCAM UKIDSS/UDS project (Lawrence et al. 2007, Almaini et al. in prep.); Spitzer/IRAC 3.6 μm (ch1) and 4.5 μm (ch2) images from the Spitzer Large Area Survey with Hyper-Suprime-Cam (SPLASH) project (SPLASH; PI: P. Capak; Capak et al. in prep.; Mehta et al. 2017). All images are publicly available except the SPLASH data. The aperture corrections for optical and NIR images are given in Nakajima et al. (2013). The catalog used to clean IRAC photometry and to obtain K-band counterparts is constructed from the K-band image.

COSMOS field We use the publicly available B, V, r', i', and z' images with Subaru/Suprime-Cam by the Cosmic Evolution Survey (COSMOS: Capak et al. 2007; Taniguchi et al. 2007) and J, H, and Ks images with the VISTA/VIRCAM from the third data release of the UltraVISTA survey (McCracken et al. 2012). We also use Spitzer/IRAC ch1 and ch2 images from the SPLASH project (Laigle et al. 2016). The aperture corrections for the optical images are taken from Nakajima et al. (2013) and those for the NIR images follow McCracken et al. (2012). The catalog used to clean IRAC photometry and to obtain K-band counterparts is the one given by Laigle et al. (2016), for which sources have been detected in a combined z'YJHKs image.

3 Subsamples

A vast majority of our LAEs are too faint to estimate stellar masses on individual basis. To study how LAH luminosity depends on stellar and dark matter halo masses, we therefore divide the entire sample into subsamples in accordance with the following five quantities which are expected to correlate with stellar mass, and perform a stacking analysis on each subsample. (i) K-band apparent magnitude, $m_{\rm K}$, known as a good tracer of stellar mass (e.g., Bell et al. 2003). (ii) Rest-frame UV absolute magnitude, $M_{\rm UV}$, which is related to SFR and hence expected to trace stellar mass through the star formation main sequence (e.g., Speagle et al. 2014). (iii) UV spectral slope β ($f_\lambda \propto \lambda^\beta$), an indicator of dust attenuation and may correlate with stellar mass (e.g., Reddy et al. 2010). (iv) Lyα luminosity $L({\rm Ly}\alpha)$ and (v) rest-frame Lyα equivalent width $EW_0({\rm Ly}\alpha)$, both of which possibly anti-correlate with stellar mass according to Ando relation (Ando et al. 2006, 2007, see also Shimakawa et al. (2017)).

While only 30–40% of our LAEs are detected in the K band with $m_{\rm K} \lesssim 25.0$ (see section 3.2), the other four quantities can be measured for almost all objects because they need only optical imaging data, which are deep enough as shown in table 1. We divide the whole sample of each field into two subsamples in accordance with each of $m_{\rm K}$, $M_{\rm UV}$, β, $L({\rm Ly}\alpha)$, and $EW_0({\rm Ly}\alpha)$; further division makes stacked SEDs too noisy to do reliable SED fitting. Among the five quantities, m_K and $M_{\rm UV}$ are expected to correlate with $M_\star$ most tightly. The subsamples by β, $L({\rm Ly}\alpha)$, and $EW_0({\rm Ly}\alpha)$ are useful to check the results obtained for the m_K and $M_{\rm UV}$ subsamples, because these three quantities are affected by the NB selection bias differently from m_K and $M_{\rm UV}$ as discussed in appendix 1 (see figure 1). As shown later, all five subsample pairs give similar results.

3.1 UV and Lyα properties

For each object, we measure $M_{\rm UV}, \beta, L({\rm Ly}\alpha)$, and $EW_0({\rm Ly}\alpha)$ from $NB387$, B, V, and R magnitudes in the following manner. First, we approximate the UV SED of the object by a simple SED composed of a power-law continuum and a Lyα line centered at rest-frame 1216 Å:

$$f_\nu \quad ({\rm erg\,s^{-1}\,cm^{-2}\,Hz^{-1}}) = A \times 10^{-0.4(m_{\rm UV}+48.60)} \tag{1}$$

$$\times \left(\frac{\lambda\nu}{\lambda_{UV}}\right)^{\beta+2} + F_{{\rm Ly}\alpha} \times \delta(\lambda - 1216), \tag{2}$$

where A, $m_{\rm UV}$, and $F_{{\rm Ly}\alpha}$ are the intergalactic medium (IGM) attenuation factor from Madau (1995), the apparent UV magnitude (corresponding to $M_{\rm UV}$), and the Lyα flux (${\rm erg\,s^{-1}\,cm^{-2}}$), respectively. The apparent magnitude of the model SED in a given band i is calculated from its transfer function $T_i(\lambda)$ as below:

$$m_{i,model} = -2.5 \log \left(\frac{\int f_\nu c/\lambda^2 T_i(\lambda) d\lambda}{\int c/\lambda^2 T_i(\lambda) d\lambda} \right) - 48.6, \tag{3}$$

where c is the speed of light.

We fit this model SED to the apparent magnitudes of the object with $M_{\rm UV}$, β, and $F_{{\rm Ly}\alpha}$ as free parameters. We search for the best-fit parameter values that minimize

$$\chi^2 = \Sigma_{i=NB,B,V,R} \left(\frac{m_i - m_{i,model}}{\sigma m_i} \right)^2, \tag{4}$$

where m_i and σm_i are the i-th band apparent magnitude and its 1 σ error, respectively. We calculate apparent magnitudes from $2''$ diameter aperture magnitudes (see Kusakabe et al. 2018) assuming that our LAEs are point sources in all four bands including $NB387$ which detects Lyα emission. We also assume that their Lyα lines are located at the peak of the response function of $NB387$ and do not correct for flux loss. The best-fit $F_{{\rm Ly}\alpha}$ is obtained by solving $\frac{\partial {\chi^2}}{\partial F_{{\rm Ly}\alpha}} = 0$. Hereafter, we refer to the $L({\rm Ly}\alpha)$ and $EW_0({\rm Ly}\alpha)$ obtained with the assumption of

Table 1. Details of the data.

band	SXDS ($\sim 1240\,\mathrm{arcmin}^2$, $600^{(a)}$ LAEs)				COSMOS ($\sim 740\,\mathrm{arcmin}^2$, $297^{(a)}$ LAEs)			
	PSF ($''$)	aperture diameter ($''$)	aperture correction (mag)	5σ limit (mag)	PSF ($''$)	aperture diameter ($''$)	aperture correction (mag)	5σ limit (mag)
	(1)	(2)	(3)	(4)	(1)	(2)	(3)	(4)
$NB387$	0.88	2.0	0.17	25.7	0.95	2.0	0.25	26.1
B	0.84	2.0	0.17	27.5–27.8	0.95	2.0	0.12	27.5
V	0.8	2.0	0.15	27.1–27.2	1.32	2.0	0.33	26.8
$R(r')$	0.82	2.0	0.16	27.0–27.2	1.04	2.0	0.19	26.8
$i'(I)$	0.8	2.0	0.16	26.9–27.1	0.95	2.0	0.12	26.3
z'	0.81	2.0	0.16	25.8 – 26.1	1.14	2.0	0.25	25.4
J	0.85	2.0	0.15	25.6	0.79	2.0	0.3	24.6–24.8
H	0.85	2.0	0.15	25.1	0.76	2.0	0.2	24.3–24.4
$K(Ks)$	0.85	2.0	0.16	25.3	0.75	2.0	0.2	23.9–24.6
IRAC ch1	1.7	3.0	0.52	$24.9^{(b)}$	1.7	3.0	0.52	$25.4^{(b)}$
IRAC ch2	1.7	3.0	0.55	$24.9^{(b)}$	1.7	3.0	0.55	$25.1^{(b)}$

Note. (1) The FWHM of the PSF, (2) aperture diameter in photometry, (3) aperture correction, and (4) 5σ limiting magnitude with a $2''$ diameter aperture are shown for each band. Values in parentheses show the area used in clustering analysis. (a) The number of LAEs in the SXDS field is slightly different from that in Kusakabe et al. (2018) since we use $NB387$ images before PSF matching to other selection-band images for photometry. (b) The limiting magnitude measured in areas with no sources (see Laigle et al. 2016; Mehta et al. 2017).

Table 2. Subsample definition.

subsample	criteria	COSMOS	SXDS	total
bright UV (MuvB)	$M_{UV} \leq -19.2\,\mathrm{mag}$	123 (123, 9)	293 (257, 52)	416 (380, 61)
faint UV (MuvF)	$M_{UV} > -19.2\,\mathrm{mag}$	173 (173, 13)	302 (257, 47)	475 (430, 60)
blue β (betaB)	$\beta \leq -1.6$	80 (80, 5)	389 (334, 74)	469 (414, 79)
red β (betaR)	$\beta > -1.6$	216 (216, 17)	206 (180, 25)	422 (396, 42)
bright Lyα (lyaB)	$L(\mathrm{Ly}\alpha)_{ps} \geq 1.2\times10^{42}\,\mathrm{erg\,s^{-1}}$	211 (211, 14)	236 (218, 41)	447 (429, 55)
faint Lyα (lyaB)	$L(\mathrm{Ly}\alpha)_{ps} < 1.2\times10^{42}\,\mathrm{erg\,s^{-1}}$	85 (85, 8)	359 (296, 58)	444 (381, 66)
large EW (ewL)	$EW_{0,ps}(\mathrm{Ly}\alpha) \geq 34\,\mathrm{\AA}$	222 (222, 16)	228 (205, 35)	450 (427, 51)
small EW (ewS)	$EW_{0,ps}(\mathrm{Ly}\alpha) < 34\,\mathrm{\AA}$	74 (74, 6)	367 (309, 64)	441 (383, 70)
bright K (KB)	$m_\mathrm{K} \leq 25\,\mathrm{mag}$	112 (112, 11)	178 (177, 35)	290 (144, 46)
faint K (KF)	$m_\mathrm{K} > 25\,\mathrm{mag}$	184 (184, 11)	417 (337, 64)	601 (236, 75)

Note. The selection criterion and the numbers of objects for each subsample. The number outside the bracket indicates the number of objects for clustering analysis, while the numbers in the bracket are for SED fitting: the left one corresponds to objects with UV to NIR photometry and the right one to those with clean ch1 and ch2 photometry.

point sources as $L(\mathrm{Ly}\alpha)_{ps}$ and $EW_{0,ps}(\mathrm{Ly}\alpha)$. Since the best-fit $EW_0(\mathrm{Ly}\alpha)$ is derived from the other three parameters, the degree of freedom is one.

Among the 897 LAEs, six sources are undetected in at least one of the three broad bands. We do not use these objects in the following analyses because the four quantities derived from the SED fitting are highly uncertain.

3.2 Subsample construction

Since we divide LAEs into two subsamples in accordance with each of the five quantities, we have a total of ten subsamples for each field. The boundaries of the subsamples are defined from the distribution of the five quantities, which is shown in figure 1.

Our LAEs are widely distributed over the four UV and Lyα properties as shown in panels (a) – (d) of this figure. The distribution of M_UV, β, $L(\mathrm{Ly}\alpha)_{ps}$, and $EW_{0,ps}(\mathrm{Ly}\alpha)$ is different between the two fields. This may be partly because of cosmic variance. Another possibility is that the zero-point magnitudes (ZPs) of the optical images adopted in the original papers may have systematic errors as discussed in Yagi et al. (2013) and Skelton et al. (2014), although these two papers often claim opposite error directions. In this paper, we use the original ZPs following Kusakabe et al. (2018). We define the boundary for the four UV and Lyα quantities so that the two subsamples have roughly comparable sizes:

$$M_\mathrm{UV} = -19.2\,\mathrm{mag}, \tag{5}$$

$$\beta = -1.6, \tag{6}$$

$$L(\mathrm{Ly}\alpha)_{ps} = 1.2\times10^{42}\,\mathrm{erg\,s^{-1}}, \tag{7}$$

and

$$EW_{0,ps}(\mathrm{Ly}\alpha) = 34\,\mathrm{\AA} \tag{8}$$

as indicated by black lines in figure 1 (a) – (d). The numbers of the LAEs in the eight subsamples are shown in table 2.

For each field, we also construct two subsamples divided by

$m_{\rm K}$. The K-band catalog mentioned in section 2.2 effectively include sources with $m_{\rm K} \lesssim 25$ mag. Indeed, the 5σ limiting magnitude of the SXDS K-band image is 25.3 mag and the detection image for the COSMOS catalog, a combined $z'YJHKs$ image, reaches deeper than 25.3 mag (5σ). As a result, about 30–40% of the LAEs in each field have a K-band counterpart with $m_{\rm K} < 25.0$ as shown in panel (e). Therefore, we define the K-magnitude boundary as:

$$m_{\rm K} = 25.0\,{\rm mag}. \quad (9)$$

Note that the COSMOS K image is composed of Deep and Ultradeep stripes. Since this could add an artificial pattern in the sky distribution of K-divided subsamples, we do not use the K-divided subsamples for clustering analysis.

We derive the four UV and Lyα quantities for each subsample from a median-stacked SED (see section 4.2) in the same manner as in section 3.1. We then calculate average values over the two field, e.g., the average $M_{\rm UV}$ of the two faint-$M_{\rm UV}$ subsamples, as shown by red symbols in panels (f) – (k). They are located in the middle of the distribution of individual sources (orange and green points), implying that the average SEDs of the subsamples represent well individual LAEs. We find that the subsamples with red β, faint $L({\rm Ly}\alpha)_{ps}$, small $EW_{0,ps}({\rm Ly}\alpha)$, and bright $m_{\rm K}$ as well as bright $M_{\rm UV}$ have bright $M_{\rm UV}$ as shown by red open symbols. Note that the lower left part in panels (g) and (h) and upper the left part in panel (k) show a selection bias: LAEs with faint $M_{\rm UV}$ can be detected only if they have bright $L({\rm Ly}\alpha)_{ps}$.

4 Methods

The Lyα luminosities of LAHs are estimated from a stacked observational relation obtained by Momose et al. (2016). We do not perform a stacking analysis of LAHs on our own subsamples since their sample sizes, which are one ninth to one half of Momose et al. (2016)'s, are not large enough to obtain reliable results. Parameters that characterize stellar populations and the mass of dark matter halos are derived from SED fitting and clustering analysis, respectively, in the same manner as in Kusakabe et al. (2018).

4.1 LAH luminosities

The LAHs of LAEs have been studied either by a stacking analysis of large samples or using individually detected objects. Momose et al. (2016) have used stacked images of ~ 3000 LAEs at $z \sim 2$ to compare Lyα luminosities within $r = 40$ kpc ($\sim 5''$) to those within $r = 1''$ (~ 8 kpc). On the other hand, Leclercq et al. (2017) have measured Lyα luminosities for $3 \leq z \leq 6$ LAEs with an individually detected LAH by fitting a two component model consisting of halo and continuum-like components. We define three kinds of Lyα luminosities as below.

$L({\rm Ly}\alpha)_C$ Lyα luminosity at the central part, i.e., the main body of the object where stars are being formed. In Leclercq et al. (2017), it corresponds to the continuum-like component of Lyα luminosities. We assume that the Lyα luminosities within $r = 1''$ in 2D images in Momose et al. (2016) are approximately equal to $L({\rm Ly}\alpha)_C$. The aperture size $r = 1''$ (~ 8 kpc) is often used in photometry with ground-based telescopes for point sources, since it is comparable to their typical PSF size and hence $r = 1''$ fluxes are nearly equal to total fluxes. Leclercq et al. (2017) show that the r_s of the continuum-like component of LAEs is typically smaller than 1 kpc, ensuring our assumption that LAEs are point sources.

$L({\rm Ly}\alpha)_H$ Lyα luminosity of the LAH. In Leclercq et al. (2017), it approximately corresponds to the halo component of Lyα luminosity. We assume that the Lyα luminosities falling in the annulus of $1'' \leq r \leq 40$ kpc in Momose et al. (2016) approximately equal to $L({\rm Ly}\alpha)_H$. In Momose et al. (2016), the typical r_s of stacked Lyα emission including the LAH component is ~ 10 kpc, and LAHs are found to extend up to $r \sim 40$ kpc.

$L({\rm Ly}\alpha)_{tot}$ Total Lyα luminosity. In Leclercq et al. (2017), it corresponds to a sum of $L({\rm Ly}\alpha)_C$ and $L({\rm Ly}\alpha)_H$. we assume that the Lyα luminosities within 40 kpc in Momose et al. (2016) approximately equal to $L({\rm Ly}\alpha)_{tot}$.

Momose et al. (2016) have found that LAEs with fainter $L({\rm Ly}\alpha)_C$ have a higher $L({\rm Ly}\alpha)_{tot}$ to $L({\rm Ly}\alpha)_C$ ratio, ${\rm X}(L_{{\rm Ly}\alpha})_{\rm tot/C}$, as shown in their figure 14. This means that the relative contribution of the halo component to the total Lyα luminosity increases with decreasing $L({\rm Ly}\alpha)_C$. The best-fitting linear function between ${\rm X}(L_{{\rm Ly}\alpha})_{\rm tot/C}$ and $L({\rm Ly}\alpha)_C$, shown as their equation 2 is:

$${\rm X}(L_{{\rm Ly}\alpha})_{\rm tot/C} = 103.6 - 2.4 \times \log 10[L({\rm Ly}\alpha)_C\,({\rm erg/s})]. \quad (10)$$

This equation is valid over $41.5 < \log 10(L({\rm Ly}\alpha)_C) < 42.7$[2] and is shown in figure 2(d).

Leclercq et al. (2017) have used the MUSE Hubble Ultra Deep Field survey data to detect a LAH for 145 star forming galaxies (essentially all are LAEs) at $3 \leq z \leq 6$ individually. They have measured the size and $L({\rm Ly}\alpha)_H$ of Lyα halos as well as $L({\rm Ly}\alpha)_C$. They do not find a significant evolution of LAH size with redshift. This result is consistent with that obtained by Momose et al. (2014) with stacked LAEs at $z \simeq 2.2$–6.6, implying that the difference in redshift can be ignored in a comparison of the two studies.

In figure 2, we compare the stacked observational relation

[2] They use images with the PSF matched to $1.32''$ in FWHM. Here we have corrected a typo in their equation 2 and revised the range of $\log 10(L({\rm Ly}\alpha)_C)$.

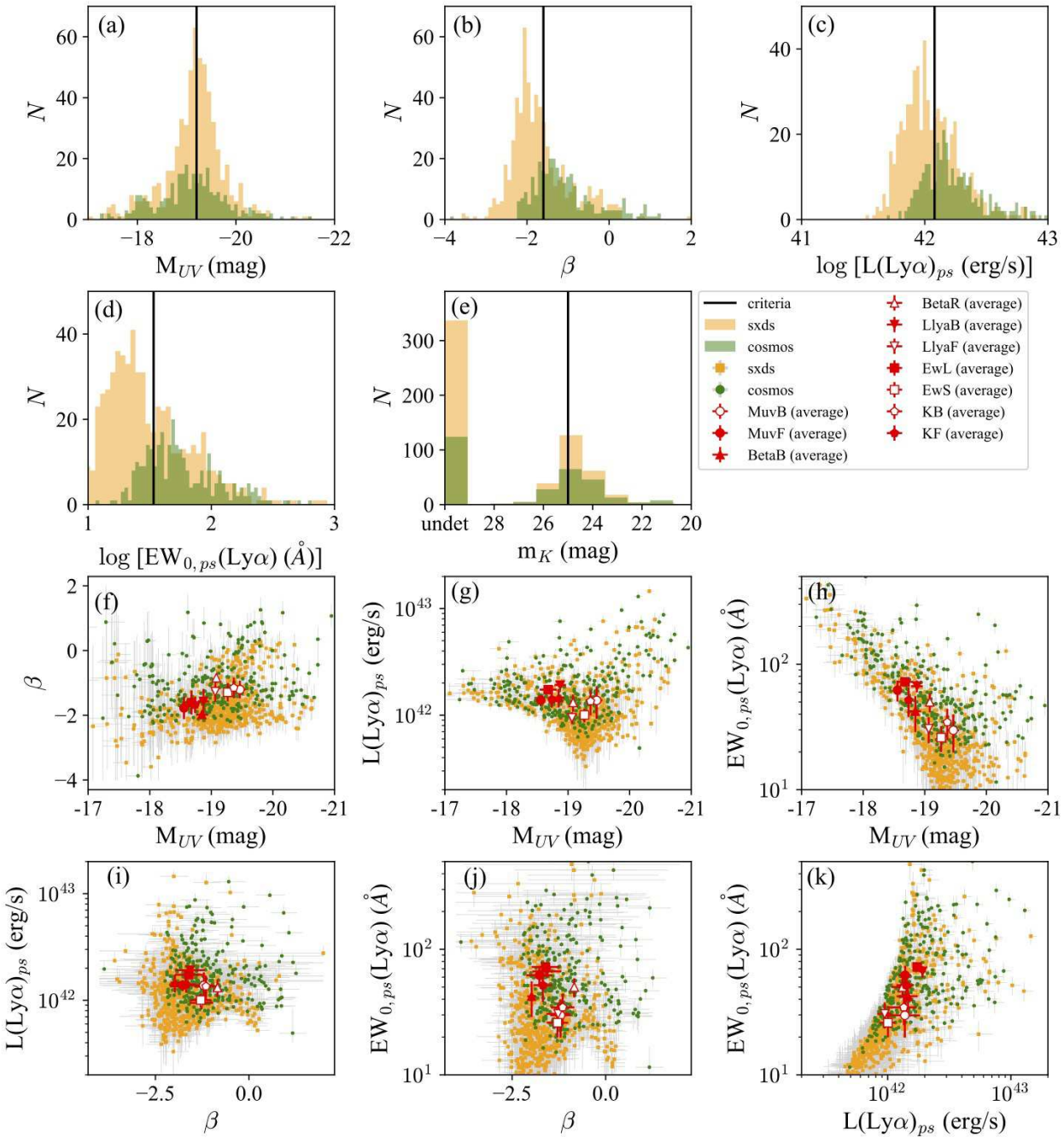

Fig. 1. The distribution of the five quantities used to divide our LAEs into subsamples. Panels (a) – (e) show histograms: (a) $M_{\rm UV}$, (b) β, (c) $L({\rm Ly}\alpha)_{ps}$, (d) $EW_{0,ps}({\rm Ly}\alpha)$, and (e) $m_{\rm K}$, with orange and green colors corresponding to the SXDS and COSMOS fields, respectively. Black lines indicate the boundaries of the two subsamples. Panels (f) – (k) are scatter plots: (f) β vs. $M_{\rm UV}$, (g) $L({\rm Ly}\alpha)_{ps}$ vs. $M_{\rm UV}$, (h) $EW_{0,ps}({\rm Ly}\alpha)$ vs. $M_{\rm UV}$, (i) $L({\rm Ly}\alpha)_{ps}$ vs. β, (j) $EW_{0,ps}({\rm Ly}\alpha)$ vs. β, and (k) $EW_{0,ps}({\rm Ly}\alpha)$ vs. $L({\rm Ly}\alpha)_{ps}$, with the same color coding as panels (a)–(d). Red symbols represent averages over the two fields, where different symbols correspond to different classifications: open (filled) circles for bright (faint) $M_{\rm UV}$, open (filled) triangles for red (blue) β, open (filled) inverted triangles for faint (bright) $L({\rm Ly}\alpha)_{ps}$, open (filled) squares for large (small) EW, and open (filled) pentagons for bright (faint) $m_{\rm K}$.

of LAEs at $z = 2.2$ in Momose et al. (2016) (black lines and red stars) with the individual results by Leclercq et al. (2017) (gray circles), where X(Ly$\alpha)_{x/y}$ indicates the Lyα luminosity ratio of component x to component y. In every panel of figure 2, we find that all five stacked data points (red stars) lie in the middle of the distribution of individual MUSE-LAEs (grey circles) over a range of $\log 10[L({\rm Ly}\alpha)_C({\rm erg/s})] \simeq 41.7$–$42.6$ or $\log 10[L({\rm Ly}\alpha)_{tot}({\rm erg/s})] \simeq 42.3$–$42.8$. This means that the stacked results represent the average halo luminosities of LAEs despite the fact that there is a great variation in halo luminosity among objects. The best-fit relation shown by a black line traces well the stacked points except for the brightest one. This

is because the brightest point already deviates from the best-fit linear relation determined in panel (d) while the other four are on the relation. Based on panel (a), Leclercq et al. (2017) have concluded that there is no significant correlation between $L(\mathrm{Ly}\alpha)_{tot}$ and $\mathrm{X}(\mathrm{Ly}\alpha)_{\mathrm{H/tot}}$ on the basis of a Spearman rank correlation coefficient of -0.05 (see their figure 7 and their section 5.3.1). However, in each of the six panels including (a), we can see a positive or negative correlation in the stacked data points although the strength and slope of the correlation vary from panel to panel.

In this work, we estimate average $L(\mathrm{Ly}\alpha)_H$ and $L(\mathrm{Ly}\alpha)_{tot}$ for each subsample from the stacked relation (equation10) as well as average $L(\mathrm{Ly}\alpha)_C$ by multiplying average $L(\mathrm{Ly}\alpha)_{ps}$ (in section 3.1) by 0.77 as an inverse aperture correction of $1.32''$ PSF (see table 5 in appendix). The $L(\mathrm{Ly}\alpha)_C$ values of our subsamples are found to be within the range shown by skyblue inverted triangles in panels (e) and (f) where the stacked relation traces well the stacked points. The typical 1σ uncertainties in the individual data points in Momose et al. (2016) are propagated to uncertainties in $L(\mathrm{Ly}\alpha)_H$ and $L(\mathrm{Ly}\alpha)_{tot}$ of $\sim 22\%$ and $\sim 16\%$, respectively. Momose et al. (2016) also present a stacked relation (anti-correlation) between $\mathrm{X}(L_{\mathrm{Ly}\alpha})_{\mathrm{tot/C}}$ and $EW_{0,ps}(L_{\mathrm{Ly}\alpha})$. Using this relation instead of equation 10 gives nearly the same $L(\mathrm{Ly}\alpha)_H$ and $L(\mathrm{Ly}\alpha)_{tot}$ values (see appendix 3).

4.2 SED fitting

We derive parameters that characterize the stellar populations of our subsamples in the two fields by fitting SEDs based on stacked multiband images. We use 810 LAEs ($\sim 91\%$ of the entire sample, 891) that have data in all ten broadband filters (B, V, R, i, z, J, H, K, ch1, and ch2). To obtain secure IRAC photometry, some prescriptions are adopted in previous studies (e.g., Vargas et al. 2014; Kusakabe et al. 2018; Malkan et al. 2017). In this paper, we follow Kusakabe et al. (2018) and only use LAEs that are not contaminated by other objects in the ch1 and ch2 images. To do so, we exclude LAEs that have either one or more neighbors or a high sky background through a two-step cleaning process. We are thus left with 121 LAEs for stacking of ch1 and ch2 images (see section 4.1 in Kusakabe et al. 2018, for more detail). We briefly describe stacking analysis, photometry, and SED models below. A detailed description can be found in Kusakabe et al. (2018).

4.2.1 Stacking Analysis and Photometry

For each band, we use the task IRAF/imcombine to create a $NB387$–centered median-stacked image from images of size $50'' \times 50''$ that are cut out with IRAF/imcopy task. While a stacked SED is not necessarily a good representation of individual objects (Vargas et al. 2014), stacking is still useful for our faint objects to obtain a rest-frame UV to NIR SED.

An aperture flux is measured for each stacked image using the task PyRAF/phot with the same parameters in Kusakabe et al. (2018). We use an aperture diameter of $2''$ for the $NB387$, optical, and NIR band images and $3''$ for the MIR (IRAC) images following Ono et al. (2010). For each of the ch1 and ch2 images, we obtain the net $3''$-aperture flux density by subtracting an offset of the sky background as described in section 4.2 of Kusakabe et al. (2018). All aperture magnitudes are corrected for Galactic extinction, $\mathrm{E(B-V)_b}$, of 0.020 and 0.018 for the SXDS and COSMOS fields, respectively (Schlegel et al. 1998).

The aperture magnitudes are converted into total magnitudes using the aperture correction values summarized in table 1. The 1σ uncertainty in the total magnitudes is the sum of the errors in photometry, aperture correction, and the ZP. For the ch1 and ch2 data, the errors in sky subtraction are also included. The photometric errors are determined in the same procedure as Kusakabe et al. (2015). The aperture correction errors in the $NB387$, optical, and NIR bands are estimated to be 0.03 mag, and those in the ch1 and ch2 bands are set to 0.05 mag. The ZP errors for all bands are set to be 0.1 mag. The stacked SEDs thus obtained for individual subsamples are shown in figures 11 and 12 in appendix.

4.2.2 SED Models

We perform SED fitting on the stacked SEDs with model SEDs in the same manner as in Kusakabe et al. (2018). The model SEDs are constructed by adding nebular emission (lines and continuum) to the stellar population synthesis model GALAXEV (Bruzual & Charlot 2003; Ono et al. 2010). We assume constant star formation history, $0.2Z_\odot$ stellar metallicity, and $\mathrm{E(B-V)_{gas}} = \mathrm{E(B-V)}_\star$ (Erb et al. 2006) following previous SED studies of LAEs (e.g., Ono et al. 2010; Vargas et al. 2014). We also assume a SMC-like dust extinction model for the attenuation curve (hereafter a SMC-like attenuation curve; Gordon et al. 2003) since it is suggested to be more appropriate for LAEs at $z \sim 2$ and low-mass star forming galaxies at $z \geq 2$ than the Calzetti curve (Calzetti et al. 2000) in Kusakabe et al. (2015) and Reddy et al. (2018), respectively. The Lyman continuum escape fraction, $f_{\mathrm{esc}}^{\mathrm{ion}}$, is fixed to 0.2 (Nestor et al. 2013). We also examine the case of the Calzetti attenuation curve for comparison with previous studies and conservative discussion. The case without nebular emission ($f_{\mathrm{esc}}^{\mathrm{ion}} = 1$) has been examined and discussed in Kusakabe et al. (2018).

We search for the best-fitting model SED to the stacked SED of each subsample that minimizes χ^2 and derive the following stellar parameters: stellar mass ($M_\star$), color excess ($\mathrm{E(B-V)}_\star$), age, and SFR. The stellar mass is calculated by solving $\frac{\partial \chi^2}{\partial M_\star} = 0$, while the SFR is determined from $M_\star$ and age. Thus, the degree of freedom is 7. The 1σ confidence interval in these stellar parameters is estimated from $\chi^2_{\mathrm{min}} + 1$, where

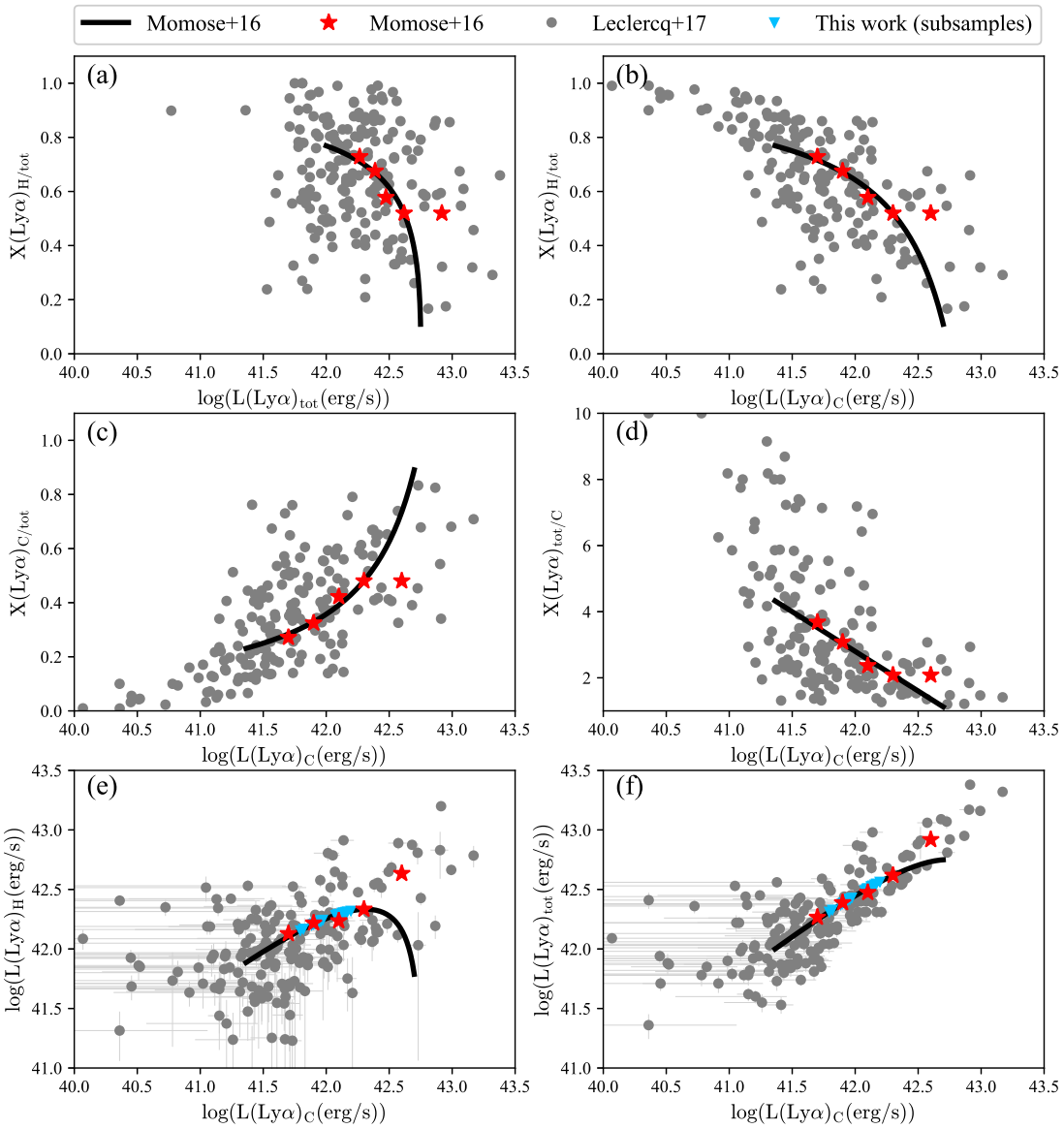

Fig. 2. Relation between $L(\mathrm{Ly}\alpha)_H$ and $L(\mathrm{Ly}\alpha)_C$ in six different presentations. (a) $L(\mathrm{Ly}\alpha)_H/L(\mathrm{Ly}\alpha)_{tot}$ vs. $L(\mathrm{Ly}\alpha)_{tot}$; (b) $L(\mathrm{Ly}\alpha)_H/L(\mathrm{Ly}\alpha)_{tot}$ vs. $L(\mathrm{Ly}\alpha)_C$; (c) $L(\mathrm{Ly}\alpha)_C/L(\mathrm{Ly}\alpha)_{tot}$ vs. $L(\mathrm{Ly}\alpha)_C$; (d) $L(\mathrm{Ly}\alpha)_{tot}/L(\mathrm{Ly}\alpha)_C$ vs. $L(\mathrm{Ly}\alpha)_C$; (e) $L(\mathrm{Ly}\alpha)_H$ vs. $L(\mathrm{Ly}\alpha)_C$; and (f) $L(\mathrm{Ly}\alpha)_{tot}$ vs $L(\mathrm{Ly}\alpha)_C$. Red stars and black lines indicate, respectively, the stacked results and their best-fit relation given by Momose et al. (2016). The best-fit linear relation is determined in panel (d) and is shown in equation 10. Grey points represents MUSE–LAEs at $z \sim 3-6$ Leclercq et al. (2017), where error are only shown in panels (e) and (f). Skyblue inverted triangles in panels (e) and (f) show the $L(\mathrm{Ly}\alpha)_H$ and $L(\mathrm{Ly}\alpha)_{tot}$ of our subsamples calculated from $L(\mathrm{Ly}\alpha)_C$ using the stacked observational relation in Momose et al. (2016). (Color online)

$\chi^2_{\rm min}$ is the minimum χ^2 value. Figures 11 and 12 in appendix shows the best-fit SEDs and table 6 in appendix summarize the results of the best-fit parameters in the two fields. The field-average values are shown in table 3.

4.3 Clustering Analysis

We derive the angular two-point correlation functions (ACFs) of our subsamples from clustering analysis and convert the correlation lengths into bias factors and then into dark matter halo masses in the same manner as in Kusakabe et al. (2018). We

Table 3. The field-average values of stellar parameters, $f_{\rm esc}({\rm Ly}\alpha)_{\rm tot}$, and the q-parameter.

subsample	$M_\star$ ($10^8 M_\odot$) (1)	$E(B-V)_\star$ (mag) (2)	Age (Myr) (3)	SFR ($M_\odot {\rm yr}^{-1}$) (4)	$f_{\rm esc}({\rm Ly}\alpha)_{\rm tot}$ (5)	q-parameter (6)
SMC-like attenuation curve						
bright UV	14.1 ± 2.1	0.08 ± 0.01	240 ± 14	6.8 ± 1.3	0.37 ± 0.00	$0.80^{+0.11}_{+0.09}$
faint UV	4.1 ± 0.1	0.03 ± 0.01	280 ± 46	1.7 ± 0.3	1.43 ± 0.17	$-0.69^{+0.30}_{+0.62}$
blue β	4.8 ± 2.4	0.02 ± 0.00	246 ± 145	2.1 ± 0.0	1.21 ± 0.10	$-0.52^{+0.25}_{+0.27}$
red β	14.0 ± 0.9	0.10 ± 0.01	286 ± 0	5.8 ± 0.4	0.43 ± 0.08	$0.57^{+0.14}_{+0.11}$
bright Lyα	7.4 ± 0.8	0.04 ± 0.02	346 ± 80	2.2 ± 0.7	1.20 ± 0.35	$-0.28^{+0.57}_{+0.57}$
faint Lyα	12.3 ± 1.0	0.07 ± 0.01	360 ± 0	4.2 ± 0.3	0.49 ± 0.00	$0.64^{+0.10}_{+0.08}$
large EW	5.4 ± 1.6	0.04 ± 0.02	338 ± 19	1.8 ± 0.6	1.34 ± 0.42	$-0.46^{+0.60}_{+0.71}$
small EW	13.7 ± 3.4	0.07 ± 0.01	353 ± 40	5.0 ± 0.7	0.42 ± 0.02	$0.79^{+0.14}_{+0.11}$
bright K	18.3 ± 2.2	0.09 ± 0.01	265 ± 84	6.5 ± 1.2	0.36 ± 0.01	$0.72^{+0.09}_{+0.08}$
faint K	3.6 ± 0.4	0.04 ± 0.01	160 ± 44	2.3 ± 0.2	1.03 ± 0.04	$-0.04^{+0.06}_{+0.07}$
the Calzetti attenuation curve						
bright UV	12.9 ± 1.6	0.15 ± 0.02	118 ± 21	11.7 ± 3.4	0.20 ± 0.02	$0.96^{+0.16}_{+0.12}$
faint UV	2.9 ± 0.3	0.10 ± 0.03	73 ± 37	3.3 ± 1.3	0.74 ± 0.25	$0.27^{+0.46}_{+0.26}$
blue β	3.4 ± 2.4	0.06 ± 0.02	106 ± 112	2.9 ± 0.6	0.87 ± 0.08	$0.21^{+0.21}_{+0.14}$
red β	13.7 ± 2.6	0.18 ± 0.00	133 ± 30	11.8 ± 0.3	0.21 ± 0.02	$0.78^{+0.05}_{+0.05}$
bright Lyα	4.2 ± 0.6	0.14 ± 0.05	39 ± 24	6.1 ± 4.2	0.43 ± 0.29	$0.55^{+1.06}_{+0.34}$
faint Lyα	12.0 ± 1.2	0.14 ± 0.02	189 ± 11	7.1 ± 1.1	0.27 ± 0.02	$0.84^{+0.15}_{+0.11}$
large EW	3.7 ± 0.8	0.14 ± 0.03	60 ± 11	4.9 ± 2.6	0.50 ± 0.24	$0.46^{+0.51}_{+0.26}$
small EW	13.2 ± 3.6	0.14 ± 0.02	191 ± 11	8.8 ± 1.9	0.24 ± 0.03	$0.92^{+0.18}_{+0.13}$
bright K	11.2 ± 2.7	0.20 ± 0.02	46 ± 24	17.9 ± 6.4	0.13 ± 0.02	$0.93^{+0.14}_{+0.11}$
faint K	2.3 ± 0.9	0.11 ± 0.03	32 ± 25	4.1 ± 1.8	0.56 ± 0.18	$0.49^{+0.46}_{+0.25}$

Note. (1) Stellar mass, (2) color excess, (3) age, (4) SFR, (5) $f_{\rm esc}({\rm Ly}\alpha)_{\rm tot}$ calculated from SFR and $L({\rm Ly}\alpha)_{tot}$, and (6) q calculated from $f_{\rm esc}({\rm Ly}\alpha)_{\rm tot}$ and $E(B-V)_\star$.

briefly describe our methods below.

4.3.1 Angular Correlation Function

The ACF, $\omega_{\rm obs}(\theta)$, for a given subsample is measured by the calculator given in Landy & Szalay (1993):

$$\omega_{\rm obs}(\theta) = \frac{DD(\theta) - 2DR(\theta) + RR(\theta)}{RR(\theta)}, \tag{11}$$

where DD(θ), RR(θ), and DR(θ) are the normalized numbers of galaxy-galaxy, galaxy-random, and random-random pairs, respectively. We use a random sample composed of $100,000$ sources with the same geometrical constraints as the data sample. The sky distributions of the LAEs and the random sources in the two fields are shown in figure 2 of Kusakabe et al. (2018). Following Guaita et al. (2010), the $1\,\sigma$ uncertainties in ACF measurements are estimated as:

$$\Delta\omega_{\rm obs}(\theta) = \frac{1+\omega(\theta)}{\sqrt{DD_0(\theta)}}, \tag{12}$$

where $DD_0(\theta)$ is the raw number of galaxy-galaxy pairs.

We approximate the spatial correlation function of LAEs by a power law:

$$\xi(r) = \left(\frac{r}{r_0}\right)^{-\gamma}, \tag{13}$$

where r, r_0, and γ are the spatial separation between two objects in comoving scale, the correlation length, and the slope of the power law, respectively (Totsuji & Kihara 1969; Zehavi et al. 2004). We then convert $\xi(r)$ into the ACF, $\omega_{\rm model}(\theta)$, following Simon (2007), and describe it as:

$$\omega_{\rm model}(\theta) = \left(\frac{r_0\ h_{100}^{-1}{\rm Mpc}}{1\ h_{100}^{-1}{\rm Mpc}}\right)^{\gamma} \omega_{{\rm model},0}(\theta), \tag{14}$$

where $\omega_{{\rm model},0}(\theta)$ is the ACF in the case of $r_0 = 1\ h_{100}^{-1}{\rm Mpc}$. The correlation amplitude of the ACF at $\theta = 1''$, A_ω, is $\omega_{\rm model}(\theta = 1'')$.

An observationally obtained ACF, $\omega_{\rm obs}(\theta)$, includes an offset due to the fact that the measurements are made over a limited area. This offset is given by the integral constraint (IC),

$$\omega(\theta) = \omega_{\rm obs}(\theta) + IC, \tag{15}$$

$$IC = \frac{\Sigma_\theta RR(\theta)\,\omega_{{\rm model},0}(\theta)}{\Sigma_\theta RR(\theta)} \left(\frac{r_0\ h_{100}^{-1}{\rm Mpc}}{1\ h_{100}^{-1}{\rm Mpc}}\right)^{\gamma}, \tag{16}$$

where $\omega(\theta)$ is the true ACF. We fix γ to the fiducial value 1.8 following previous studies (e.g., Ouchi et al. 2003) and fit the $\omega_{\rm model}(\theta)$ to this $\omega(\theta)$ by minimizing χ^2 over $\sim 40'' - 1000''$, where we avoid the one-halo term at small scales and large sampling noise at large scales. The best-fit field-average correlation amplitude, A_ω, is calculated analytically by minimizing the summation of χ^2 over the two fields in the same manner as in Kusakabe et al. (2018). The $1\,\sigma$ fitting error in A_ω, ΔA_ω, is estimated from $\chi^2_{\rm min} + 1$, where $\chi^2_{\rm min}$ is the minimum χ^2 value.

The correlation amplitude corrected for randomly distributed foreground and background interlopers, $A_{\omega,\mathrm{corr}}$, is given by

$$A_{\omega,\mathrm{corr}} = \frac{A_\omega}{(1-f_\mathrm{c})^2}, \tag{17}$$

where f_c is the contamination fraction. The contamination fraction of our LAEs is estimated to be $10 \pm 10\%$ (0–20%) conservatively (see section 2.1) and the error range in $A_{\omega,\mathrm{corr}}$ includes both the no correction case and the maximum correction case (e.g., Khostovan et al. 2017). The $1\,\sigma$ error in the contamination-corrected correlation amplitude, $\Delta A_{\omega,\mathrm{corr}}$, is derived from error propagation of A_ω and f_c:

$$\frac{\Delta A_{\omega,\mathrm{corr}}}{A_{\omega,\mathrm{corr}}} \simeq \sqrt{\left(\frac{\Delta A_\omega}{A_\omega}\right)^2 + \left(\frac{2\Delta f_\mathrm{c}}{f_\mathrm{c}}\right)^2}, \tag{18}$$

where $\Delta f_\mathrm{c} (= 0.1)$ is the uncertainty in the contamination estimate. The value of the contamination-corrected correlation length, $r_{0,\mathrm{corr}}$ and its $1\,\sigma$ error are calculated from $A_{\omega,\mathrm{corr}}$ and $\Delta A_{\omega,\mathrm{corr}}$. Figure 13 in appendix shows the best-fit ACFs and table 4 summarizes the results of the clustering analysis.

4.3.2 Bias Factor and Dark Matter Halo Mass

The galaxy-matter bias, b_g, is defined as

$$b_\mathrm{g}(r) = \sqrt{\frac{\xi(r)}{\xi_\mathrm{DM}(r,z)}}, \tag{19}$$

where $\xi_\mathrm{DM}(r,z)$ is the spatial correlation function of underlying dark matter calculated with the linear dark matter power spectrum (Eisenstein & Hu 1998, 1999). We estimate the effective galaxy-matter bias, $b_{\mathrm{g,\,eff}}$, at $r = 8\,h_{100}^{-1}\mathrm{Mpc}$ following previous clustering analyses (e.g., Ouchi et al. 2003) using a suite of cosmological codes called Colossus (Diemer & Kravtsov 2015). The obtained $b_{\mathrm{g,\,eff}}$ is converted into the peak height in the linear density field, ν, by the formula given in Tinker et al. (2010). The effective dark matter halo mass is derived from ν with the top-hat window function and the linear dark matter power spectrum (Eisenstein & Hu 1998, 1999) using a cosmological package for Python called CosmoloPy[3]. The effective bias and the effective halo mass of each subsample is listed in table 4.

5 Results

The field-average results of the SED fitting and clustering analysis are shown in tables 3 and 4, respectively. In section 5.1, we compare the infrared excess (IRX) and star formation mode of our subsamples with the average relations of star forming galaxies to examine whether they are normal galaxies in terms of these two properties. Then, in sections 5.2 and 5.3, we focus on their LAH luminosities and Lyα escape fractions, respectively.

[3] http://roban.github.com/CosmoloPy/

5.1 IRX and Star Formation Mode

Star-forming galaxies have a positive correlation that more massive ones have higher $IRXs$. The $IRX \equiv L_\mathrm{IR}/L_\mathrm{UV}$ is an indicator of dustiness, where L_IR and L_UV are IR (8–1000μm) and UV (1530Å) luminosities, respectively (e.g., Reddy et al. 2010; Whitaker et al. 2014; Álvarez-Márquez et al. 2016; Fudamoto et al. 2017; McLure et al. 2017; Koprowski et al. 2018). Average $M_\star$-IRX relations have been obtained by several studies at $z \sim 2$ (Heinis et al. 2014; Bouwens et al. 2016). Another important correlation seen in star-forming galaxies is that more massive galaxies have higher $SFRs$, i.e., the star formation main sequence (SFMS; e.g., Noeske et al. 2007; Elbaz et al. 2007; Speagle et al. 2014). Outliers above the SFMS are star-burst galaxies (Rodighiero et al. 2011). We use these two correlations to test whether or not our LAEs are outliers in terms of dustiness and star-formation activity.

5.1.1 IRX

The IRX can be calculated from the UV attenuation A_{1530} (e.g., Meurer et al. 1999). Buat et al. (2012) have found that high-z galaxies ($z \simeq 0.95 - 2.2$) follow the relation given in Overzier et al. (2011):

$$\log_{10} IRX = \log_{10}(10^{0.4A_{1530}} - 1) - \log_{10}(0.595), \tag{20}$$

as shown in their figure 14 [4]. We convert the $E(B-V)_\star$ of our subsamples into IRX and compare them with two average relations at $z \sim 2$ (Heinis et al. 2014; Bouwens et al. 2016)[5] as shown in figure 3. At low-stellar masses with $M_\star \lesssim 3$–$5 \times 10^9\,\mathrm{M}_\odot$, the average relation has not been defined well but it is probably located between the two.

Figure 3 (a) shows the field-average values of our subsamples with the assumption of a SMC-like attenuation curve (red symbols), which are calculated from the results for the two fields shown in panel (b) (orange and green symbols). The field-average results lie on an extrapolation of the relation for UV-selected galaxies at $z \sim 1.5$ in Heinis et al. (2014). Considering the relatively large uncertainties remaining in the two average relations, we conclude that our LAEs are not outliers but have normal dustinesses. This result is consistent with those obtained for all LAEs using Spitzer/MIPS 24μm data by Kusakabe et al. (2015) and from SED fitting by Kusakabe et al. (2018).Note,

[4] This formula is derived with the total IR luminosity (3–1000μm, TIR) for local galaxies. According to the result in Buat et al. (2012), we do not convert $IRXs$ to those with IR luminosity (8–1000μm) in the relation, unlike our previous work (Kusakabe et al. 2018).

[5] Bouwens et al. (2016) have obtained a 'consensus relation' from previous analyses for galaxies at $z \sim 2$–3 (Reddy et al. 2010; Whitaker et al. 2014; Álvarez-Márquez et al. 2016), which is consistent with their result using ALMA data. On the other hand, Heinis et al. (2014) derives a relation for UV-selected galaxies at $z \sim 1.5$ giving higher $IRXs$ than the 'consensus relation' at low-stellar masses regime, however it is consistent wit a new result of star forming galaxies at $2 < z < 3$ with ALMA data McLure et al. (2017).

Table 4. Clustering Measurements for the eight subsamples.

subsamples	A_ω	$A_{\omega,\,\rm corr}$	$r_{0,\,\rm corr}$ ($\rm h_{100}^{-1}Mpc$)	$b_{\rm g,\,eff}$	$M_{\rm h}$ ($\times 10^{10}$ $\rm M_\odot$)	reduced χ^2
	(1)	(2)	(3)	(4)	(5)	(6)
bright UV	1.03 ± 0.82	1.28 ± 1.05	$1.20^{+0.48}_{-0.74}$	$0.66^{+0.23}_{-0.38}$	$< 0.2^{(7)}$	1.46
faint UV	3.65 ± 1.25	4.51 ± 1.84	$2.42^{+0.51}_{-0.61}$	$1.23^{+0.23}_{-0.29}$	$4.4^{+8.8}_{-4.0}$	1.34
blue β	1.12 ± 0.74	1.38 ± 0.97	$1.25^{+0.43}_{-0.61}$	$0.68^{+0.21}_{-0.31}$	$< 0.2^{(7)}$	0.91
red β	4.29 ± 1.37	5.29 ± 2.06	$2.65^{+0.53}_{-0.63}$	$1.34^{+0.24}_{-0.29}$	$7.6^{+12.4}_{-6.5}$	0.52
bright Lyα	3.96 ± 1.29	4.89 ± 1.93	$2.53^{+0.51}_{-0.62}$	$1.29^{+0.23}_{-0.29}$	$5.9^{+10.4}_{-5.1}$	0.85
faint Lyα	5.39 ± 1.27	6.65 ± 2.16	$3.00^{+0.51}_{-0.59}$	$1.50^{+0.23}_{-0.27}$	$15.2^{+16.8}_{-10.8}$	1.81
large EW	3.27 ± 1.27	4.04 ± 1.81	$2.28^{+0.52}_{-0.64}$	$1.17^{+0.24}_{-0.30}$	$3.0^{+7.4}_{-2.8}$	0.64
small EW	4.90 ± 1.26	6.05 ± 2.05	$2.85^{+0.50}_{-0.59}$	$1.43^{+0.23}_{-0.27}$	$11.5^{+14.3}_{-8.7}$	1.75

Note. (1) Correlation amplitude without contamination correction; (2) contamination-corrected correlation amplitude used to derive (3)–(5); (3) correlation length; (4) effective bias factor, (5) dark matter halo mass; and (6) reduced χ^2 value. (7) $1\,\sigma$ upper limit of $M_{\rm h}$ (see appendix 5). The field-average best fit values are calculated from equation 13 in Kusakabe et al. (2018).

however, that if we assume a Calzetti-like attenuation curve instead, our LAEs are expected to be dustier galaxies than ordinary galaxies at the same stellar masses as shown by pink symbols in panel (c).

5.1.2 Star Formation Mode

At $z \sim 2$, the SFMS has been determined well down to $M_\star \sim 10^{10}\,\rm M_\odot$ (e.g., Rodighiero et al. 2011; Whitaker et al. 2014; Tomczak et al. 2016; Shivaei et al. 2017) since SFRs can be accurately measured from either rest-frame UV and FIR (or MIR) fluxes or Hα and Hβ emission-line fluxes.Although these results are not consistent with each other as shown in figure 4, the true SFMS probably lies somewhere between the Tomczak et al. (2016) and Shivaei et al. (2017)'s results. Below $M_\star \sim 10^{10}\,\rm M_\odot$, Santini et al. (2017) suggest that the SFMS continues down to $M_\star \sim 10^8\,\rm M_\odot$ without changing its power-law slope. We compare the results for our LAEs with the extrapolated SFMS shown in Tomczak et al. (2016) and Shivaei et al. (2017) below.

Figure 4 (a) shows the field-average values for the ten subsamples with a SMC-like attenuation curve (red symbols) while panel (b) the separate results for the two fields (orange and green symbols). All the field-average data points lie on the extrapolation of the SFMS in Tomczak et al. (2016), being only slightly above the Shivaei et al. relation.This result is also consistent with those obtained for all LAEs by Kusakabe et al. (2015) and Kusakabe et al. (2018). We conclude that the majority of our LAEs are in a moderate star formation mode even after divided into two subsamples by various properties.

We also compare our results to previous studies on individual LAEs and Hα emitters (HAEs) at similar redshifts. For this comparison, we use the results based on a Calzetti attenuation curve (figure 4 [c]) following these previous studies. We find in figure 4 (d) that our ten subsamples (pink symbols) are distributed in the middle of individual LAEs with $M_\star$ and SFR measurements (Hagen et al. 2016; Shimakawa et al. 2017; Hashimoto et al. 2017; Taniguchi et al. 2015, $z \sim 2$–3)[6]. In figure 4 (e), our LAEs are found to be located at the lower-mass regime of NB-detected HAEs (Tadaki et al. 2013; Matthee et al. 2016). While the HAEs in Tadaki et al. (2013) (open cyan hexagons) [7] lie on the SFMS, those in Matthee et al. (2016) (filled blue hexagons) [8] are widely scattered along the horizontal direction around the SFMS because they are essentially Hα luminosity selected. Some HAEs in Matthee et al. (2016) have similarly low stellar masses to our LAEs but with higher $SFRs$ due to this selection bias.

5.2 Halo and total Lyα luminosities

Figure 5 plots $L(\rm Ly\alpha)_H$ and $L(\rm Ly\alpha)_{tot}$ against SFR, $E(B-V)_\star$, $M_\star$, and $M_{\rm h}$. The ten subsamples have similar $L(\rm Ly\alpha)_H$ of $\sim 2\times10^{42}\,\rm erg\,s^{-1}$, and similar $L(\rm Ly\alpha)_{tot}$ of $\sim 2\times10^{42}$–$4\times10^{42}\,\rm erg\,s^{-1}$ within a factor of 1.5 (see also table 5 in appendix). Specifically, $L(\rm Ly\alpha)_H$ and $L(\rm Ly\alpha)_{tot}$ remain almost unchanged when $M_\star$ increases by factor 2–5.

The nearly constant (or even slightly decreasing) $L(\rm Ly\alpha)_H$ against $M_\star$ is a result of two competing trends. One is that $L(\rm Ly\alpha)_C$ is constant or decreases with $M_\star$ as expected from the $L(\rm Ly\alpha)_{ps}$ vs. $M_{\rm UV}$ plot (figure1 [g]), and the other is that $L(\rm Ly\alpha)_H/L(\rm Ly\alpha)_C$ decreases with $L(\rm Ly\alpha)_C$ as found from equation (10). Let us take the $L(\rm Ly\alpha)$–divided and K–divided

[6] In Hagen et al. (2016) and Shimakawa et al. (2017), $M_\star$ are derived from SED fitting with the Calzetti curve and SFR from the IRX–β relation in Meurer et al. (1999). On the other hand, Taniguchi et al. (2015) and Hashimoto et al. (2017) derive both quantities from SED fitting with the Calzetti curve.

[7] They derive $M_\star$ from SED fitting with the Calzetti curve (for more details Tadaki et al. 2017), while deriving SFRs from Hα luminosities except for MIPS 24μm detected objects whose SFRs are estimated from UV and MIPS photometry (see also Tadaki et al. 2015). Note that SFRs calculated from PACS data are not plotted here.

[8] When analyzing individual galaxies, they assume the Calzetti curve to derive $M_\star$ and assume $E(B-V)_\star = E(B-V)_g$ to correct Hα luminosities (and hence $SFRs$) for dust extinction(see SED fitting paper of HiZELS for more details Sobral et al. 2014). However, when stacking, they use $A(\rm H\alpha) = 1$ mag to correct Hα luminosities for all subsamples.

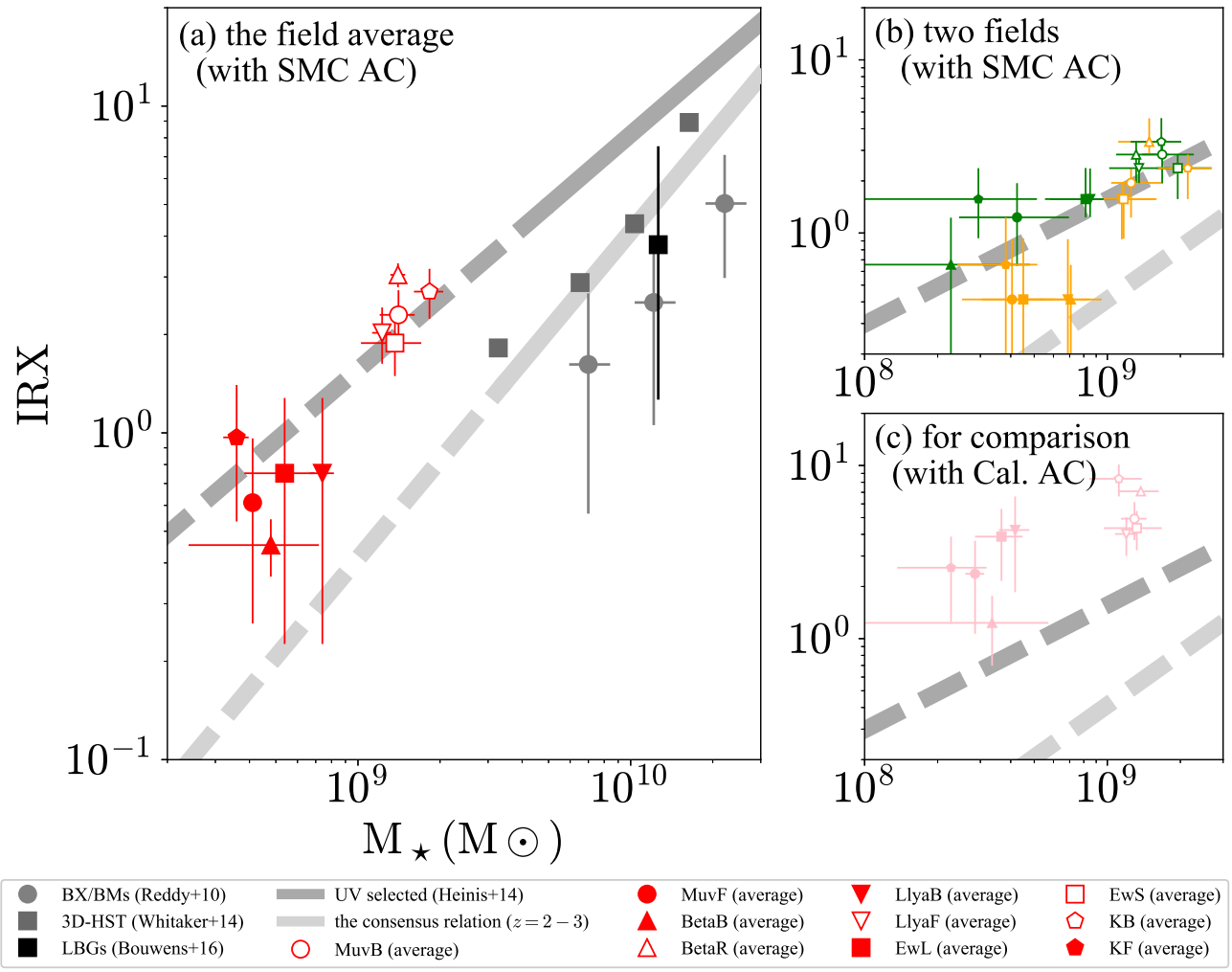

Fig. 3. IRX vs.$M_\star$. (a) Field average values of our ten subsamples with an assumption of a SMC-like attenuation curve (red symbols), (b) results before averaging (green and orange symbols), and (c) field average values with an assumption of a Calzetti curve (pink symbols), plotted with some literature results. In panels (a) and (c), different subsamples are shown by different symbols: open (filled) circles for bright (faint) $M_{\rm UV}$, open (filled) triangles for red (blue) β, open (filled) inverted triangles for faint (bright) $L({\rm Ly}\alpha)_{ps}$, open (filled) squares for small (large) $EW_{0,ps}({\rm Ly}\alpha)$, and open (filled) pentagons for bright (faint) $m_{\rm K}$. Dark gray squares, dark gray circles, a black square, a dark gray solid line and a light gray solid line represent, respectively, 3D-HST galaxies at $z\sim2$ in Whitaker et al. (2014), UV selected galaxies at $z\sim2$ in Reddy et al. (2010), LBGs at $z\sim2-3$ in Bouwens et al. (2016), UV-selected galaxies at $z\sim1.5$ in Heinis et al. (2014) and the consensus relation of them determined by Bouwens et al. (2016). Dark and light gray dashed lines indicate extrapolations of gray solid lines. In panel (b), orange and green symbols indicate, respectively, the SXDS and COSMOS subsamples with a SMC-like attenuation curve (with SMC AC). All data are rescaled to a Salpeter IMF according to footnote 1. (Color online)

subsamples as two examples. For the former subsamples, the $L({\rm Ly}\alpha)_C$ of the massive subsample is factor 2.5 *lower* than that of the less massive one, but the difference is reduced to factor 1.5 in $L({\rm Ly}\alpha)_H$ because objects with lower $L({\rm Ly}\alpha)_C$ have higher $L({\rm Ly}\alpha)_H/L({\rm Ly}\alpha)_C$. For the latter, the two subsamples have almost the same $L({\rm Ly}\alpha)_C$ and hence almost the same $L({\rm Ly}\alpha)_H$. The slightly decreasing trend of $L({\rm Ly}\alpha)_{tot}$ with mass is due to the fact that $L({\rm Ly}\alpha)_{tot}/L({\rm Ly}\alpha)_C$ decreases with $L({\rm Ly}\alpha)_C$ more mildly than $L({\rm Ly}\alpha)_H/L({\rm Ly}\alpha)_C$ does.

Figure 5 shows that $L({\rm Ly}\alpha)_H$ and $L({\rm Ly}\alpha)_{tot}$ are also nearly independent of SFR, $E(B-V)_\star$, and $M_{\rm h}$, although the uncertainties in $M_{\rm h}$ are relatively large. The fact that differently defined subsamples follow a common trend in each panel indicates that the nearly constant $L({\rm Ly}\alpha)_H$ and $L({\rm Ly}\alpha)_{tot}$ against

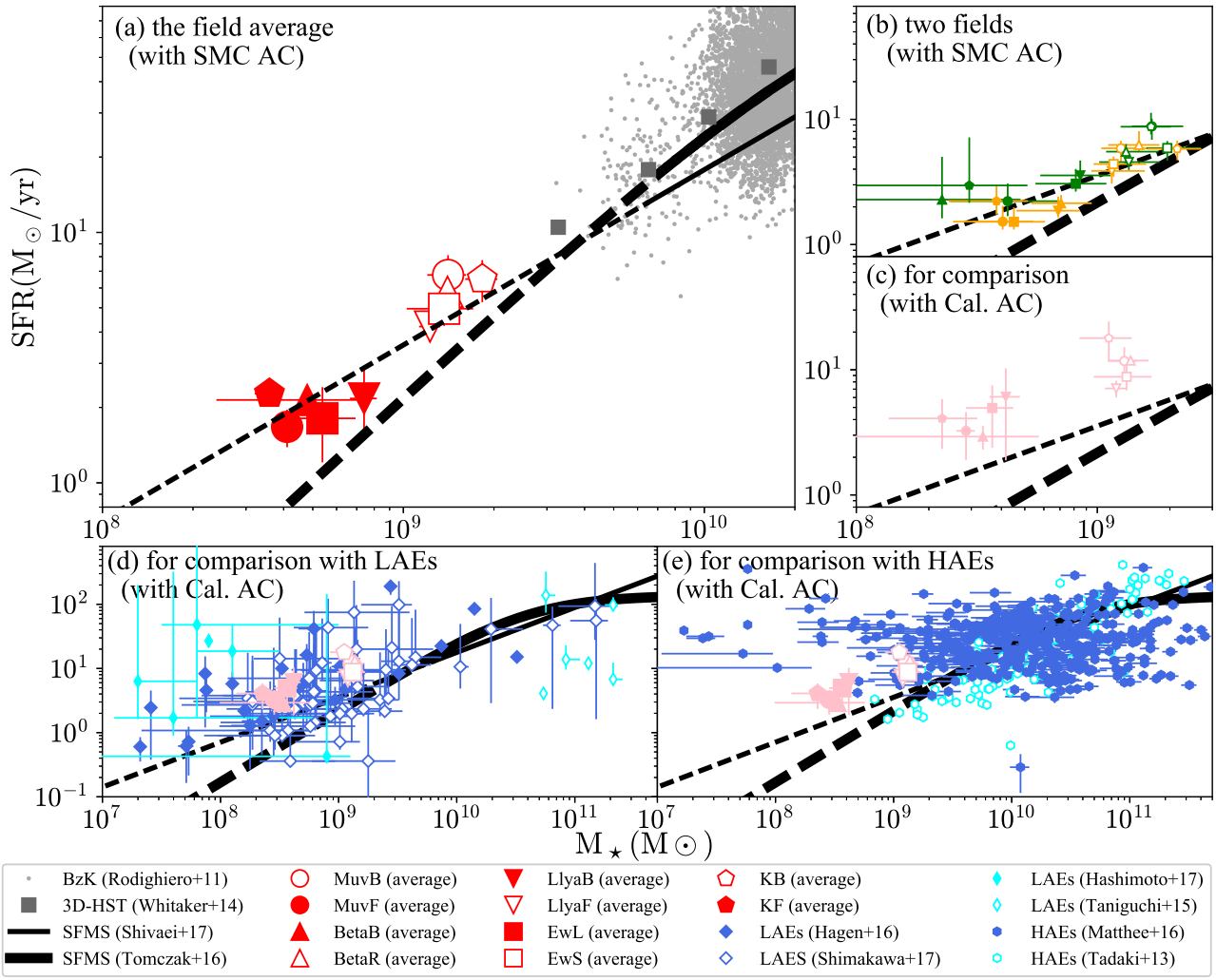

Fig. 4. SFR vs. $M_\star$. (a) Field average values of our ten subsamples with a SMC-like attenuation curve (red symbols), (b) results before averaging (green and orange symbols), and (c)-(e) field average values with a Calzetti curve (pink symbols), plotted with some literature results. In panels (a) and (c)–(e), different subsamples are shown by different symbols: open (filled) circles for bright (faint) $M_{\rm UV}$, open (filled) triangles for red (blue) β, open (filled) inverted triangles for faint (bright) $L({\rm Ly}\alpha)_{ps}$, open (filled) squares for small (large) $EW_{0,ps}({\rm Ly}\alpha)$, and open (filled) pentagons for bright (faint) $m_{\rm K}$. In panel (b), orange and green symbols indicate, respectively, the SXDS and COSMOS subsamples with a SMC-like attenuation curve (with SMC AC). In panels (c)–(e), pink symbols show the average values of the subsamples over the two fields with a Calzetti attenuation curve (with Cal. AC). Dark gray squares, light gray dots, thick black solid lines, and thin black solid lines represent, respectively, 3D-HST galaxies at $z\sim2$ in Whitaker et al. (2014), BzK galaxies at $z\sim2$ in Rodighiero et al. (2011), the SFMS at $z\sim2$ in Tomczak et al. (2016), and the SFMS at $z\sim2$ in Shivaei et al. (2017). Thick and thin black dashed lines indicate extrapolations of the black solid lines. In panel (d), filled blue diamonds, open blue diamonds, filled cyan thin diamonds, and open cyan thin diamonds indicate LAEs at $z\sim2$–3 in Hagen et al. (2016); Shimakawa et al. (2017); Hashimoto et al. (2017) and Taniguchi et al. (2015), respectively. In panel (e), filled blue hexagons and open cyan hexagons show HAEs at $z\sim2$–3 in Matthee et al. (2016) and Tadaki et al. (2013). All data are rescaled to a Salpeter IMF according to footnote 1. (Color online)

$M_\star$ and the other three parameters are real; it is unlikely that grouping the LAEs into two by the five quantities has erased strong mass dependence which otherwise would be visible. We discuss the physical origins of diffuse Lyα halos from these results in section 6.1.

5.3 Escape fraction of Lyα photons

Following previous studies, we define the escape fraction of Lyα photons, $f_{\rm esc}({\rm Ly}\alpha)$, as the ratio of observed Lyα luminosity, $L({\rm Ly}\alpha)_{obs}$, to intrinsic Lyα luminosity, $L({\rm Ly}\alpha)_{int}$, produced in the galaxy due to star formation (e.g., Atek et al. 2008;

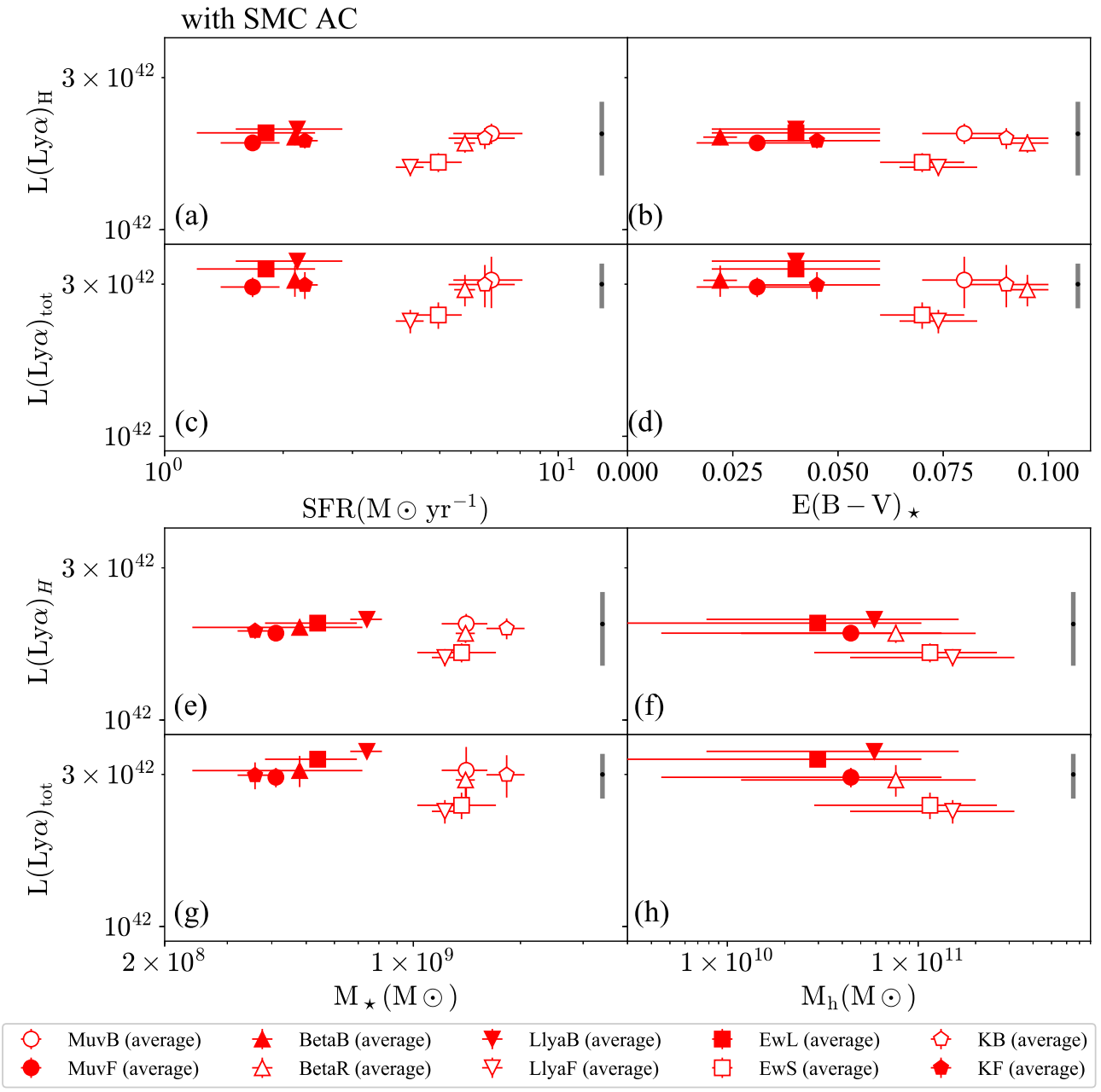

Fig. 5. $L(\mathrm{Ly}\alpha)_H$ and $L(\mathrm{Ly}\alpha)_{tot}$ as a functions of stellar parameters and dark matter halo mass for a SMC curve: (a) $L(\mathrm{Ly}\alpha)_H$ vs. SFR, (b) $L(\mathrm{Ly}\alpha)_H$ vs. $E(B-V)_\star$, (c) $L(\mathrm{Ly}\alpha)_{tot}$ vs. SFR, (d) $L(\mathrm{Ly}\alpha)_{tot}$ vs. $E(B-V)_\star$, (e) $L(\mathrm{Ly}\alpha)_H$ vs. $M_\star$, (f) $L(\mathrm{Ly}\alpha)_H$ vs. M_h, (g) $L(\mathrm{Ly}\alpha)_{tot}$ vs. $M_\star$, and (h) $L(\mathrm{Ly}\alpha)_{tot}$ vs. M_h. All values are field average values. Different symbols indicate different subsamples: open (filled) circles for bright (faint) M_UV, open (filled) triangles for red (blue) β, open (filled) inverted triangles for faint (bright) $L(\mathrm{Ly}\alpha)_{ps}$, open (filled) squares for small (large) $EW_{0,ps}(\mathrm{Ly}\alpha)$, and open (filled) pentagons for bright (faint) m_K. The typical 1σ uncertainties in the individual data in Momose et al. (2016) are propagated to uncertainties in $L(\mathrm{Ly}\alpha)_H$ and $L(\mathrm{Ly}\alpha)_{tot}$ of $\sim 22\%$ and $\sim 16\%$, respectively. Gray error bars of black dots in panels (a)–(d) and (e)–(f) show those uncertainties at $L(\mathrm{Ly}\alpha)_H = 2\times10^{42}\,\mathrm{erg\,s^{-1}}$ and $L(\mathrm{Ly}\alpha)_{tot} = 3\times10^{42}\,\mathrm{erg\,s^{-1}}$, respectively. The vertical error bars of the red symbols are derived from the fitting errors in $L(\mathrm{Ly}\alpha)_{ps}$. M_h are not calculated for the m_K-divided subsamples. The M_h values for the bright M_UV and blue β subsamples are not shown because they are not constrained well owing to too weak clustering signals. (Color online)

Kornei et al. 2010):

$$f_\mathrm{esc}(\mathrm{Ly}\alpha) = \frac{L(\mathrm{Ly}\alpha)_{obs}}{L(\mathrm{Ly}\alpha)_{int}} = \frac{SFR_{Ly\alpha}}{SFR_{tot}}, \quad (21)$$

where SFR_{tot} is the total (i.e., dust-corrected) star formation rate and $SFR_{Ly\alpha}$ is the star formation rate converted from $L(\mathrm{Ly}\alpha)_{obs}$ as below:

$$SFR_{Ly\alpha}\,(\mathrm{M_\odot\,yr^{-1}}) = 9.1\times10^{-43}\,L(\mathrm{Ly}\alpha)_{obs}\,(\mathrm{erg\,s^{-1}}) \quad (22)$$

(Brocklehurst 1971; Kennicutt 1998). In this work, we derive $f_{\rm esc}({\rm Ly}\alpha)$ from $L({\rm Ly}\alpha)_{tot}$ (total Lyα escape fraction, $f_{\rm esc}({\rm Ly}\alpha)_{tot}$; see table 3) unlike previous studies which have ignored the contribution from the LAH (e.g., Blanc et al. 2011; Kusakabe et al. 2015; Oteo et al. 2015). For SFR_{tot} we use the one obtained from the SED fitting. This definition of $f_{\rm esc}({\rm Ly}\alpha)$ thus assumes that all Lyα photons including those of the LAH are produced from star formation in the central galaxy. We discuss the possibility of the existence of additional Lyα sources later.

Figure 6 shows $f_{\rm esc}({\rm Ly}\alpha)_{tot}$ as a functions of $M_\star$, SFR, and $E(B-V)$ for the ten subsamples. All values are field-average values. For a thorough discussion, results with a Calzetti curve are also shown (panels [b], [d], and [f]) as well as those with a SMC curve (the other panels). Two interesting features are seen in this figure. First, $f_{\rm esc}({\rm Ly}\alpha)_{tot}$ anti-correlates with $M_\star$, SFR, and $E(B-V)$ regardless of the assumed curve.

Similar anti-correlations have been found for HAEsby Matthee et al. (2016) who have measured total Lyα luminosities on a $6''$ diameter aperture, corresponding to 24 kpc in radius (blue crosses in the Calzetti-curve panels; see also footnote 8). Any galaxy population may have such anti-correlations. Indeed, an anti-correlation between $f_{\rm esc}({\rm Ly}\alpha)$ and $E(B-V)$ is found for star forming galaxies at $\sim$0–3 (e.g., Hayes et al. 2011; Blanc et al. 2011; Atek et al. 2014; Hayes et al. 2014). Although Lyα halos are not included in their calculations, these results imply an anti-correlation between $f_{\rm esc}({\rm Ly}\alpha)_{tot}$ and $E(B-V)$ since $L({\rm Ly}\alpha)_{tot}$ increases with $L({\rm Ly}\alpha)_C$ as seen in figure 2(f).

Second, our LAEs have very high $f_{\rm esc}({\rm Ly}\alpha)_{tot}$ values. For a SMC-like curve, they are higher than $\sim 30\%$, with some exceeding 100%. Using a Calzetti curve makes $f_{\rm esc}({\rm Ly}\alpha)_{tot}$ lower but still in a range of $\sim$ 10–100%. More importantly, the $f_{\rm esc}({\rm Ly}\alpha)_{tot}$ of our LAEs is higher than that of HAEs with similar $M_\star$, SFR, and $E(B-V)_\star$. We discuss mechanisms by which LAEs can achieve such high escape fractions in section 6.2.

6 Discussion

6.1 The origin of LAHs

As described in section 1, theoretical studies have suggested three physical origins of LAHs around high–z star-forming galaxies: (a) cold streams (gravitational cooling), (b) star formation in satellite galaxies, and (c) resonant scattering of Lyα photons in the CGM which have escaped from the central galaxy. In origins (a) and (b), the Lyα photons of LAHs are produced in situ, while in origin (c) they come from central galaxies. The difference between (a) and (b) is how to produce Lyα photons.A flow chart and an illustration of these origins are shown in figure 6 in Mas-Ribas et al. (2017) and figure 15 in Momose et al. (2016), respectively. However, observations have not yet identified the dominant origin(s) as explained below.

There are two observational studies on the origin of LAHs around star-forming galaxies. Leclercq et al. (2017) use 166 LAEs at $z\sim$ 3–5 detected with the MUSE, while Momose et al. (2016) are based on a stacking analysis of ~ 3600 $z\simeq 2.2$ LAEs from a narrow-band survey, the same parent sample as we use in this study. Leclercq et al. (2017) have argued that a significant contribution from (b) star formation in satellite galaxies is somewhat unlikely since the UV component of MUSE-LAEs is compact and not spatially offset from the center of their LAH. However, they have not given a firm conclusion on the contributions from the remaining two origins. This is because while they have found a scaling relation of $L({\rm Ly}\alpha)_H \propto L_{\rm UV}^{0.45}$ which is not dissimilar to the scaling predicted from hydrodynamical simulations of cold streams by Rosdahl & Blaizot (2012), resonant scattering also prefers such a positive scaling relation if $f_{\rm esc}({\rm Ly}\alpha)_{tot}$ is constant. Moreover, they have also found that $\sim 80\%$ of their sample have a not-so-large total EW of Lyα emission, $EW_{0,tot}({\rm Ly}\alpha) \lesssim 200$Å, not exceeding the maximum dust-free $EW_0({\rm Ly}\alpha)$ of population II star formation, $\sim$ 50–240Å, with a solar metallicity and a Salpeter IMF (e.g., Charlot & Fall 1993; Malhotra & Rhoads 2002). If $EW_0({\rm Ly}\alpha)$ is larger than $\sim$200Å, Lyα radiation from cold streams is responsible for LAHs.

Momose et al. (2016) have also found relatively low $EW_{0,tot}({\rm Ly}\alpha)$ and marginally ruled out the cold-stream origin based on a similar discussion to Leclercq et al. (2017)'s. In these two observational studies, $EW_{0,tot}({\rm Ly}\alpha)$ are calculated by dividing the total Lyα luminosity by the UV luminosity of the *central* part. Therefore, the relatively low $EW_{0,tot}({\rm Ly}\alpha)$ values do not necessarily mean that the net EW_0 of LAHs are also low; they would even be extremely high if LAHs do not have UV emission. Thus, the cold-stream scenario cannot be ruled out from the low $EW_{0,tot}({\rm Ly}\alpha)$ values alone. The discussion using the $L({\rm Ly}\alpha)_H$–$L_{\rm UV}$ relation assumes $L_{\rm UV} \propto M_{\rm h}^{0.5}$ because the simulations have calculated $L({\rm Ly}\alpha)_H$ against $M_{\rm h}$. Since $L_{\rm UV}$ may not be a perfect tracer of $M_{\rm h}$, it is more desirable to use directly the $L({\rm Ly}\alpha)_H$-$M_{\rm h}$ relation, or the $L({\rm Ly}\alpha)_H$–$M_\star$ relation as a better substitute. In addition, comparing the normalization of the relation as well as its power-law slope can better constrain this scenario. With regard to (b) satellite star formation, independent observations are desirable to strengthen the conclusion by Leclercq et al. (2017) since Momose et al. (2016) have not been able to rule out this origin. Finally, if resonant scattering is the dominant origin, LAH luminosities have to be explained by the properties of the main body of galaxies such as SFR and $E(B-V)$.

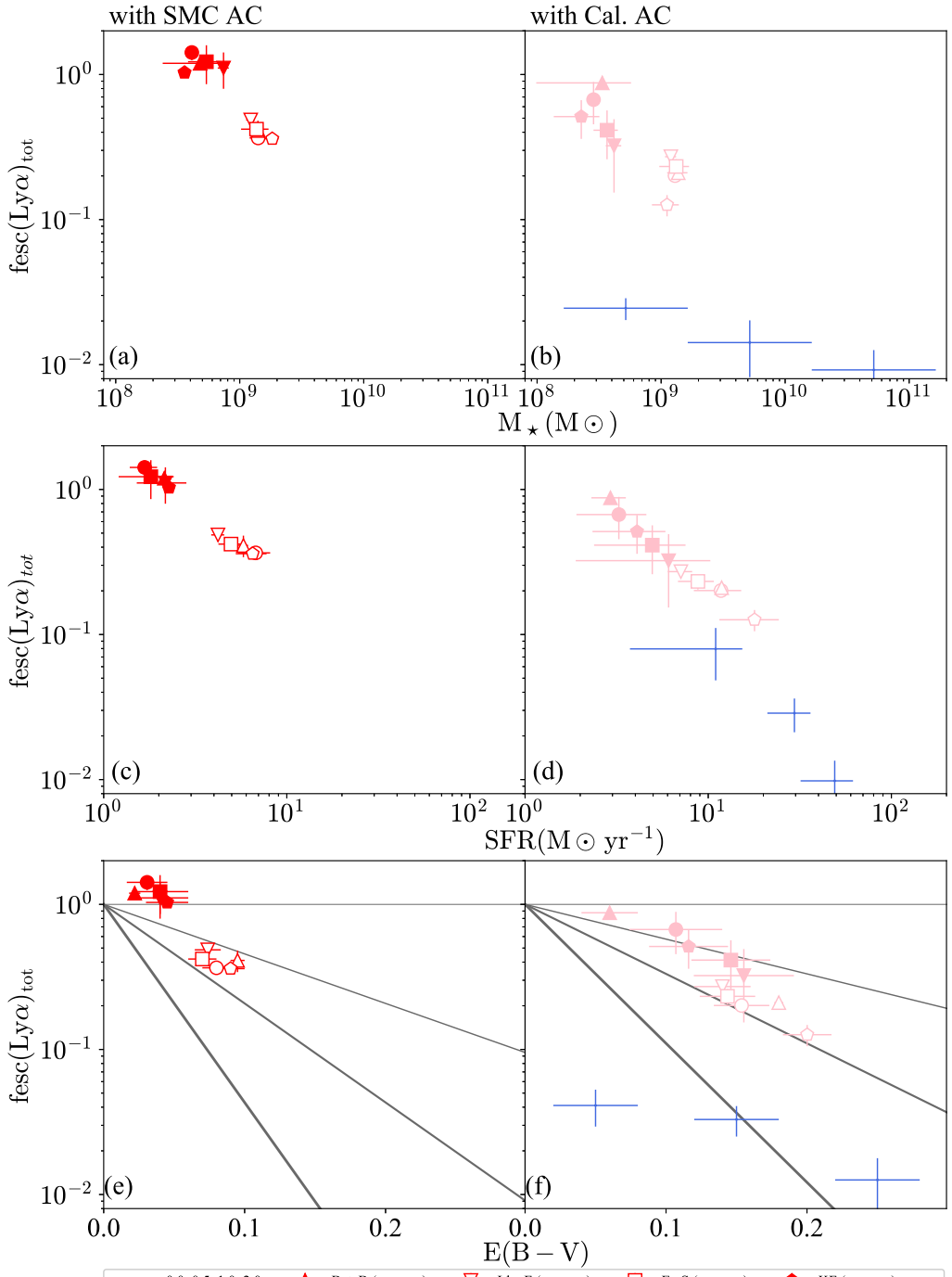

Fig. 6. $fesc(\mathrm{Ly}\alpha)_{tot}$ as a functions of $M_\star$ (panels [a] and [b]), SFR ([c] and [d]), and $E(B-V)$ ([e] and [f]) for the two attenuation curves. All values are field average values. Different symbols indicate different subsamples: open (filled) circles for bright (faint) M_{UV}, open (filled) triangles for red (blue) β, open (filled) inverted triangles for faint (bright) $L(\mathrm{Ly}\alpha)_{ps}$, open (filled) squares for small (large) $EW_{0,ps}(\mathrm{Ly}\alpha)$, and open (filled) pentagons for bright (faint) m_{K}. Blue crosses indicate HAEs in Matthee et al. (2016), whose Lyα luminosities are derived from $6''$ aperture photometry. Dark gray solid lines show models for four different q values, $q = 0.0, 0.5, 1.0$, and 2.0 with increasing thickness. Stellar parameters are derived with the assumption of $E(B-V)_\star = E(B-V)_g$. (Color online)

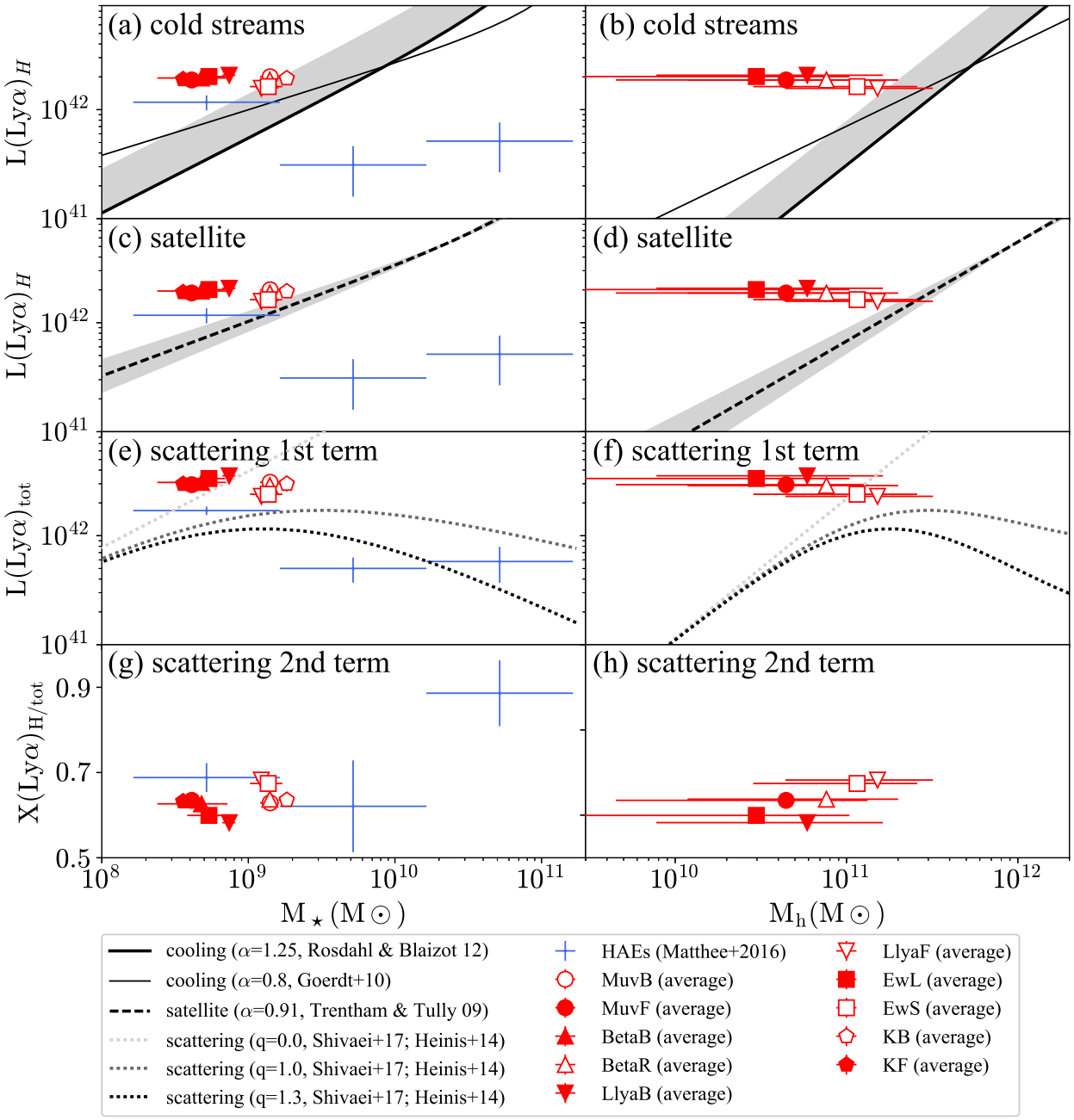

Fig. 7. Test of the three LAH scenarios against the observed $L(\mathrm{Ly}\alpha)_H$ and its mass dependence: (a) and (b) – cooling flow; (c) and (d) – satellite star formation; (e) and (h) – resonant scattering. Thick and thin solid black lines in panels (a) and (b) show the Lyα luminosity of cooling flows by theoretical models with a power law of $\alpha = 1.25$ (Rosdahl & Blaizot 2012) and $\alpha = 0.8$ (Goerdt et al. 2010), respectively. Gray shaded regions above the solid black lines roughly indicate the distribution of Rosdahl & Blaizot (2012)'s simulated galaxies above the solid line, whose $L(\mathrm{Ly}\alpha)_H$ reaches at most ~ 2.5 times higher than the line. A dashed black line in panels (c) and (d) shows the Lyα luminosity from the star formation in satellite galaxies, with a normalization to the cold stream scenario in Rosdahl & Blaizot (2012). Gray shaded regions around the dashed black lines indicate the 1σ uncertainty in the power law index in Trentham & Tully (2009). Light gray, dark gray, and black dotted lines in (e) represent the Lyα luminosity escaping from the main body out to the CGM, with an absorption efficiency relative to UV continuum of $q = 0.0, 1.0$ and 1.3. We assume that all Ly$alpha$ photons originate from star formation. Blue crosses indicate HAEs in Matthee et al. (2016), whose Lyα luminosities are derived from $3''$ and $6''$-diameter aperture photometry (see footnotes 8 and 9). Field average values of our ten subsamples are shown by symbols below: open (filled) circles for bright (faint) M_{UV}, open (filled) triangles for red (blue) β, open (filled) inverted triangles for faint (bright) $L(\mathrm{Ly}\alpha)_{ps}$, open (filled) squares for small (large) $EW_{0,ps}(\mathrm{Ly}\alpha)$, and open (filled) pentagons for bright (faint) m_{K}. Stellar parameters of our subsamples are derived with the assumption of a SMC-like attenuation curve. M_{h} are not calculated for the K-divided subsamples, and are not plotted for the bright M_{UV} and blue β subsamples because of extremely large uncertainties. All data are rescaled to a Salpeter IMF according to footnote 1. (Color online)

In section 5, we find that the $L(\mathrm{Ly}\alpha)_H$ and $L(\mathrm{Ly}\alpha)_{tot}$ of our LAEs remain unchanged with increasing stellar mass. We also obtain a constant or increasing $X(\mathrm{Ly}\alpha)_{H/tot}$ with $M_\star$ (see figure 7[g]). In the following subsections, we use these relations to discuss the three origins with figure 7. We also use the results on HAEs obtained by Matthee et al. (2016)[9] to strengthen the discussion.

6.1.1 (a) Cold streams

Theoretical studies and simulations suggest that high-z ($z \gtrsim 2$) galaxies obtain baryons through the accretion of relatively dense and cold ($\sim 10^4$ K) gas known as cold streams (e.g., Fardal et al. 2001; Kereš et al. 2005; Dekel & Birnboim 2006). The accreting gas releases the gravitational energy and emits Lyα photons, thus producing an extended Lyα halo without (extended) UV continuum emission (e.g., Haiman et al. 2000; Furlanetto et al. 2005; Dijkstra & Loeb 2009; Lake et al. 2015).

The Lyα luminosity due to cold streams is suggested to increase with the M_h of host galaxies. A scaling of $L(\mathrm{Ly}\alpha)_H \propto {M_\mathrm{h}}^{1.1}$-${M_\mathrm{h}}^{1.25}$ at $M = 10^{10}$–$10^{13}\,M_\odot$ has been predicted by (zoom-in) cosmological hydrodynamical simulations in Faucher-Giguère et al. (2010) and Rosdahl & Blaizot (2012). Dijkstra & Loeb (2009) have obtained a similar correlation to Faucher-Giguère et al. (2010)'s from an analytic model which reproduces the Lyα luminosities, Lyα line widths, and number densities of observed LABs at $M_\mathrm{h} \gtrsim 10^{11}\,M_\odot$. On the other hand, Goerdt et al. (2010) have derived a shallower power law slope ~ 0.8 for LAB-hosting massive ($M_\mathrm{h} \sim 10^{12}$–$10^{13}\,M_\odot$) halos from high-resolution cosmological hydrodynamical adaptive mesh refinement simulations.

We examine if our subsamples are consistent with these theoretical predictions by comparing the power-law slope and amplitude of the $L(\mathrm{Ly}\alpha)_H$-M_h relation. For a conservative discussion, we use Rosdahl & Blaizot (2012)'s relation which gives the steepest slope and Goerdt et al. (2010)'s relation giving the shallowest slope as shown in figure 7 (b) [10]:

$$L(\mathrm{Ly}\alpha)_H \sim 8 \times 10^{42} \left(\frac{M_\mathrm{h}}{10^{12} M_\odot}\right)^{1.25} \left(\frac{1+z}{1+3}\right)^{1.3} \quad (23)$$

$$L(\mathrm{Ly}\alpha)_H = 9.72 \times 10^{42} \left(\frac{M_\mathrm{h}}{10^{12} M_\odot}\right)^{0.8} (1+z)^{1.3}. \quad (24)$$

In panel 7(a), we convert M_h to $M_\star$ using the average relation between $M_\star$ and M_h at $z \sim 2$ in Moster et al. (2013)[11]. The constant $L(\mathrm{Ly}\alpha)_H$ with $M_\star$ and M_h seen in the LAEs is inconsistent with the increasing $L(\mathrm{Ly}\alpha)_H$ predicted by the theoretical models, although the uncertainties in our M_h estimates are large. The HAEs have also non-increasing $L(\mathrm{Ly}\alpha)_H$ over two orders of magnitude in $M_\star$, highlighting the inconsistency found for the LAEs. As for amplitude, the LAEs shown by red filled (open) symbols have $\sim$ 2–4 ($\sim$ 1–2) times higher $L(\mathrm{Ly}\alpha)_H$ than the two model predictions at the same $M_\star$ (panel [a]), and at least $\sim$ 1–10 ($\sim$ 1–10) times higher at the same M_h (panel [b]). Even when the individual distribution of Rosdahl & Blaizot (2012)'s galaxies is considered, low-$M_\star$ LAEs (red filled symbols) have more than 10σ brighter $L(\mathrm{Ly}\alpha)_H$ than the simulated galaxies with similar $M_\star$ (a gray shaded region). In other words, cold streams cannot produce as many Lyα photons in the CGM as observed.

Note that as mentioned in appendix 1, the $L(\mathrm{Ly}\alpha)_H$ values of the faint m_K and M_{UV} subsamples are possibly overestimated since they miss small $EW(\mathrm{Ly}\alpha)$ (faint $L(\mathrm{Ly}\alpha)_C$) sources due to the NB-selection bias. If we derive $L(\mathrm{Ly}\alpha)_H$ conservatively from the M_{UV}–$L(\mathrm{Ly}\alpha)_H$ relation for individual MUSE-LAEs without such a selection bias in Leclercq et al. (2017), we obtain ~ 1.5 times smaller $L(\mathrm{Ly}\alpha)_H$, which results in a slightly positive correlation between $M_\star$ and $L(\mathrm{Ly}\alpha)_H$. However, the power law index and the amplitude of the $M_\star$–$L(\mathrm{Ly}\alpha)_H$ correlation of the m_K subsamples is still shallower and higher than theoretical results at more than the 2σ and 10σ confidence levels, respectively (see more details in appendix 4).

We thus conclude that (a) cold streams are not the dominant origin of LAHs.

6.1.2 (b) Satellite star formation

Satellite galaxies emit Lyα photons through star formation. If satellite star formation significantly contributes to LAHs, they will involve an extended UV emission from the star formation (e.g., Shimizu et al. 2011; Zheng et al. 2011; Lake et al. 2015; Mas-Ribas et al. 2017). Unfortunately, this emission is expected to be too diffuse to detect even by stacking of some 10^3 objects as mentioned in Momose et al. (2016).

The Lyα luminosity from satellite star formation can be expressed as a function of the M_h of the central galaxy with simple assumptions based on observational results as explained below. In the local universe, the number of disk (i.e., star-forming) satellite galaxies is found to be described by a power law of the host halo mass of the central galaxy with a slope 0.91 ± 0.11 for galaxies with $M_\mathrm{h} \sim 10^{12}$–$10^{14}\,M_\odot$ (see figure 14 and equation 6 in Trentham & Tully 2009). Wang et al. (2014) have studied the radial profile of the satellite number density for local galax-

[9] They discuss the escape fraction using $L(\mathrm{Ly}\alpha)$ on $r = 12$ kpc ($3''$ diameter) and 24 kpc ($6''$) apertures. Although the average profile of their LAHs extends to $r = 40$ kpc, we refer to $6''$ aperture luminosity as $L(\mathrm{Ly}\alpha)_{tot}$ and to the difference in $3''$ and $6''$ aperture luminosities as $L(\mathrm{Ly}\alpha)_H$.

[10] We shift the relation shown in figure 8 in Rosdahl & Blaizot (2012) at $z = 3$ to $z = 2$ by multiplying redshift-evolution term, $(1+z)^{1.3}$, given in figure 12 and equation 21 in Goerdt et al. (2010). We also note that the relation at $z \sim 3$ predicted in Faucher-Giguère et al. (2010) has a lower amplitude than that in Rosdahl & Blaizot (2012) typically about a factor of two (see appendix E in Rosdahl & Blaizot 2012, , for more details).

[11] Kusakabe et al. (2018) have found that our LAEs are on average slightly offset from the average relation to lower M_h values. Our discussion is unchanged if we instead use M_h reduced by this offset.

ies down to $M_\star \sim 10^{10}\,M_\odot$ and found that higher-$M_\star$ central galaxies have a higher normalization of the number density (see their figure 2). The radial distribution is also found to be similar to that of the dark matter profile. At high redshift, at least for massive central galaxies ($M_\star \sim 10^{11}\,M_\odot$ at $z \sim 1.4$), the radial number density profile of satellite galaxies is not significantly different from that at $z \sim 0$ (Tal et al. 2013). These local properties are reproduced by theoretical models (e.g., Nickerson et al. 2013; Sales et al. 2014; Okamoto et al. 2010), although Okamoto et al. (2010) argue that the behavior of satellite galaxies is sensitive to detailed modeling in simulations such as star formation feedbacks. With an assumption that the Lyα luminosity from satellite galaxies is proportional to the number of satellite galaxies, $L(\mathrm{Ly}\alpha)_H$ can be estimated from the local observational results.

We focus only on the power-law slope of the relation between $L(\mathrm{Ly}\alpha)_H$ and mass and normalize the relation with $L(\mathrm{Ly}\alpha)_H = 5.5 \times 10^{42}\,\mathrm{erg\,s^{-1}}$ at $M_\mathrm{h} = 10^{12}\,M_\odot$ for the presentation purpose[12] in figure 7(d):

$$L(\mathrm{Ly}\alpha)_H = 5.5 \times 10^{42} \left(\frac{M_\mathrm{h}}{10^{12}\,M_\odot}\right)^{0.91\pm0.11}. \quad (25)$$

This relation is then converted into a relation with $M_\star$ in figure 7(c) using the $M_\star$-M_h relation at $z \sim 2$ in Moster et al. (2013). The predicted positive correlation of $L(\mathrm{Ly}\alpha)_H$ with $M_\star$ is incompatible with the constant $L(\mathrm{Ly}\alpha)_H$ of our LAEs and with the decreasing $L(\mathrm{Ly}\alpha)_H$ of the HAEs in Matthee et al. (2016). These LAEs and HAEs span two orders of magnitude in $M_\star$. A non-increasing $L(\mathrm{Ly}\alpha)_H$ over this wide mass range may be achieved if the star formation of satellites around the massive ($\gtrsim 10^{10} M_\odot$) HAEs is greatly suppressed owing to strong negative feedbacks. However, this will not be the case because they are normal star-forming galaxies without hosting an AGN. It may also be achieved if the Lyα photons from satellites of massive galaxies are heavily ($\sim$ one dex) absorbed in the CGM, but such a heavy dust pollution in the CGM is probably unlikely.

As described in the previous subsection, using Leclercq et al. (2017)'s M_UV–$L(\mathrm{Ly}\alpha)_H$ relation results in a slightly positive correlation. However, the power law index determined by the m_K subsamples is still shallower than that of the model at more than the 2σ confidence level (see appendix 4 for detalis). In addition, it remains difficult for the model to explain the results of LAEs and HAEs in a unfied manner.

From these results, we conclude that satellite star formation is unlikely to be the dominant origin.

[12]We adopt the same normalization as that of equation 23 at $M_\mathrm{h} = 10^{12}\,M_\odot$ since Lake et al. (2015) find that the contributions to LAHs from cold streams and satellite star formation are comparable in their cosmological simulations at $z \sim 3$.

6.1.3 (c) Resonant scattering of Lyα photons in the CGM which are produced in central galaxies

HI gas in the CGM can resonantly scatter Lyα photons which have escaped from the main body of the galaxy (e.g., Laursen & Sommer-Larsen 2007; Barnes & Haehnelt 2010; Zheng et al. 2011; Dijkstra & Kramer 2012; Verhamme et al. 2012). However, there is no theoretical study that predicts $L(\mathrm{Ly}\alpha)_H$ and its dependence on galaxy properties by solving the radiative transfer of Lyα photons in the CGM. In this subsection, we first describe the LAH luminosity of a galaxy assuming that all Lyα photons come from the main body. To do so, we introduce two parameters: the escape fraction out to the CGM and the scattering efficiency in the CGM. Then, we examine if resonant scattering can explain reasonably well the behavior of LAEs and HAEs shown in the previous section. Let $L(\mathrm{Ly}\alpha)_{int}$ be the total luminosity of Lyα photons produced in the main body.Some fraction of $L(\mathrm{Ly}\alpha)_{int}$ is absorbed by dust in the inter stellar medium (ISM) and the rest escapes out into the CGM. With an assumption that dust absorption in the CGM is negligibly small, the escaping luminosity is equal to $L(\mathrm{Ly}\alpha)_{tot}$ ($= L(\mathrm{Ly}\alpha)_C + L(\mathrm{Ly}\alpha)_H$), and the escape fraction into the CGM is calculated as $f_\mathrm{esc}(\mathrm{Ly}\alpha)_{tot} = L(\mathrm{Ly}\alpha)_{tot}/L(\mathrm{Ly}\alpha)_{int}$. Then, a fraction, $X(\mathrm{Ly}\alpha)_{H/tot}$, of the escaping photons are scattered in the CGM, being extended as a LAH with $L(\mathrm{Ly}\alpha)_H$. Thus, $L(\mathrm{Ly}\alpha)_H$ can be written as:

$$L(\mathrm{Ly}\alpha)_H = L(\mathrm{Ly}\alpha)_{int}\, f_\mathrm{esc}(\mathrm{Ly}\alpha)_{tot}\, X(\mathrm{Ly}\alpha)_{H/tot} \quad (26)$$

$$= L(\mathrm{Ly}\alpha)_{tot}\, X(\mathrm{Ly}\alpha)_{H/tot}. \quad (27)$$

In the following modeling, we assume that $L(\mathrm{Ly}\alpha)_{int}$ originates only from star formation, and express it as a function of $M_\star$ using the SFMS:

$$L(\mathrm{Ly}\alpha)_{int}\,(\mathrm{erg\,s^{-1}}) = SFR_\mathrm{MS}\,(\mathrm{M_\odot\,yr^{-1}})/9.1 \times 10^{-43}. \quad (28)$$

We then describe $f_\mathrm{esc}(\mathrm{Ly}\alpha)_{tot}$ as a function of $M_\star$ using the $M_\star$–IRX relation discussed in section 5.1.The dust attenuation for 1216 Å continuum, $A_{1216con}$, at a fixed $M_\star$ is calculated from $IRX(M_\star)$:

$$A_{1216con}(M_\star) = 2.5\log_{10}(0.595 IRX(M_\star) + 1.0)\left(\frac{\kappa_{1216}}{\kappa_{1500}}\right), \quad (29)$$

where κ_{1216} and κ_{1500} are the coefficients of the attenuation curve at $\lambda = 1216$ Å and 1500 Å, respectively. Introducing the relative efficiency of the attenuation of Lyα emission to the continuum at the same wavelength, $q = A_{\mathrm{Ly}\alpha}/A_{1216con}$ (e.g., Finkelstein et al. 2008), we can write $f_\mathrm{esc}(\mathrm{Ly}\alpha)_{tot}$ as:

$$f_\mathrm{esc}(\mathrm{Ly}\alpha)_{tot} = 10^{-0.4\,q\,A_{1216con}(M_\star)}, \quad (30)$$

where $q = 0$ and $q = 1$ correspond to the case without attenuation of Lyα emission and with the same attenuation as that of continuum. We thus obtain:

$$L(\mathrm{Ly}\alpha)_{tot}(M_\star) = \left(\frac{SFR_\mathrm{MS}(M_\star)}{9.1 \times 10^{-43}}\right) 10^{-0.4\,q\,A_{1216}(M_\star)}. \quad (31)$$

We use Shivaei et al. (2017)'s SFMS and Heinis et al. (2014)'s IRX-$M_\star$ relation because our LAEs are on these relations. We also assume a SMC-like attenuation curve.

Shown in figure 7(e) are three calculations with $q = 0.0$, 1.0, and 1.3 (light gray, dark gray, and black dotted lines, respectively). The constant $L(\mathrm{Ly}\alpha)_{tot}$ with increasing $M_\star$ seen in the LAEs is achieved if q increases with $M_\star$. We note that all LAEs require $q < 1$, with the less massive subsamples suggesting $q = 0$, meaning that Lyα photons escape much more efficiently than UV photons. We do not compare the HAEs with these models since they do not follow well the SFMS and the IRX-$M_\star$ relation. As we show later, the HAEs can be explained by large q values. Further discussion of $f_{\mathrm{esc}}(\mathrm{Ly}\alpha)_{tot}$ and q for our LAEs and the HAEs is given in section 6.2. We also find that this result is unchanged even ifwe instead use a Calzetti attenuation curve, Tomczak et al. (2016)'s SFMS, and/or Bouwens et al. (2016)'s IRX-$M_\star$ relation.

The term $X(\mathrm{Ly}\alpha)_{H/tot}$ can be interpreted as the efficiency of resonant scattering in the CGM. More massive galaxies may have a larger amount of HI gas in the halo and thus have a higher $X(\mathrm{Ly}\alpha)_{H/tot}$ value. Figure 7(g) shows that this picture is consistent with our LAEs and Matthee et al. (2016)'s HAEs, because these two populations appear to follow a common, positive (although very shallow) correlation between $X(\mathrm{Ly}\alpha)_{H/tot}$ and $M_\star$.This picture is also consistent with the $X(\mathrm{Ly}\alpha)_{H/tot}$ – M_{h} plot for our LAEs (figure 7[h])within the large uncertainties in M_{h}.In this case, the LAHs of our LAEs ($\lesssim 40$ kpc in radius) are caused by HI gas roughly within the virial radius of hosting dark matter halos, $\sim$ 20–50 kpc, whose mass is estimated to be in the range $M_{\mathrm{h}} \sim 10^{10}$–$10^{11}\ M_\odot$. This relative extent of LAHs is close to those inferred for the LAHs of MUSE-LAEs by Leclercq et al. (2017), typically 60–90% of the virial radius, where they predict M_{h} from observed UV luminosities using the semi-analytic model of Garel et al. (2015).

Thus, in the resonant scattering scenario, the constant (or decreasing) $L(\mathrm{Ly}\alpha)_H$ observed is achieved by a combination of increasing $L(\mathrm{Ly}\alpha)_{int}$, decreasing $f_{\mathrm{esc}}(\mathrm{Ly}\alpha)_{tot}$, and (slightly) increasing $X(\mathrm{Ly}\alpha)_{H/tot}$ with mass, and all three trends are explained reasonably well. We conclude that (c) resonant scattering is the dominant origin of the LAHs.

6.1.4 Summary of the three comparisons

It is found that resonant scattering most naturally explains the $L(\mathrm{Ly}\alpha)_H$ and its dependence on galaxy properties seen in our LAEs and Matthee et al. (2016)'s HAEs.We, however, note that hydrodynamic cosmological simulations in Lake et al. (2015) show that scattered Lyα in the CGM can reach only out to ~ 15 kpc, suggesting that cold streams or satellite star formation are also needed, although they slightly overestimate the observed radial Lyα profile at 15 kpc (by a factor of 2). On the other hand, Xue et al. (2017) have found for LAEs at $z \sim 4$ that the radial profile of LAHs is very close toa predicted profile by Dijkstra & Kramer (2012) who have only considered resonant scattering.Theoretical models discussing the contribution of scattering to $f_{\mathrm{esc}}(\mathrm{Ly}\alpha)_{tot}$ and $X(\mathrm{Ly}\alpha)_{H/tot}$ as a function of $M_\star$ and M_{h} are needed for a more detailed comparison. Deep, spatially resolved observations of Hα emission with James Webb Space Telescope (JWST) would provide us with important clues to the origin of LAHs. Mas-Ribas et al. (2017) suggest that the spatial extents of Lyα, UV, and Hα emission differ among different origins.

6.2 The origin high Lyα escape fractions

By including $L(\mathrm{Ly}\alpha)_H$ in the total Lyα luminosity, we obtain very high $f_{\mathrm{esc}}(\mathrm{Ly}\alpha)_{tot}$ values for our LAEs as shown in section 5.2. These values are systematically higher than those obtained for LAEs in previous studies which have not considered $L(\mathrm{Ly}\alpha)_H$ (e.g., Song et al. 2014; Hayes et al. 2011). They are also about one order of magnitude higher than those of HAEs with the same $M_\star$ and $E(B-V)$ (figure 6), suggesting a large scatter in $f_{\mathrm{esc}}(\mathrm{Ly}\alpha)_{tot}$ among galaxies.

It is helpful to discuss $f_{\mathrm{esc}}(\mathrm{Ly}\alpha)$ using $E(B-V)$, since additional mechanisms are needed to make $f_{\mathrm{esc}}(\mathrm{Ly}\alpha)$ higher or lower than that expected from $E(B-V)$. The attenuation of Lyα emission relative to that of continuum emission is evaluated by the q-parameter [13] (e.g., Finkelstein et al. 2008, 2009), as discussed in section 6.1.3. Figure 8 shows q as a function of $E(B-V)$ for our LAEs and Matthee et al. (2016)'s HAEs, which are divided into subsamples in accordance with $E(B-V)$. Regardless of the attenuation curve, the LAEs have small q less than unity, which increases with $E(B-V)$. Remarkably, about a half of the subsamples, shown by red filled symbols, have $q < 0$, meaning that the observed Lyα luminosity exceeds the one calculated from the SFR. On the other hand, the HAEs have larger q (> 1) decreasing with $E(B-V)$. The difference in q between these two galaxy populations becomes larger at smaller $E(B-V)$. Note that if we calculate q of our LAEs from $L(\mathrm{Ly}\alpha)_{ps}$ instead of including $L(\mathrm{Ly}\alpha)_H$, we obtain higher values, $q \sim 1$, being closer to the values found in previous studies (e.g., Hayes et al. 2010; Nakajima et al. 2012).

Below, we discuss how LAEs can have low q and hence high

[13] The q-parameter can be rewritten as:$q = \frac{-\log(f_{\mathrm{esc}}(\mathrm{Ly}\alpha))}{0.4E(B-V)\kappa_{1216}} = \frac{\kappa}{k\kappa_{1216}} - \frac{\log C}{0.4E(B-V)\kappa_{1216}}$, where κ and C are two parameters of a commonly used fitting formula of $f_{\mathrm{esc}}(\mathrm{Ly}\alpha) = C10^{-0.4E(B-V)\kappa}$ (e.g., Hayes et al. 2011). The two parameters are difficult to interpret physically, especially for a case with $C < 1$. Hayes et al. (2011) and Atek et al. (2014) do not include $L(\mathrm{Ly}\alpha)_H$ to calculate the $f_{\mathrm{esc}}(\mathrm{Ly}\alpha)$ and obtain $C = 0.445$ with $\kappa = 13.6$ and $C = 0.22$ with $\kappa = 6.67$, respectively. Although Matthee et al. (2016) include $L(\mathrm{Ly}\alpha)_H$ to calculate $f_{\mathrm{esc}}(\mathrm{Ly}\alpha)_{tot}$, their C is less than 1 ($C = 0.08^{+0.02}_{-0.01}$ with $\kappa = 7.64^{+1.38}_{-1.36}$), which is slightly larger than the value derived without $L(\mathrm{Ly}\alpha)_H$ ($C = 0.03^{+0.01}_{-0.01}$ with $\kappa = 10.71^{+0.89}_{-1.01}$). Note that Atek et al. (2014) uses Balmer decrements to estimate $E(B-V)_{gas}$, while other studies use SED fitting.

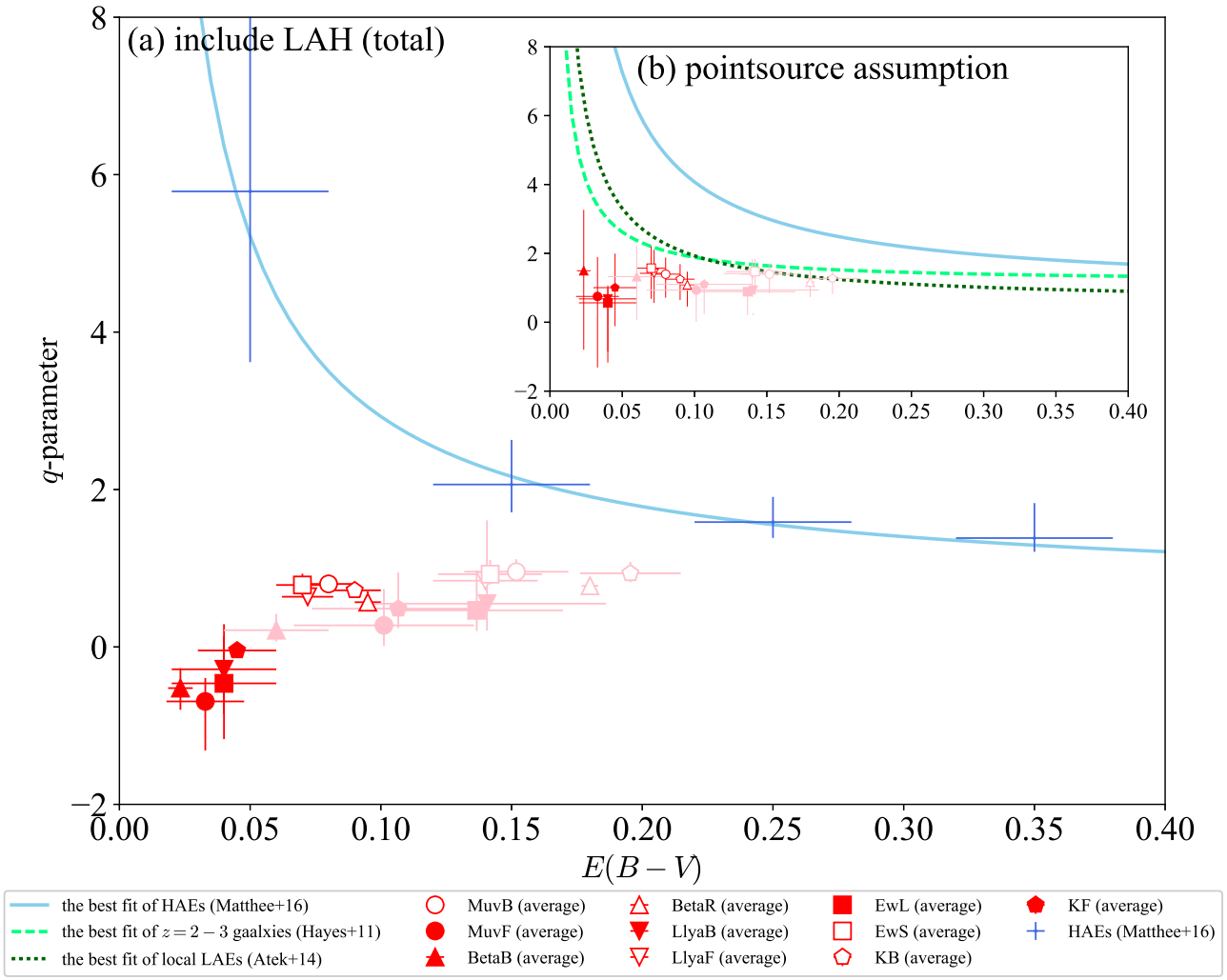

Fig. 8. The q parameter vs. $E(B-V)$. The LAH is included in calculation of q in panel (a), while not included in panel (b). Blue crosses and a solid skyblue line show the values of $E(B-V)$-subdivided HAEs in Matthee et al. (2016) and the best fit two-parameter model to them as described in footnote 13 (see also footnotes 8 and 9); 12 kpc and 24 kpc apertures are used in panels (a) and (b), respectively. A light green dashed line and a dark green dotted line represent the best fit relation for LAEs, HAES, and UV-selected galaxies at $z \sim 2$–3 in Hayes et al. (2011) and local LAEs in Atek et al. (2014), respectively. Field average values of our ten subsamples with an assumption of an SMC-like attenuation curve are shown by red symbols below: open (filled) circles for bright (faint) $M_{\rm UV}$, open (filled) triangles for red (blue) β, open (filled) inverted triangles for faint (bright) $L({\rm Ly}\alpha)_{ps}$, open (filled) squares for small (large) $EW_{0,ps}({\rm Ly}\alpha)$, and open (filled) pentagons for bright (faint) $m_{\rm K}$. Shown by pink symbols are the results with the Calzetti curve. $E(B-V)_\star = E(B-V)_g$ is assumed to derive $E(B-V)$. All data are rescaled to a Salpeter IMF according to footnote 1. (Color online)

$f_{\rm esc}({\rm Ly}\alpha)_{tot}$ than HAEs with the same $E(B-V)$, by grouping possible origins into three categories: (i) less efficient resonant scattering in a uniform ISM, (ii) less efficient resonant scattering in a clumpy ISM, and (iii) additional Lyα sources. We then discuss the difference in q and $f_{\rm esc}({\rm Ly}\alpha)_{tot}$ between the LAEs and HAEs. In this discussion, we assume that the contribution from cold streams and satellite galaxies to $L({\rm Ly}\alpha)_H$ is negligible.

6.2.1 (i) Less efficient resonant scattering in a uniform ISM

In a uniform ISM where dust and gas are well mixed, Lyα photons have a higher chance of dust absorption than continuum photons because of resonant scattering. To reduce the efficiency of resonant scattering in a uniform ISM, one needs to reduce the column density of HI gas ($N_{\rm HI}$) or the scattering cross section ($\sigma_{{\rm Ly}\alpha}$) (e.g., Duval et al. 2014; Garel et al. 2015).

First, it appears that LAEs indeed have lower $N_{\rm HI}$ than aver-

age galaxies with the same $M_\star$ (and hence the same $(E(B-V)$ since average galaxies are expected to follow a common IRX-$M_\star$ relation). This is because Kusakabe et al. (2018) suggest that LAEs at $z\sim2$ have lower $M_{\rm h}$ than expected from the average $M_\star$-$M_{\rm h}$ relation. At a fixed $M_\star$, a lower $M_{\rm h}$ means a lower baryon mass and hence a lower gas mass, and it is reasonable to expect that galaxies with a lower gas mass have a lower $N_{\rm HI}$. The $N_{\rm HI}$ of LAEs is further reduced if they have a high ionizing parameter as suggested by e.g., Nakajima & Ouchi (2014), Song et al. (2014), and Nakajima et al. (2018) or have a relatively face-on inclination (e.g., Verhamme et al. 2012; Yajima et al. 2012; Behrens & Braun 2014; Shibuya et al. 2014a; Kobayashi et al. 2016; Paulino-Afonso et al. 2018).

The idea that LAEs have lower $N_{\rm HI}$ than average galaxies appears to be consistent with results based on observed Lyα profiles that LAEs have lower $N_{\rm HI}$ than LBGs (e.g., Hashimoto et al. 2015; Verhamme et al. 2006). This idea is also consistent with an anti-correlation between $M_{\rm HI}$ and $f_{\rm esc}({\rm Ly}\alpha)$ found for local galaxies, although their $f_{\rm esc}({\rm Ly}\alpha)$ values at a fixed $E(B-V)$ are lower than those of our LAEs (Lyα Reference Sample Hayes et al. 2013; Östlin et al. 2014).

The probability of the resonant scattering of Lyα photons is also reduced if the ISM is outflowing, because the gas sees redshifted Lyα photons (e.g., Kunth et al. 1998; Verhamme et al. 2006). This mechanism should work in LAEs because most LAEs have outflows (e.g., Hashimoto et al. 2013; Shibuya et al. 2014b; Hashimoto et al. 2015; Guaita et al. 2017). Outflowing gas is also needed to reproduce observed Lyα profiles characterized by a relatively broad, asymmetric shape with a redshifted peak. Note, however, that it is not clear whether LAEs have higher outflow velocities than average galaxies with the same $M_\star$ and $E(B-V)$.

To summarize, low HI column densities combined with some other mechanisms such as outflows appear to contribute to the high $f_{\rm esc}({\rm Ly}\alpha)_{tot}$ seen in LAEs. However, none of these mechanisms can reduce q below unity as long as a uniform ISM is assumed.

6.2.2 (ii) Less efficient resonant scattering in a clumpy ISM

Lyα photons are not attenuated by dust if dust is confined in HI clumps (the clumpy ISMs; Neufeld 1991; Hansen & Peng Oh 2006) because Lyα photons are scattered on the surface of clumps before being absorbed by dust. Scarlata et al. (2009) find that the clumpy dust screen (ISMs) can reproduce observed line ratios of Lyα to Hα (or $f_{\rm esc}({\rm Ly}\alpha)$), and H$\alpha$ to Hβ (or$E(B-V)$) of local LAEs (see also Bridge et al. 2017). It is, however, not clear what causes such a clumpy ISM geometry especially for LAEs. Indeed, Laursen et al. (2013) argue that any real ISM is unlikely to give $q<1$. Duval et al. (2014) also find that the clumpy ISM model (Neufeld 1991) can achieve $q<1$ only under unrealistic conditions: a large covering factor of clumps with high $E(B-V)$, a low HI content in interclump regions, and a uniform, constant, and slow outflow.

6.2.3 (iii) Additional Lyα sources

If galaxies have other Lyα-photon sources in the main body besides star formation, the number of produced Lyα photons is larger than expected from the SFR, resulting in underestimation of q and overestimation of $f_{\rm esc}({\rm Ly}\alpha)_{tot}$. We discuss three candidate sources: AGNs, cold streams, and hard ionizing spectra.

First, the contribution of AGNs should be modest. This is because we have removed all objects detected in either X-ray, UV, or radio regarding them as AGNs, and because the fraction of obscured AGNs (AGNs without detection in either X-ray, UV, or radio) in the remaining sample is estimated to be only 2% (see Kusakabe et al. 2018).

Second, Lake et al. (2015) have found from hydrodynamical simulations of galaxies with $M_{\rm h}=10^{11.5}\,M_\odot$ at $z\sim3$ that the Lyα luminosity from cold streams in the central part of galaxies amounts to as high as $\sim45\%$ of that from star formation. This result may apply to our LAEs to some degree.

Third, if our LAEs have a hard ionizing spectrum as suggested in previous studies on higher-z LAEs (at $z\sim3$–7: e.g., Nakajima et al. 2016; Harikane et al. 2017; Nakajima et al. 2018), the intrinsic number of ionizing photons is larger than that assumed in equation 22. A hard ionizing spectrum arises from a young age, a low metallicity, a stellar population with a contribution of massive binary systems, an increasing star formation history, and/or a top-heavy IMF.

In any case, the very low q values ($\lesssim0$) seen in about half of our LAEs (red filled objects) indicate a non-neglible contribution from additional Lyα sources. Song et al. (2014) have also found several bright LAEs with $q<0$ as shown in their figure 14, where q would decrease more if they include $L({\rm Ly}\alpha)_{\rm H}$ in the calculation of $f_{\rm esc}({\rm Ly}\alpha)_{\rm H}$.

6.2.4 Summary of the mechanisms affecting the q-parameter

The origin of very high $f_{\rm esc}({\rm Ly}\alpha)_{tot}$ and very low q found for LAEs is a long-standing problem. This study makes this problem more serious by including $L({\rm Ly}\alpha)_H$ in the calculation of these parameters. Remarkably, all of our subsamples have $q<1$ and a half of them reach $q<0$.

Low $N_{\rm HI}$ and small $\sigma_{{\rm Ly}\alpha}$ should help to increase $f_{\rm esc}({\rm Ly}\alpha)_{tot}$ and reduce q to some degree. However, additional mechanisms are needed to reduce q less than unity, as highlighted by the very low q values, with some being negative, found for our LAE subsamples. Cold streams in the main body of LAEs and hard ionizing spectra are candidate mechanisms while a clumpy ISM may be unlikely. The q value of galaxies is probably determined by the balance between

the efficiency of resonant scattering and additional Lyα-photon sources. Spectroscopic observations of LAEs' Hα luminosities would provide more accurate measurements of $f_{\rm esc}({\rm Ly}\alpha)_{tot}$ (q-parameters). They will also enable us to evaluate the spectral hardness from the UV to Hα luminosity ratio and to constrain the contribution of cold streams from the Lyα to Hα luminosity ratio.

Our LAEs have much lower q values than the HAEs in the lowest-$E(B-V)$ bin, which indicates that not all galaxies with small $E(B-V)$ (or equivalently, small $M_\star$) can be LAEs. A possible reason for this large difference is that our LAEs have lower $M_{\rm h}$ and hence lower $M_{\rm HI}$. Matthee et al. (2016)'s HAEs in the lowest-$M_\star$ bin ($M_\star \sim 3\times10^9$–$8\times10^9\,M_\odot$) used for clustering analysis by Cochrane et al. (2018) reside in massive dark matter halos of $M_{\rm h} \sim 7^{+9}_{-4}\times10^{12}\,M_\odot$ (Cochrane et al. 2018), which is one dex larger than the average $M_{\rm h}$ of our LAEs [14]. It would imply that the lowest-$E(B-V)$ HAEs in Matthee et al. (2016) have higher $M_{\rm h}$ than our LAEs, since the lowest-$E(B-V)$ HAEs should largely overlap with the lowest-$M_\star$ HAEs. Furthermore, a large fraction of low-$M_\star$ ($M_\star \lesssim 10^9\,M_\star$) HAEs are expected to be star burst galaxies as shown in figure 4, implying a large amount of gas (including HI) to fuel the star burst. However, the higher $M_{\rm h}$ also imply that they have brighter $L({\rm Ly}\alpha)$ from cold streams (in the main body). If the higher $M_{\rm HI}$ can reduce the $L({\rm Ly}\alpha)$ produced from both star formation and cold streams sufficiently, the higher q values of the HAEs can be reproduced.

7 Conclusions

We have studied the dependence of LAH luminosity on stellar properties and dark matter halo mass using ~900 star forming LAEs at $z\sim2$ to identify the dominant origin of LAHs. To do so, we have divided the whole sample into ten subsamples in accordance with five physical quantities ($m_{\rm K}$, $M_{\rm UV}$, β, $L({\rm Ly}\alpha)$ and $EW_0({\rm Ly}\alpha)$), some of which are expected to correlate with $M_\star$ and $M_{\rm h}$. We have estimated for each subsample the LAH luminosity from a stacked observational relation obtained by Momose et al. (2016). We have used the thus obtained dependence of LAH luminosity to test three candidate origins: cold streams, satellite star formation, and resonant scattering. We have also derived total Lyα escape fractions and q values by including the halo component, and discussed how LAEs can have high escape fractions. Our main results are as follows.

1. We compare Momose et al. (2016)'s observational $L({\rm Ly}\alpha)_C$–$L({\rm Ly}\alpha)_H$ relation obtained from stacking analysis of essentially the same sample as ours, with the distribution of individual LAEs by VLT/MUSE in Leclercq et al. (2017). We find that their observational relation agree well with the average trend of individual LAEs as shown in figure 2, ensuring the use of the relation for our analysis.
2. Our LAEs are found to lie on an extrapolation of the $M_\star$–IRX relation at $z\sim1.5$ in Heinis et al. (2014) and that of the SFMS at $z\sim2$ in Shivaei et al. (2017) if an SMC-like attenuation curve is assumed (shown in figures 3 and 4). These results are used in the discussion of the origin of LAHs.
3. The ten subdivided LAE samples are found to have similar $L({\rm Ly}\alpha)_H \sim 2\times10^{42}\,{\rm erg\,s^{-1}}$ and $L({\rm Ly}\alpha)_{tot} \sim 2\times10^{42}$–$4\times10^{42}\,{\rm erg\,s^{-1}}$ (shown in figure 2). Their $L({\rm Ly}\alpha)_H$ and $L({\rm Ly}\alpha)_{tot}$ remain almost unchanged or even decrease when $M_\star$ increases by factor 2–5. They are also nearly independent of SFR, $E(B-V)_\star$, and $M_{\rm h}$, although the uncertainties in $M_{\rm h}$ are large. The HAEs in Matthee et al. (2016) also have non-increasing $L({\rm Ly}\alpha)_H$ and $L({\rm Ly}\alpha)_{tot}$. These results are inconsistent with the cold streams scenario and the satellite star formation scenario both of which predict a nearly linear scaling of $L({\rm Ly}\alpha)_H$ with mass (figure 7). Specifically, the power law slope of the $M_\star$–$L({\rm Ly}\alpha)_H$ relation for the K-divided subsamples, the most stellar-mass sensitive subsamples, is shallower than predictions with more than the 2σ confidence level. The former scenario also fails to reproduce the bright $L({\rm Ly}\alpha)_H$ of low-mass subsamples at, e.g., a more than the 10σ level for the faint m_K subsample. The most likely is the resonant scattering scenario because it can naturally explain these results.
4. The $f_{\rm esc}({\rm Ly}\alpha)_{tot}$ of all ten subsamples is higher than $\sim30\%$, with some exceeding 100%, with very low q values of $-1\lesssim q\lesssim1$. Using the Calzetti curve instead of an SMC-like curve makes $f_{\rm esc}({\rm Ly}\alpha)_{tot}$ lower but still in a range of 10–100% with $q\sim0$–1. The $f_{\rm esc}({\rm Ly}\alpha)_{tot}$ of the LAEs anti-correlates with $M_\star$, SFR, and $E(B-V)$ regardless of the assumed attenuation curve (figure 6). Their $f_{\rm esc}({\rm Ly}\alpha)_{tot}$ and q are higher and lower, respectively, than those of HAEs with similar $M_\star$ and $E(B-V)$. The very low q values of the LAEs suggest the existence of an additional Lyα source in the main body; Lyα emission from cold streams is a possible candidate. The difference in q between the LAEs and HAEs is possibly caused by a different balance between resonant scattering and additional Lyα-photon source(s).

In the near future, we will obtain much better $M_{\rm h}$ estimates for ~9000 LAEs with new $NB387$ data from $\simeq25$ deg^2 taken with Hyper Suprime-Cam (SILVERRUSH; Ouchi et al. 2018; Shibuya et al. 2018) as part of a large imaging survey program (Aihara et al. 2018). It will enable us to compare observed relations of $L({\rm Ly}\alpha)_{tot}$ with theoretical predictions more directly.

[14] We calculate this $M_{\rm h}$ value from the correlation length given in Cochrane et al. (2018) in the same manner as for our LAEs. Their r_0 and $M_{\rm h}$ are higher than those averaged over all the LAEs ($r_0 = 2.30^{+0.36}_{-0.41}\,h^{-1}\,Mpc$, i.e., $3.2^{+4.7}_{-2.5}\times10^{10}\,M_\odot$), although their median $M_\star$ ($\sim6\times10^9\,M_\odot$) is slightly higher than our average value ($\sim1\times10^9\,M_\odot$).

Acknowledgments

We are grateful to Yoshiaki Ono for giving insightful comments and suggestions on SED fitting. We would like to express our gratitude to Jorryt Matthee and Ken-ichi Tadaki for kindly providing their data plotted in figures 4, and 6–8 and figure 4, respectively. We acknowledge Ryosuke Goto, Akira Konno, Ryota Kawamata, Taku Okamura, Kazushi Irikura, Ryota Kakuma, and Makoto Ando for constructive discussions at meetings. This work is based on observations taken by the Subaru Telescope which is operated by the National Astronomical Observatory of Japan. The authors wish to recognize and acknowledge the very significant cultural role and reverence that the summit of Maunakea has always had within the indigenous Hawaiian community. Based on data products produced by TERAPIX and the Cambridge Astronomy Survey Unit on behalf of the UltraVISTA consortium. This research made use of IRAF, which is distributed by NOAO, which is operated by AURA under a cooperative agreement with the National Science Foundation and of Python packages for Astronomy: Astropy (The Astropy Collaboration et al. 2013), Colossus, CosmoloPy and PyRAF, which is produced by the Space Telescope Science Institute, which is operated by AURA for NASA. H.K acknowledges support from the JSPS through the JSPS Research Fellowship for Young Scientists. This work is supported in part by KAKENHI (16K05286) Grant-in-Aid for Scientific Research (C) through the JSPS.

Appendix 1 NB selection bias

In this Appendix, we first describe the NB-selection bias of our LAE sample, and then discuss the effect of this bias on the obtained $M_\star$–$L(\mathrm{Ly}\alpha)_H$ relations. As shown in figures 1 (g) and (h), our sample misses UV-faint LAEs ($M_{UV} \gtrsim -19$ mag) with faint $L(\mathrm{Ly}\alpha)_{ps}$ and small $EW_{0,ps}(\mathrm{Ly}\alpha)$. This selection bias has the following effects on subsample properties.

M_{UV} and m_K subsamples The UV-faint ($M_{UV} > -19.2$ mag) subsample is biased toward brighter $L(\mathrm{Ly}\alpha)_{ps}$ and larger $EW_{0,ps}(\mathrm{Ly}\alpha)$. The K-faint subsample ($m_K > 25.0$ mag) is probably biased similarly. Although the $L(\mathrm{Ly}\alpha)_H$ of these subsamples is probably overestimated, we find in appendix 2 that it does not change our results. This selection bias probably does not change $M_\star$ values since m_K and M_{UV} are a good tracer of $M_\star$. The bright m_K and M_{UV} subsamples are almost free from this bias.

β subsamples Galaxies with fainter UV luminosities generally have smaller β (e.g., Alavi et al. 2014). Although our β subsamples are probably biased to some degree, it is difficult to evaluate the effects on $M_\star$ and $L(\mathrm{Ly}\alpha)_H$ estimates quantitatively. However, the effects should be smaller than those on the UV and K subsamples, since the M_{UV}–β correlation has a large scatter (see figure 1 [f]).

$L(\mathrm{Ly}\alpha)_{ps}$ and $EW_{0,ps}$(Lyα) subsamples The faint $L(\mathrm{Ly}\alpha)$ and small $EW(\mathrm{Ly}\alpha)$ subsamples are biased toward bright UV magnitudes. Although their $L(\mathrm{Ly}\alpha)_H$ values are probably not affected by the selection bias, their $M_\star$ values are expected to be overestimated to some degree. The bright $L(\mathrm{Ly}\alpha)$ and large $EW(\mathrm{Ly}\alpha)$ subsamples are not biased. If the $M_\star$ of the faint $L(\mathrm{Ly}\alpha)$ and small $EW(\mathrm{Ly}\alpha)$ subsamples decreases, the power-law slope of the $M_\star$–$L(\mathrm{Ly}\alpha)_H$ relation becomes shallower, enlarging the descrepancy from the models of cold streams and satellite star formation.

In the next Appendix, we use the MUSE sample to evaluate the robustness of $L(\mathrm{Ly}\alpha)_H$ estimates for our faint m_K and M_{UV} subsamples. The MUSE sample is complementary to our sample, because it is essentially UV-limited but contains much fewer objects than ours.

Appendix 2 Robustness of $L(\mathrm{Ly}\alpha)_H$ estimates

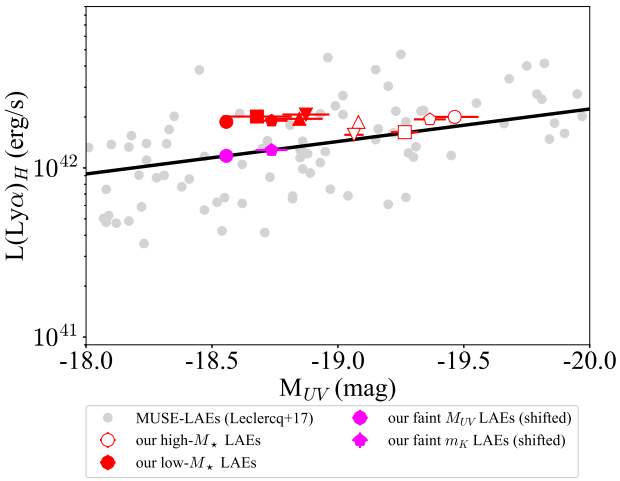

Fig. 9. $L(\mathrm{Ly}\alpha)_H$ as a function of M_{UV}. Grey points represent MUSE-LAEs at $z \sim 3-6$ and a black solid line the best fit of a linear function to them (Leclercq et al. 2017). The field average values of our ten subsamples using the stacked relation (equation 10) are shown by red symbols below: open (filled) circles for bright (faint) M_{UV}, open (filled) triangles for red (blue) β, open (filled) inverted triangles for faint (bright) $L(\mathrm{Ly}\alpha)_{ps}$, open (filled) squares for small (large) $EW_{0,ps}(\mathrm{Ly}\alpha)$, and open (filled) pentagons for bright (faint) m_{K}. Results using Leclercq et al. (2017)'s relation for two subsamples are shown by filled magenta symbols: a circle for the faint M_{UV} subsample and a pentagon for the faint m_K subsample. (Color online)

We first examine the robustness of the stacked relation (equation 10) in Momose et al. (2016). We then evaluate the

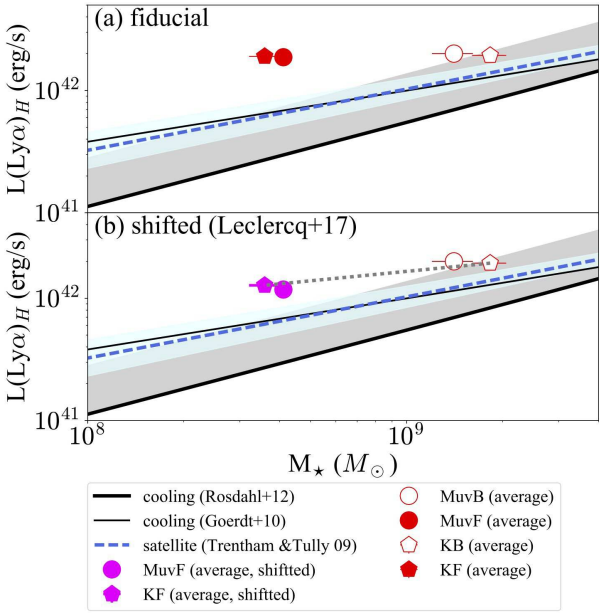

Fig. 10. $L(\mathrm{Ly}\alpha)_H$ vs. $M_\star$: (a) the fiducial results and (b) NB-selection bias corrected results using the M_{UV}–$L(\mathrm{Ly}\alpha)_H$ relation in Leclercq et al. (2017). The field average values of our M_{UV} and m_K subsamples using the stacked relation (equation 10) are shown by red symbols below: open (filled) circles for bright (faint) M_{UV}, and open (filled) pentagons for bright (faint) m_{K}. Results using Leclercq et al. (2017)'s relation for two subsamples are shown by filled magenta symbols: a circle for the faint M_{UV} subsample and a pentagon for the faint m_K subsample. Thick and thin solid black lines show the Lyα luminosities from cooling flows by theoretical models in Rosdahl & Blaizot (2012) and Goerdt et al. (2010), respectively, which are converted from original $M_\star$–$L(\mathrm{Ly}\alpha)_H$ relations using the $M_\star$–M_{h} relation in Moster et al. (2013). Gray shaded regions above the solid black lines roughly indicate the distribution of Rosdahl & Blaizot (2012)'s simulated galaxies above the solid line, whose $L(\mathrm{Ly}\alpha)_H$ reaches at most ~ 2.5 times higher than the line. Dashed blue lines show the Lyα luminosity from the star formation in satellite galaxies, normalized to the cold streams model by Rosdahl & Blaizot (2012). Cyan shaded regions around the dashed blue lines indicate the 1σ uncertainty in the power law index in Trentham & Tully (2009). A dotted black line in panel (b) shows the slope determined by the m_K subsamples. (Color online)

effects of the NB-selection bias on the m_K and M_{UV} subsamples.

To test the robustness of $L(\mathrm{Ly}\alpha)_H$ values derived from equation 10, we calculate $L(\mathrm{Ly}\alpha)_H$ from $EW_{0,ps}(L_{\mathrm{Ly}\alpha})$ using another stacked relation presented in Momose et al. (2016), an anti-correlation between $\mathrm{X}(L_{\mathrm{Ly}\alpha})_{\mathrm{tot/C}}$ and $EW_{0,ps}(L_{\mathrm{Ly}\alpha})$. We find that using this relation gives nearly the same $L(\mathrm{Ly}\alpha)_H$ values as those derived from equation 10, with differences being at most 0.09 dex.

To evaluate the effects of the NB-selection bias on $L(\mathrm{Ly}\alpha)_H$ for the faint m_K and M_{UV} subsamples, we re-estimate $L(\mathrm{Ly}\alpha)_H$ with a complementary result of the MUSE-LAEs in Leclercq et al. (2017) which is essentially free from this kind of bias: the relation between M_{UV} and $L(\mathrm{Ly}\alpha)_H$. They have found $L(\mathrm{Ly}\alpha)_H$ anti-correlates with L_{UV} (see their figure 16). As shown in figure 9, our high-$M_\star$ LAEs (red filled objects), which are not affected by the NB-bias, are consistent with the best-fit relation of MUSE-LAEs (black solid line), while the faint m_K and M_{UV} subsamples are found to lie alightly above the relation. As a result, the power-law slopes of the m_K and M_{UV} subsamples become positive as shown in figure 10. However, they are still shallow. For example, the m_K-divided subsamples give a power-law index of 0.26 ± 0.05, which is more than 2σ shallower than those of the cold streams models in Goerdt et al. (2010) and Rosdahl & Blaizot (2012), ~ 0.38 and ~ 0.75, respectively. This slope is also more than 2σ shallower than that of the satellite star formation model, $\sim 0.49^{+0.13}_{-0.12}$. Moreover, the $L(\mathrm{Ly}\alpha)_H$ values of the faint m_K and M_{UV} subsamples also remain higher than predicted from the cold streams models at a $> 10\sigma$ level. We conclude that the conclusions obtained in section 6 are robust.

Table 5. Lyα luminosities for the subsamples.

subsamples	$L(\mathrm{Ly}\alpha)_C$ $10^{41}\,L_\odot$ (1)	$L(\mathrm{Ly}\alpha)_H$ $10^{41}\,L_\odot$ (2)	$L(\mathrm{Ly}\alpha)_{tot}$ $10^{41}\,L_\odot$ (3)
SXDS			
bright UV	$7.7^{+2.3}_{+1.5}$	$15.9^{+2.0}_{+1.7}$	$23.6^{+4.3}_{+3.2}$
faint UV	$9.4^{+1.8}_{+0.8}$	$17.5^{+1.4}_{+0.7}$	$26.9^{+3.2}_{+1.5}$
blue β	$9.1^{+2.1}_{+1.2}$	$17.3^{+1.6}_{+1.1}$	$26.4^{+3.7}_{+2.4}$
red β	$8.5^{+1.8}_{+0.9}$	$16.8^{+1.5}_{+0.9}$	$25.3^{+3.4}_{+1.8}$
bright Lyα	$13.8^{+2.4}_{+1.1}$	$20.2^{+0.8}_{+0.5}$	$34.0^{+3.3}_{+1.5}$
faint Lyα	$6.2^{+1.9}_{+1.0}$	$14.3^{+2.1}_{+1.4}$	$20.5^{+4.1}_{+2.4}$
large EW	$12.5^{+2.1}_{+0.8}$	$19.6^{+0.9}_{+0.4}$	$32.1^{+3.1}_{+1.2}$
small EW	$6.6^{+2.1}_{+1.3}$	$14.7^{+2.2}_{+1.7}$	$21.3^{+4.2}_{+3.0}$
bright K	$7.9^{+2.3}_{+1.2}$	$16.1^{+2.0}_{+1.3}$	$24.0^{+4.4}_{+2.5}$
faint K	$9.1^{+1.9}_{+0.9}$	$17.3^{+1.5}_{+0.8}$	$26.3^{+3.4}_{+1.7}$
COSMOS			
bright UV	$14.7^{+3.0}_{+1.4}$	$20.6^{+0.8}_{+0.6}$	$35.3^{+3.8}_{+2.0}$
faint UV	$11.9^{+2.0}_{+0.6}$	$19.2^{+1.0}_{+0.4}$	$31.1^{+2.9}_{+1.0}$
blue β	$13.5^{+2.4}_{+1.0}$	$20.1^{+0.9}_{+0.5}$	$33.5^{+3.2}_{+1.5}$
red β	$12.4^{+2.3}_{+0.9}$	$19.5^{+1.0}_{+0.5}$	$31.9^{+3.3}_{+1.5}$
bright Lyα	$15.7^{+2.5}_{+0.9}$	$20.9^{+0.5}_{+0.3}$	$36.6^{+3.1}_{+1.2}$
faint Lyα	$8.1^{+1.8}_{+0.8}$	$16.4^{+1.6}_{+0.8}$	$24.5^{+3.4}_{+1.7}$
large EW	$14.3^{+2.4}_{+0.7}$	$20.4^{+0.7}_{+0.3}$	$34.7^{+3.1}_{+0.9}$
small EW	$8.9^{+2.2}_{+1.2}$	$17.1^{+1.7}_{+1.1}$	$26.0^{+3.9}_{+2.3}$
bright K	$13.4^{+2.7}_{+1.1}$	$20.0^{+1.0}_{+0.6}$	$33.4^{+3.6}_{+1.7}$
faint K	$12.6^{+2.1}_{+0.8}$	$19.6^{+0.9}_{+0.4}$	$32.2^{+3.0}_{+1.2}$

Note. (1) Lyα luminosity at the central part derived by multiplying $L(\mathrm{Ly}\alpha)_{ps}$ by 0.77; (2) Lyα luminosity of the LAH derived from equation 10; (3) total Lyα luminosity derived from equation 10.

Appendix 3 Estimated Lyα luminosities

In table 5, we show the three kinds of Lyα luminosities for individual subsamples. Note that the typical 1σ uncertainties in the individual data points in Momose et al. (2016)'s $L(\mathrm{Ly}\alpha)_C$ - $L(\mathrm{Ly}\alpha)_H$ relation are propagated to uncertainties in $L(\mathrm{Ly}\alpha)_H$ and $L(\mathrm{Ly}\alpha)_{tot}$ of $\sim 22\%$ and $\sim 16\%$, respectively (see figure 5

Table 6. Best-fit parameters of SED fitting for the two fields.

subsample	$M_\star$ ($10^8 M_\odot$) (1)	$E(B-V)_\star$ (mag) (2)	Age (Myr) (3)	SFR ($M_\odot \mathrm{yr}^{-1}$) (4)	χ^2_r (5)
SXDS field/ SMC-like attenuation curve					
bright UV	$12.5^{+4.5}_{-2.1}$	$0.07^{+0.01}_{-0.02}$	255^{+198}_{-74}	$5.9^{+0.9}_{-1.3}$	0.538
faint UV	$4.1^{+1.4}_{-1.5}$	$0.02^{+0.02}_{-0.01}$	321^{+188}_{-178}	$1.5^{+0.5}_{-0.2}$	0.139
blue β	$7.1^{+2.4}_{-1.8}$	$0.02^{+0.01}_{-0.01}$	404^{+236}_{-149}	$2.1^{+0.4}_{-0.3}$	0.588
red β	$14.9^{+3.2}_{-3.8}$	$0.10^{+0.02}_{-0.01}$	286^{+118}_{-125}	$6.2^{+1.8}_{-0.8}$	2.282
bright Lyα	$6.9^{+1.6}_{-2.3}$	$0.02^{+0.02}_{-0.01}$	453^{+187}_{-226}	$1.9^{+0.5}_{-0.2}$	0.289
faint Lyα	$11.5^{+4.3}_{-2.0}$	$0.06^{+0.01}_{-0.02}$	360^{+280}_{-105}	$3.9^{+0.6}_{-0.8}$	1.461
large EW	$4.5^{+1.6}_{-1.5}$	$0.02^{+0.02}_{-0.01}$	360^{+211}_{-180}	$1.5^{+0.5}_{-0.2}$	0.255
small EW	$11.7^{+4.3}_{-2.0}$	$0.06^{+0.01}_{-0.02}$	321^{+250}_{-94}	$4.4^{+0.7}_{-0.9}$	0.775
bright K	$21.5^{+5.5}_{-5.3}$	$0.08^{+0.01}_{-0.02}$	453^{+265}_{-167}	$5.8^{+1.0}_{-1.1}$	0.680
faint K	$3.8^{+1.3}_{-1.4}$	$0.03^{+0.02}_{-0.02}$	203^{+158}_{-112}	$2.2^{+0.8}_{-0.5}$	0.692
SXDS field/ the Calzetti attenuation curve					
bright UV	$12.0^{+3.0}_{-3.8}$	$0.13^{+0.03}_{-0.03}$	143^{+112}_{-79}	$9.7^{+4.5}_{-2.7}$	0.902
faint UV	$3.1^{+2.3}_{-1.8}$	$0.06^{+0.05}_{-0.05}$	161^{+348}_{-128}	$2.3^{+2.3}_{-1.0}$	0.114
blue β	$6.7^{+2.7}_{-2.4}$	$0.04^{+0.05}_{-0.03}$	321^{+320}_{-207}	$2.5^{+1.8}_{-0.7}$	0.581
red β	$16.0^{+3.7}_{-4.0}$	$0.18^{+0.02}_{-0.02}$	161^{+94}_{-70}	$11.6^{+3.5}_{-2.4}$	2.978
bright Lyα	$5.2^{+3.3}_{-3.3}$	$0.07^{+0.06}_{-0.06}$	203^{+438}_{-174}	$3.0^{+4.0}_{-1.4}$	0.268
faint Lyα	$10.9^{+3.2}_{-2.7}$	$0.12^{+0.02}_{-0.04}$	203^{+202}_{-89}	$6.4^{+1.9}_{-2.1}$	1.550
large EW	$2.8^{+3.3}_{-1.9}$	$0.09^{+0.04}_{-0.08}$	102^{+469}_{-85}	$3.1^{+2.8}_{-1.8}$	0.212
small EW	$11.1^{+2.9}_{-2.9}$	$0.12^{+0.03}_{-0.03}$	181^{+141}_{-90}	$7.2^{+3.0}_{-2.0}$	1.016
bright K	$16.1^{+5.8}_{-4.2}$	$0.17^{+0.03}_{-0.04}$	143^{+143}_{-72}	$13.0^{+5.5}_{-4.4}$	1.012
faint K	$3.6^{+1.3}_{-1.5}$	$0.06^{+0.03}_{-0.03}$	143^{+143}_{-91}	$2.9^{+1.5}_{-0.8}$	0.673
COSMOS field/ SMC-like attenuation curve					
bright UV	$16.8^{+5.9}_{-2.9}$	$0.09^{+0.01}_{-0.02}$	227^{+177}_{-66}	$8.8^{+1.3}_{-1.9}$	0.377
faint UV	$4.2^{+2.7}_{-1.8}$	$0.05^{+0.02}_{-0.02}$	227^{+282}_{-137}	$2.2^{+0.9}_{-0.5}$	0.244
blue β	$2.3^{+2.5}_{-1.8}$	$0.03^{+0.02}_{-0.02}$	114^{+246}_{-105}	$2.3^{+2.7}_{-0.7}$	0.458
red β	$13.1^{+4.8}_{-2.3}$	$0.09^{+0.01}_{-0.02}$	286^{+223}_{-84}	$5.5^{+0.8}_{-1.2}$	0.560
bright Lyα	$8.5^{+2.8}_{-2.7}$	$0.06^{+0.02}_{-0.01}$	286^{+167}_{-143}	$3.6^{+1.1}_{-0.5}$	0.257
faint Lyα	$13.5^{+4.6}_{-3.3}$	$0.08^{+0.01}_{-0.01}$	360^{+211}_{-133}	$4.6^{+0.8}_{-0.6}$	2.238
large EW	$8.1^{+2.8}_{-2.6}$	$0.06^{+0.02}_{-0.01}$	321^{+188}_{-160}	$3.1^{+1.0}_{-0.4}$	0.311
small EW	$19.5^{+7.3}_{-3.5}$	$0.08^{+0.01}_{-0.02}$	404^{+315}_{-118}	$5.9^{+0.8}_{-1.2}$	3.052
bright K	$16.7^{+3.5}_{-4.2}$	$0.10^{+0.02}_{-0.01}$	227^{+94}_{-99}	$8.7^{+2.5}_{-1.1}$	0.208
faint K	$2.9^{+2.2}_{-2.4}$	$0.06^{+0.02}_{-0.02}$	114^{+172}_{-107}	$3.0^{+4.2}_{-0.8}$	0.278
COSMOS field/ the Calzetti attenuation curve					
bright UV	$15.5^{+5.5}_{-5.6}$	$0.17^{+0.02}_{-0.03}$	102^{+101}_{-57}	$17.4^{+6.7}_{-5.1}$	1.185
faint UV	$2.6^{+2.5}_{-1.1}$	$0.13^{+0.02}_{-0.05}$	57^{+170}_{-32}	$5.1^{+2.1}_{-2.4}$	0.213
blue β	$1.7^{+2.6}_{-1.0}$	$0.08^{+0.02}_{-0.06}$	47^{+239}_{-35}	$3.9^{+1.9}_{-2.1}$	0.413
red β	$10.9^{+5.1}_{-3.4}$	$0.18^{+0.02}_{-0.03}$	102^{+126}_{-52}	$12.2^{+4.2}_{-3.8}$	1.305
bright Lyα	$3.8^{+3.0}_{-1.0}$	$0.17^{+0.01}_{-0.04}$	35^{+79}_{-12}	$11.8^{+2.4}_{-5.0}$	0.377
faint Lyα	$13.4^{+3.5}_{-3.5}$	$0.16^{+0.03}_{-0.03}$	181^{+141}_{-90}	$8.7^{+3.7}_{-2.4}$	2.609
large EW	$4.4^{+3.4}_{-1.4}$	$0.16^{+0.02}_{-0.04}$	57^{+123}_{-28}	$8.6^{+3.1}_{-3.5}$	0.368
small EW	$19.3^{+5.1}_{-4.8}$	$0.16^{+0.02}_{-0.03}$	203^{+158}_{-89}	$11.2^{+3.3}_{-3.0}$	3.267
bright K	$9.7^{+4.2}_{-1.4}$	$0.21^{+0.02}_{-0.02}$	40^{+41}_{-11}	$26.3^{+6.0}_{-7.0}$	1.057
faint K	$1.7^{+1.2}_{-0.7}$	$0.13^{+0.02}_{-0.01}$	26^{+38}_{-14}	$6.7^{+1.9}_{-1.7}$	0.279

Note. (1) Stellar mass; (2) color excess; (3) age; (4) SFR; and (5) reduced χ^2 value.
Metallicity is fixed to $0.2\mathrm{Z}_\odot$, redshift to 2.18, and $f_{\mathrm{esc}}^{\mathrm{ion}}$ to 0.2.

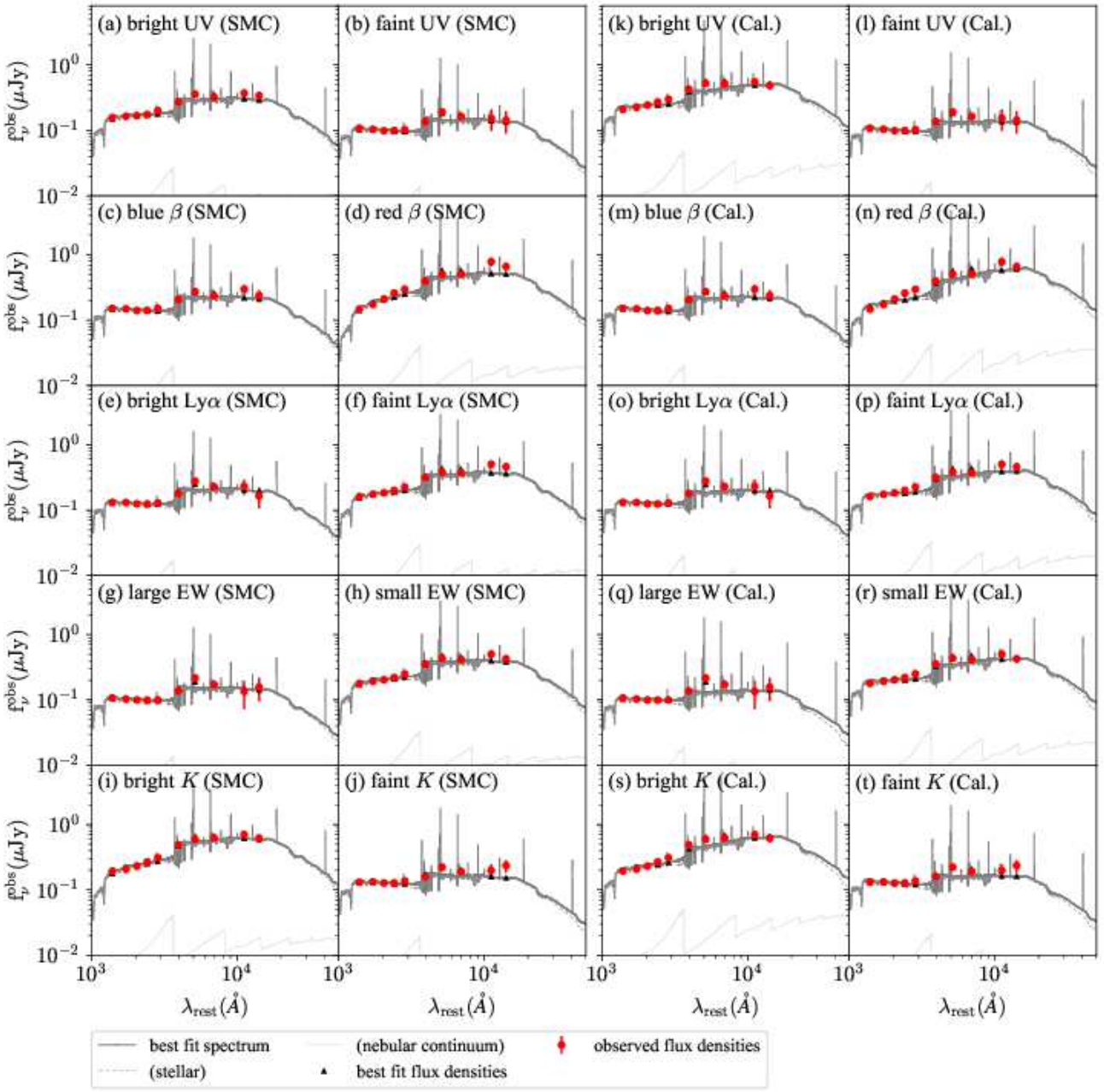

Fig. 11. Best-fit SEDs for the ten subsamples of the SXDS field. Panels (a)–(h) show results with an assumption of SMC-like attenuation curve: (a) bright UV, (b) faint UV, (c) blue β, (d) red β, (e) bright Lyα, (f) faint Lyα, (g) bright K, and (h) faint K, while panels (i)–(t) show those with an assumption of Calzetti curve. For each panel, a gray solid line, a light gray solid line and a light gray dotted line show the best-fit model spectrum, its nebular continuum component and its stellar continuum component, respectively. Red filled circles and black filled triangles represent the observed flux densities and the flux densities calculated from the best-fit spectrum, respectively. (Color online)

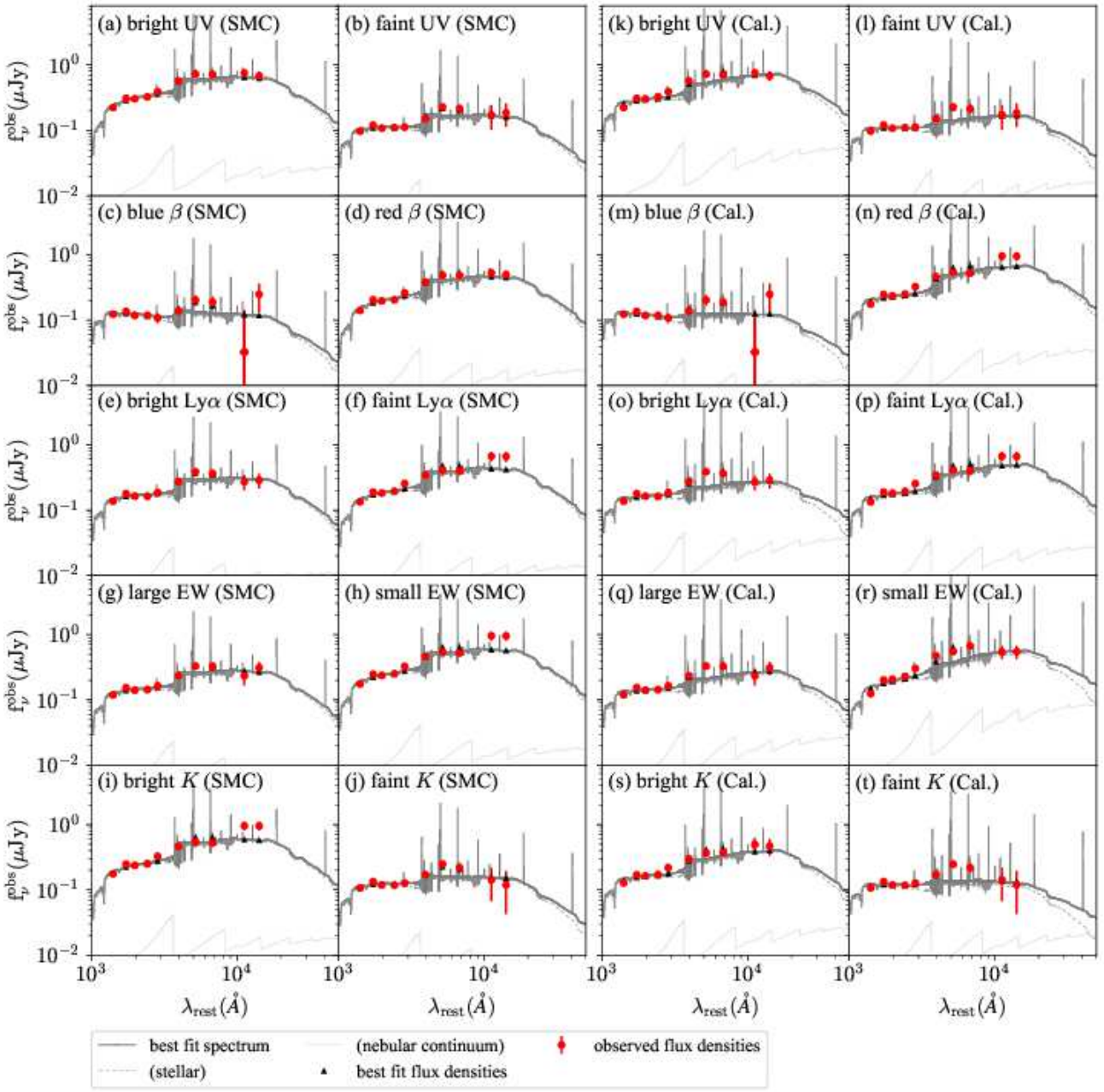

Fig. 12. Best-fit SEDs for the ten subsamples of the COSMOS field. Panels (a)–(h) show results with an assumption of SMC-like attenuation curve: (a) bright UV, (b) faint UV, (c) blue β, (d) red β, (e) bright Lyα, (f) faint Lyα, (g) bright K, and (h) faint K, while panels (i)–(t) show those with an assumption of Calzetti curve. For each panel, a gray solid line, light gray solid line and a light gray dotted line show the best-fit model spectrum, its nebular continuum component and its stellar continuum component, respectively. Red filled circles and black filled triangles represent the observed flux densities and the flux densities calculated from the best-fit spectrum, respectively. (Color online)

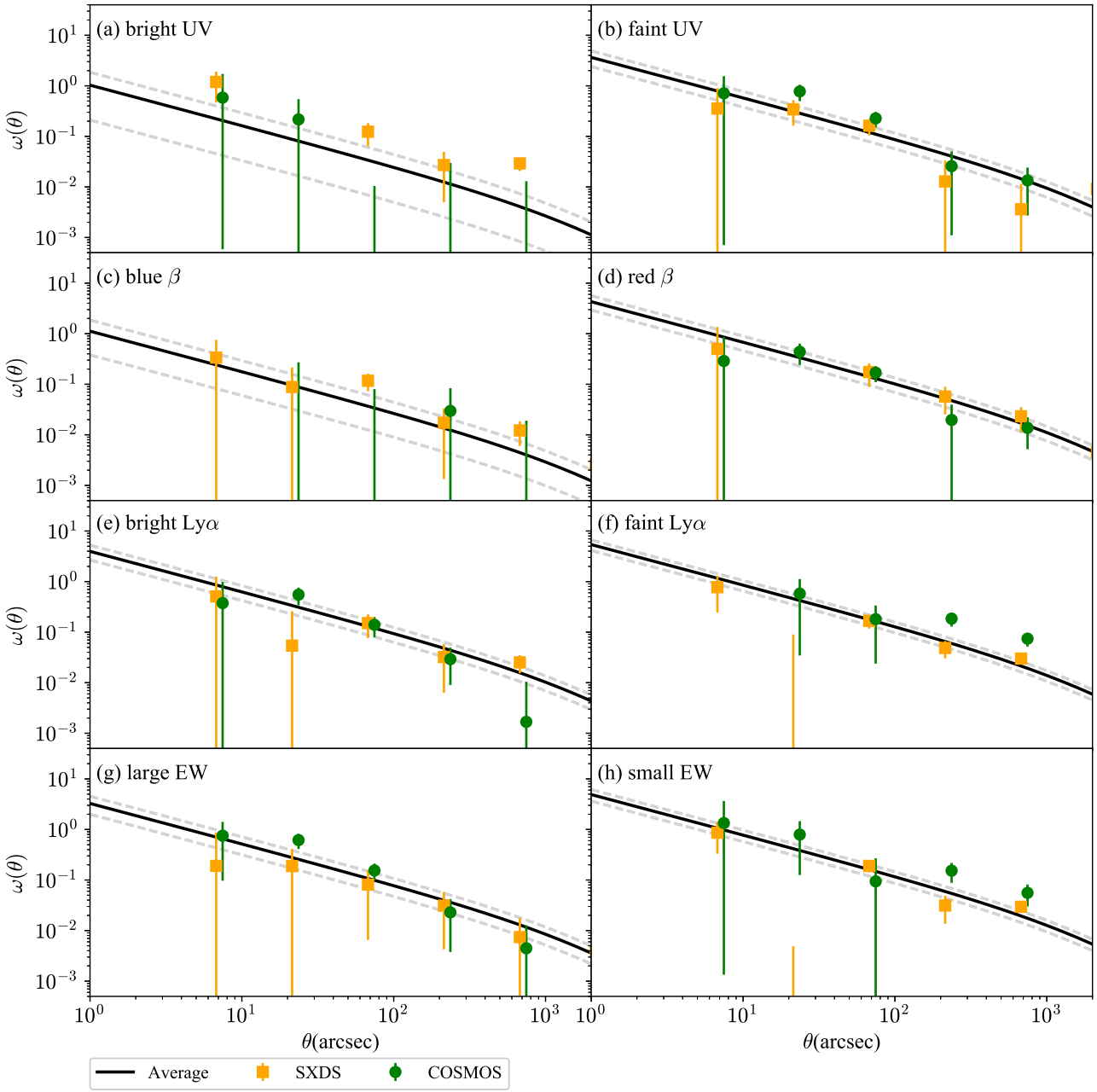

Fig. 13. ACF measurements for the eight subsamples: (a) bright UV, (b) faint UV, (c) blue β, (d) red β, (e) bright Lyα, and (f) faint Lyα. For each panel, orange filled squares and green filled circles represent measurements in the SXDS and COSMOS fields. A black solid line and light gray dotted line indicate the field-average best-fit ACFs with fixed $\beta = 0.8$, whose fitting range is 40–$1000''$. we slightly shift all data points along the abscissa by a value depending on the field for presentation purpose. (Color online)

Appendix 4 Results of the SED fitting

Figures 11 and 12 show the best-fit SEDs for the ten subsamples for each field, and table 3 the best-fit stellar parameters.

Appendix 5 The best fit ACFs

We show the best-fit ACFs for the two fields and their field-average values in figure 13. We do not perform clustering analysis for the K-divided subsamples as described in section 3.2. We do not plot the $M_{\rm h}$ of the UV bright and blue β subsamples (figures 5 and 7), since they are not constrained well. This is partly because at small r_0 values like those of these two subsamples, $M_{\rm h}$ depends very sensitively on r_0 according to the bias model (see appendix B in Khostovan et al. 2017). The differences in the ACF measurement between the two fields have been discussed in Kusakabe et al. (2018).

References

Aihara, H., Arimoto, N., Armstrong, R., et al. 2018, Publications of the Astronomical Society of Japan, 70, 1

Alavi, A., Siana, B., Richard, J., et al. 2014, The Astrophysical Journal, 780, 143

Álvarez-Márquez, J., Burgarella, D., Heinis, S., et al. 2016, Astronomy & Astrophysics, 587, A122

Ando, M., Ohta, K., Iwata, I., et al. 2006, The Astrophysical Journal, 645, L9

—. 2007, Publications of the Astronomical Society of Japan, 59, 717

Atek, H., Kunth, D., Hayes, M., Östlin, G., & Mas-Hesse, J. M. 2008, Astronomy and Astrophysics, 488, 491

Atek, H., Kunth, D., Schaerer, D., et al. 2014, Astronomy & Astrophysics, 561, A89

Barnes, L. A., & Haehnelt, M. G. 2010, Monthly Notices of the Royal Astronomical Society, 403, 870

Behrens, C., & Braun, H. 2014, Astronomy and Astrophysics, 572, A74

Bell, E. F., McIntosh, D. H., Katz, N., & Weinberg, M. D. 2003, 289

Blanc, G. a., Adams, J. J., Gebhardt, K., et al. 2011, The Astrophysical Journal, 736, 31

Bouwens, R. J., Aravena, M., Decarli, R., et al. 2016, The Astrophysical Journal, 833, 72

Bridge, J. S., Hayes, M., Melinder, J., et al. 2017, The Astrophysical Journal, 852, 9

Brocklehurst, M. 1971, MNRAS, 153, 471

Bruzual, G., & Charlot, S. 2003, Monthly Notices of the Royal Astronomical Society, 344, 1000

Buat, V., Noll, S., Burgarella, D., et al. 2012, Astronomy & Astrophysics, 545, A141

Calzetti, D., Armus, L., Bohkin, R., et al. 2000, ApJ, 533, 682

Cantalupo, S., Porciani, C., Lilly, S. J., & Miniati, F. 2005, The Astrophysical Journal, 628, 61

Capak, P., Cowie, L. L., Hu, E. M., et al. 2004, The Astronomical Journal, 127, 180

Capak, P., Aussel, H., Ajiki, M., et al. 2007, The Astrophysical Journal Supplement Series, 172, 99

Chabrier, G., & Chabrier, G. 2003, PASP, 115, 763

Charlot, S., & Fall, S. M. 1993, Astrophysical Journal v.415, 415, 580

Cochrane, R. K., Best, P. N., Sobral, D., et al. 2018, Monthly Notices of the Royal Astronomical Society, 475, 3730

Dekel, A., & Birnboim, Y. 2006, Monthly Notices of the Royal Astronomical Society, 368, 2

Diemer, B., & Kravtsov, A. V. 2015, The Astrophysical Journal, 799, 108

Dijkstra, M., & Kramer, R. 2012, Monthly Notices of the Royal Astronomical Society, 424, 1672

Dijkstra, M., & Loeb, A. 2009, Monthly Notices of the Royal Astronomical Society, 400, 1109

Duval, F., Schaerer, D., Östlin, G., & Laursen, P. 2014, Astronomy & Astrophysics, 562, A52

Eisenstein, D. J., & Hu, W. 1998, The Astrophysical Journal, 496, 605

—. 1999, the Astrophysical Journal, 511, 5

Elbaz, D., Daddi, E., Borgne, D. L., et al. 2007, A&A, 468, 33

Erb, D. K., Steidel, C. C., Shapley, A. E., et al. 2006, The Astrophysical Journal, 647, 128

Fardal, M. A., Katz, N., Gardner, J. P., et al. 2001, Astrophysical Journal, 562, 605

Faucher-Giguère, C. A., Kereš, D., Dijkstra, M., Hernquist, L., & Zaldarriaga, M. 2010, Astrophysical Journal, 725, 633

Feldmeier, J. J., Hagen, A., Ciardullo, R., et al. 2013, Astrophysical Journal, 776, 75

Finkelstein, S. L., Rhoads, J. E., Malhotra, S., & Grogin, N. 2009, The Astrophysical Journal, 691, 465

Finkelstein, S. L., Rhoads, J. E., Malhotra, S., Grogin, N., & Wang, J. 2008, ApJ, 678, 655

Fudamoto, Y., Oesch, P. A., Schinnerer, E., et al. 2017, MNRAS, 472, 483

Furlanetto, S. R., Schaye, J., Springel, V., & Hernquist, L. 2005, The Astrophysical Journal, 622, 7

Furusawa, H., Kosugi, G., Akiyama, M., et al. 2008, ApJs, 176, 1

Garel, T., Blaizot, J., Guiderdoni, B., et al. 2015, Monthly Notices of the Royal Astronomical Society, 450, 1279

Giacconi, R., Rosati, P., & Tozzi, P. 2001, The Astrophysical Journal, 551, 624

Goerdt, T., Dekel, A., Sternberg, A., et al. 2010, Monthly Notices of the Royal Astronomical Society, 407, 613

Gordon, K. D., Clayton, G. C., Misselt, K. A., Landolt, A. U., & Wolff, M. J. 2003, ApJ, 594, 279

Goto, T., Utsumi, Y., Furusawa, H., Miyazaki, S., & Komiyama,

Y. 2009, Monthly Notices of the Royal Astronomical Society, 400, 843
Guaita, L., Gawiser, E., Padilla, N., et al. 2010, The Astrophysical Journal, 714, 255
Guaita, L., Talia, M., Pentericci, L., et al. 2017, Astronomy & Astrophysics, 606, A19
Hagen, A., Zeimann, G. R., Behrens, C., et al. 2016, The Astrophysical Journal, 817, 79
Haiman, Z., Spaans, M., & Quataert, E. 2000, Astrophysical Journal, 537, L5
Hansen, M., & Peng Oh, S. 2006, Monthly Notices of the Royal Astronomical Society, 367, 979
Harikane, Y., Ouchi, M., Shibuya, T., et al. 2017
Hashimoto, T., Ouchi, M., Shimasaku, K., et al. 2013, The Astrophysical Journal, 765, 70
Hashimoto, T., Verhamme, A., Ouchi, M., et al. 2015, The Astrophysical Journal, 812, 157
Hashimoto, T., Ouchi, M., Shimasaku, K., et al. 2017, MNRAS, 465, 1543
Hayashino, T., Matsuda, Y., Tamura, H., et al. 2004, The Astrophysical Journal Letters, 128, 2073
Hayes, M., Östlin, G., Mas-Hesse, J., et al. 2005, Astronomy and Astrophysics, 438, 71
Hayes, M., Schaerer, D., Östlin, G., et al. 2011, The Astrophysical Journal, 730, 8
Hayes, M., Östlin, G., Schaerer, D., et al. 2010, Nature, 464, 562
—. 2013, The Astrophysical Journal, 765, L27
Hayes, M., Östlin, G., Duval, F., et al. 2014, ApJ, 782, 6
Heinis, S., Buat, V., Béthermin, M., et al. 2014, Monthly Notices of the Royal Astronomical Society, 437, 1268
Keel, W. C., Cohen, S. H., Windhorst, R. A., & Waddington, I. 1999, The Astrophysical Journal Letters, 118, 2547
Kennicutt, R. C. 1998, STAR FORMATION IN GALAXIES ALONG THE HUBBLE SEQUENCE
Kereš, D., Katz, N., Weinberg, D. H., & Davé, R. 2005, Monthly Notices of the Royal Astronomical Society, 363, 2
Khostovan, A. A., Sobral, D., Mobasher, B., et al. 2017, arXiv, 1705.01101
Kobayashi, M. A. R., Murata, K. L., Koekemoer, A. M., et al. 2016, The Astrophysical Journal, 819, 0
Kojima, T., Ouchi, M., Nakajima, K., et al. 2017, PASJ, 69, 44
Kollmeier, J. A., Zheng, Z., Davé, R., et al. 2010, Astrophysical Journal, 708, 1048
Konno, A., Ouchi, M., Nakajima, K., et al. 2016, The Astrophysical Journal, 823, 20
Koprowski, M. P., Coppin, K. E. K., Geach, J. E., et al. 2018, arXiv:1801.00791, 1
Kornei, K. a., Shapley, A. E., Erb, D. K., et al. 2010, The Astrophysical Journal, 711, 693
Kroupa, P. 2001, Monthly Notices of the Royal Astronomical Society, 322, 231
Kunth, D., Leitherer, C., Mas-Hesse, J. M., Östlin, G., & Petrosian, A. 2003, The Astrophysical Journal, 597, 263
Kunth, D., Mas-Hesse, J. M., Terlevich, E., et al. 1998, Astronomy and Astrophysics, 334, 11
Kusakabe, H., Shimasaku, K., Nakajima, K., & Ouchi, M. 2015, The Astrophysical Journal, 800, L29
Kusakabe, H., Shimasaku, K., Ouchi, M., et al. 2018, Publications of the Astronomical Society of Japan, 70, 1
Lai, K., Huang, J.-s., Fazio, G., et al. 2008, ApJ, 674, 70
Laigle, C., McCracken, H. J., Ilbert, O., et al. 2016, The Astrophysical Journal Supplement Series, 224, 1
Lake, E., Zheng, Z., Cen, R., et al. 2015, The Astrophysical Journal, 806, 46
Landy, S. D., & Szalay, A. S. 1993, The Astrophysical Journal, 412, 64
Laursen, P., Duval, F., & Östlin, G. 2013, Astrophysical Journal, 766, 124
Laursen, P., & Sommer-Larsen, J. 2007, The Astrophysical Journal, 657, L69
Lawrence, A., Warren, S. J., Almaini, O., et al. 2007, Monthly Notices of the Royal Astronomical Society, 379, 1599
Leclercq, F., Bacon, R., Wisotzki, L., et al. 2017, Astronomy & Astrophysics, 608, A8
Madau, P. 1995, The Astrophysical Journal, 441, 18
Malhotra, S., & Rhoads, J. E. 2002, ApJ, 565, L71
Malkan, M. A., Cohen, D. P., Maruyama, M., et al. 2017, The Astrophysical Journal, 850, 5
Mas-Ribas, L., & Dijkstra, M. 2016, The Astrophysical Journal, 822, 84
Mas-Ribas, L., Dijkstra, M., Hennawi, J. F., et al. 2017, The Astrophysical Journal, 841, 19
Matsuda, Y., Yamada, T., Hayashino, T., et al. 2011, Monthly Notices of the Royal Astronomical Society: Letters, 410, 13
—. 2012, Monthly Notices of the Royal Astronomical Society, 425, 878
Matthee, J., Sobral, D., Oteo, I., et al. 2016, Monthly Notices of the Royal Astronomical Society, 458, 449
McCracken, H. J., Milvang-Jensen, B., Dunlop, J., et al. 2012, Astronomy & Astrophysics, 544, A156
McLure, R. J., Dunlop, J. S., Cullen, F., et al. 2017, ArXiv:1709.06102, 17, 1
Mehta, V., Scarlata, C., Capak, P., et al. 2017, arxiv:1711.05280
Meurer, G. R., Heckman, T., & Calzetti, D. 1999, ApJ, 521, 64
Momose, R., Ouchi, M., Nakajima, K., et al. 2014, MNRAS442, 442, 110
—. 2016, Monthly Notices of the Royal Astronomical Society, 457, 2318
Mori, M., & Umemura, M. 2006, Nature, 440, 644
Moster, B. P., Naab, T., & White, S. D. M. 2013, Monthly Notices of the Royal Astronomical Society, 428, 3121
Nakajima, K., Ellis, R. S., Iwata, I., et al. 2016, The Astrophysical Journal, 831, L9

Nakajima, K., Fletcher, T., Ellis, R. S., Robertson, B. E., & Iwata, I. 2018, ArXiv:1801.03085, 13, 1

Nakajima, K., & Ouchi, M. 2014, Monthly Notices of the Royal Astronomical Society, 442, 900

Nakajima, K., Ouchi, M., Shimasaku, K., et al. 2013, The Astrophysical Journal, 769, 3

—. 2012, The Astrophysical Journal, 745, 12

Nestor, D. B., Shapley, A. E., Kornei, K. a., Steidel, C. C., & Siana, B. 2013, The Astrophysical Journal, 765, 47

Neufeld, d. A. 1991, ApJ, 370, 85

Nickerson, S., Stinson, G., Couchman, H. M. P., Bailin, J., & Wadsley, J. 2013, Monthly Notices of the Royal Astronomical Society, 429, 452

Noeske, K. G., Kassin, S. a., Weiner, B. J., et al. 2007, ApJ, 10, 35

Okamoto, T., Frenk, C. S., Jenkins, A., & Theuns, T. 2010, Monthly Notices of the Royal Astronomical Society, 406, 208

Oke, J. B., & Gunn, J. E. 1983, The Astrophysical Journal, 266, 713

Ono, Y., Shimasaku, K., Dunlop, J., et al. 2010, The Astrophysical Journal, 724, 1524

Östlin, G., Hayes, M., Kunth, D., et al. 2009, The Astronomical Journal, 138, 923

Östlin, G., Hayes, M., Duval, F., et al. 2014, The Astrophysical Journal, 797, 11

Oteo, I., Sobral, D., Ivison, R. J., et al. 2015, Monthly Notices of the Royal Astronomical Society, 452, 2018

Ouchi, M., Shimasaku, K., Furusawa, H., et al. 2003, The Astrophysical Journal, 582, 60

Ouchi, M., Harikane, Y., Shibuya, T., et al. 2018, Publications of the Astronomical Society of Japan, 70, 1

Overzier, R. a., Heckman, T. M., Wang, J., et al. 2011, The Astrophysical Journal, 726, L7

Paulino-Afonso, A., Sobral, D., Ribeiro, B., et al. 2018, Monthly Notices of the Royal Astronomical Society, doi:10.1093/mnras/sty281

Pirzkal, N., Malhotra, S., Rhoads, J. E., & Xu, C. 2007, The Astrophysical Journal, 667, 49

Plank Collaboration. 2016, A&A, 594, 13

Reddy, N. a., Erb, D. K., Pettini, M., Steidel, C. C., & Shapley, A. E. 2010, The Astrophysical Journal, 712, 1070

Reddy, N. A., Oesch, P. A., Bouwens, R. J., et al. 2018, The Astrophysical Journal, 853, 56

Rodighiero, G., Daddi, E., Baronchelli, I., et al. 2011, The Astrophysical Journal, 739, L40

Rosdahl, J., & Blaizot, J. 2012, Monthly Notices of the Royal Astronomical Society, 423, 344

Sales, L. V., Vogelsberger, M., Genel, S., et al. 2014, Monthly Notices of the Royal Astronomical Society: Letters, 447, L6

Salpeter, E. E. 1955, Astrophysical Journal, 121, 161

Santini, P., Fontana, A., Castellano, M., et al. 2017, The Astrophysical Journal, 847, 76

Scarlata, C., Colbert, J., Teplitz, H. I., et al. 2009, The Astrophysical Journal, 704, L98

Schlegel, D. J. D. J., Finkbeiner, D. P. D. P., & Davis, M. 1998, The Astrophysical Journal, 500, 525

Scoville, N., Abraham, R. G., Aussel, H., et al. 2007, ApJs, 172, 38

Shibuya, T., Ouchi, M., Nakajima, K., et al. 2014a, The Astrophysical Journal, 785, 64

—. 2014b, The Astrophysical Journal, 788, 74

Shibuya, T., Ouchi, M., Konno, A., et al. 2018, Publications of the Astronomical Society of Japan, 70, 1

Shimakawa, R., Kodama, T., Shibuya, T., et al. 2017, MNRAS, 468, 1123

Shimizu, I., Yoshida, N., & Okamoto, T. 2011, Monthly Notices of the Royal Astronomical Society, 418, 2273

Shivaei, I., Reddy, N., Shapley, A., et al. 2017, The Astrophysical Journal, 837, 157

Simon, P. 2007, Astronomy & Astrophysics, 473, 711

Skelton, R. E., Whitaker, K. E., Momcheva, I. G., et al. 2014, The Astrophysical Journal Supplement Series, 214, 24

Sobral, D., Best, P. N., Smail, I., et al. 2014, Monthly Notices of the Royal Astronomical Society, 437, 3516

Song, M., Finkelstein, S. L., Gebhardt, K., et al. 2014, The Astrophysical Journal, 791, 3

Speagle, J. S., Steinhardt, C. L., Capak, P. L., & Silverman, J. D. 2014, The Astrophysical Journal Supplement Series, 214, 15

Steidel, C. C., Bogosavljević, M., Shapley, A. E., et al. 2011, The Astrophysical Journal, 736, 160

Tadaki, K.-i., Kodama, T., Tanaka, I., et al. 2013, The Astrophysical Journal, 778, 114

Tadaki, K. I., Kohno, K., Kodama, T., et al. 2015, Astrophysical Journal Letters, 811, L3

Tadaki, K.-i., Genzel, R., Kodama, T., et al. 2017, The Astrophysical Journal, 834, 135

Tal, T., van Dokkum, P. G., Franx, M., et al. 2013, The Astrophysical Journal, 769, 31

Taniguchi, Y., & Shioya, Y. 2000, Astrophysical Journal Letters v.489, 532, L13

Taniguchi, Y., Scoville, N., Murayama, T., et al. 2007, The Astrophysical Journal Supplement Series, 172, 9

Taniguchi, Y., Kajisawa, M., Kobayashi, M. A. R., et al. 2015, The Astrophysical Journal, 809, L7

The Astropy Collaboration, Robitaille, T. P., Tollerud, E. J., et al. 2013, Astronomy & Astrophysics, 558, A33

Tinker, J. L., Robertson, B. E., Kravtsov, A. V., et al. 2010, The Astrophysical Journal, 724, 878

Tomczak, A. R., Quadri, R. F., Tran, K.-V. H., et al. 2016, The Astrophysical Journal, 817, 118

Totsuji, H., & Kihara, T. 1969, Publications of the Astronomical Society of Japan, 21, 221

Trentham, N., & Tully, R. B. 2009, Monthly Notices of the Royal Astronomical Society, 398, 722
Vargas, C. J., Bish, H., Acquaviva, V., et al. 2014, The Astrophysical Journal, 783, 26
Verhamme, A., Dubois, Y., Blaizot, J., et al. 2012, A&A, 546, 111
Verhamme, A., Schaerer, D., & Maselli, A. 2006, A&A, 460, 397
Wang, W., Sales, L. V., Henriques, B. M. B., & White, S. D. M. 2014, Monthly Notices of the Royal Astronomical Society, 442, 1363
Whitaker, K. E., Franx, M., Leja, J., et al. 2014, ApJ, 795, 104
Wisotzki, L., Bacon, R., Blaizot, J., et al. 2016, A&A, 587, 98
Xue, R., Lee, K.-S., Dey, A., et al. 2017, The Astrophysical Journal, 837, 172
Yagi, M., Suzuki, N., Yamanoi, H., et al. 2013, PASJ, 65, 22
Yajima, H., Li, Y., & Zhu, Q. 2013, The Astrophysical Journal, 773, 151
Yajima, H., Li, Y., Zhu, Q., et al. 2012, Astrophysical Journal, 754, 118
Zehavi, I., Weinberg, D. H., Zheng, Z., et al. 2004, The Astrophysical Journal, 608, 16
Zheng, Z., Cen, R., Weinberg, D., Trac, H., & Miralda-Escudé, J. 2011, The Astrophysical Journal, 739, 62